WL-TR-97-3111

THREE-DIMENSIONAL HYPERSONIC BOUNDARY LAYER STABILITY AND TRANSITION

Roger L. Kimmel
J. Poggie

Aerodynamic Configuration Branch (AFRL/VAAA)
Aeronautical Sciences Division
Air Vehicles Directorate
Air Force Research Laboratory, Air Force Materiel Command
Wright-Patterson Air Force Base, OH 45433-7542

DECEMBER 1997

Final Report for 01 August 1994 – 01 December 1997

20031001 105

AIR VEHICLES DIRECTORATE
AIR FORCE RESEARCH LABORATORY
AIR FORCE MATERIEL COMMAND
WRIGHT-PATTERSON AIR FORCE BASE, OH 45433-7542

NOTICE

USING GOVERNMENT DRAWINGS, SPECIFICATIONS, OR OTHER DATA INCLUDED IN THIS DOCUMENT FOR ANY PURPOSE OTHER THAN GOVERNMENT PROCUREMENT DOES NOT IN ANY WAY OBLIGATE THE US GOVERNMENT. THE FACT THAT THE GOVERNMENT FORMULATED OR SUPPLIED THE DRAWINGS, SPECIFICATIONS, OR OTHER DATA DOES NOT LICENSE THE HOLDER OR ANY OTHER PERSON OR CORPORATION; OR CONVEY ANY RIGHTS OR PERMISSION TO MANUFACTURE, USE, OR SELL ANY PATENTED INVENTION THAT MAY RELATE TO THEM.

THIS REPORT IS RELEASABLE TO THE NATIONAL TECHNICAL INFORMATION SERVICE (NTIS). AT NTIS, IT WILL BE AVAILABLE TO THE GENERAL PUBLIC, INCLUDING FOREIGN NATIONS.

THIS TECHNICAL REPORT HAS BEEN REVIEWED AND IS APPROVED FOR PUBLICATION.

/s/ _____   /s/ _____
Roger L. Kimmel   Dieter Multhopp
Senior Research Engineer   Chief, Aerodynamic Configuration Research
                                         Branch

/s/ _____

TIM J. SCHUMACHER, Chief
Aeronautical Sciences Division
Air Vehicles Directorate

Do not return copies of this report unless contractual obligations or notice on a specific document requires its return.

REPORT DOCUMENTATION PAGE

The public reporting burden for this collection of information is estimated to average 1 hour per response, including the time for reviewing instructions, searching existing data sources, gathering and maintaining the data needed, and completing and reviewing the collection of information. Send comments regarding this burden estimate or any other aspect of this collection of information, including suggestions for reducing this burden, to Department of Defense, Washington Headquarters Services, Directorate for Information Operations and Reports (0704-0188), 1215 Jefferson Davis Highway, Suite 1204, Arlington, VA 22202-4302. Respondents should be aware that notwithstanding any other provision of law, no person shall be subject to any penalty for failing to comply with a collection of information if it does not display a currently valid OMB control number. **PLEASE DO NOT RETURN YOUR FORM TO THE ABOVE ADDRESS.**

1. REPORT DATE (DD-MM-YY)	2. REPORT TYPE	3. DATES COVERED (From - To)
December 1997	Final	08/01/1994 – 12/01/1997

4. TITLE AND SUBTITLE

THREE-DIMENSIONAL HYPERSONIC BOUNDARY LAYER STABILITY AND TRANSITION

5a. CONTRACT NUMBER
In-House

5b. GRANT NUMBER

5c. PROGRAM ELEMENT NUMBER
61102F

6. AUTHOR(S)

Roger L. Kimmel
J. Poggie

5d. PROJECT NUMBER
2307

5e. TASK NUMBER
N4

5f. WORK UNIT NUMBER
66

7. PERFORMING ORGANIZATION NAME(S) AND ADDRESS(ES)

Aerodynamic Configuration Branch (AFRL/VAAA)
Aeronautical Sciences Division
Air Vehicles Directorate
Air Force Research Laboratory, Air Force Materiel Command
Wright-Patterson Air Force Base, OH 45433-7542

8. PERFORMING ORGANIZATION REPORT NUMBER

WL-TR-97-3111

9. SPONSORING/MONITORING AGENCY NAME(S) AND ADDRESS(ES)

Air Vehicles Directorate
Air Force Research Laboratory
Air Force Materiel Command
Wright-Patterson AFB, OH 45433-7542

10. SPONSORING/MONITORING AGENCY ACRONYM(S)

AFRL/VAAA

11. SPONSORING/MONITORING AGENCY REPORT NUMBER(S)
WL-TR-97-3111

12. DISTRIBUTION/AVAILABILITY STATEMENT
Approved for public release; distribution is unlimited.

13. SUPPLEMENTARY NOTES

14. ABSTRACT

The stability and transition of three-dimensional boundary layers was studied. In the first phase of the investigation, arrays of hot film probes were used to measure the three-dimensional structure of instability waves on an axisymmetric cone at Mach 8. In the second phase, linear stability theory was used to design a cone with an elliptic cross section, which was also tested at Mach 8. Results show that disturbances on the axisymmetric cone travel in wave packets with predominantly zero wave angle. On the elliptic cone, only weak evidence for stationary waves was found. The predominant waves were traveling waves at about 12 kHz. Additional waves, probably second mode, occurred near 80 kHz.

15. SUBJECT TERMS

HYPERSONICS, TRANSITION, TURBULENCE, BOUNDARY LAYERS, HEAT TRANSFER

16. SECURITY CLASSIFICATION OF:			17. LIMITATION OF ABSTRACT:	18. NUMBER OF PAGES	19a. NAME OF RESPONSIBLE PERSON (Monitor)
a. REPORT	b. ABSTRACT	c. THIS PAGE	SAR	86	Roger L. Kimmel
Unclassified	Unclassified	Unclassified			19b. TELEPHONE NUMBER (Include Area Code) (937) 255-8295

CONTENTS

FIGURES

PREFACE

NOMENCLATURE

A = disturbance amplitude

b^2 = bicoherence, Eqn. (4-1)

C = co-spectrum, Eqn. (2-3), integral path, Eqn. (5-5)

c^2 = cross bicoherence, Eqn. (4-2)

c_r = convection velocity in streamwise direction

d = roughness diameter

E = expected value

e = ratio of major to minor axes of ellipse

f = frequency

H = compressibility factor, $\eta(\delta_{10}) / \int_0^{\eta(\delta_{10})} (T / T_e)d\eta$, Ref. 37

h = enthalpy, J/kg, or ratio of computed laminar to measured heat transfer

i,j,k = computational indices for elliptic cone

j = $\sqrt{-1}$

$\vec{k}$ = wavenumber

G = cross spectrum Eqn. (2-2)

L = model length, 1.016 m, or wall cooling factor in modified crossflow Reynolds number, Ref. 37

M = Mach number

N = number of time records averaged, or log of amplitude ratio (A/A_0)

$\vec{n}$ = unit normal to surface

p = pressure

Q = quad-spectrum, Eqn. (2-3)

$\dot{q}$ = heat flux, W/m^2

R = film resistance, Ohms. Also, Reed and Haynes (Ref. 37) crossflow parameter,
$Re_{cf(new)}U_e / w_{max}$

Re = Reynolds number based on boundary layer edge conditions and running length along model surface

Re_{cf} = crossflow Reynolds number, $w_{max}\delta_{10} / \nu_e$, Ref. 37

$Re_{cf(new)}$ = new crossflow Reynolds number, $HL\,Re_{cf}$, Ref. 37

Re_u = unit Reynolds number, m^{-1}

Re_L = Reynolds number based on freestream (upstream of the model bow-shock) conditions and model reference length, $Re_{u\infty}L$

Re_x = Reynolds number based on freestream conditions and longitudinal distance along model axis,
$Re_{u\infty}x$

S = auto-power spectrum

St = Stanton number, $\dot{q} / (\rho_\infty U_\infty (h(T_0) - h(T_w)))$

T = temperature or record length

t = time

U = axial velocity

w_{max} = maximum crossflow velocity, m/s

X = complex Fourier coefficient

x = longitudinal distance from model apex to measuring station, measured along model centerline

x' = unwrapped surface coordinate on elliptic cone

y = on axisymmetric cone, distance away from model surface, measured perpendicular to model surface. On elliptic cone, coordinate oriented along major axis of ellipse (Fig. 2-1)

y' = on axisymmetric cone, y-distance from model surface to point equidistant between two vertically separated probes. On elliptic cone, unwrapped surface coordinate.

z = on axisymmetric cone, distance along circular arc centered on model centerline. On elliptic cone, coordinate oriented along minor axis of ellipse (Fig. 2-1)

α = temperature coefficient of resistance, $^{\circ}C^{-1}$, or elevation angle in spherical coordinate system, deg.

α_i = amplification rate, N / meter

β = quadratic temperature coefficient of resistance, $^{\circ}C^{-2}$, or azimuthal angle in spherical coordinate system, deg.

δ_{10} = height above w_{max} point where crossflow is 10% of w_{max}, m

γ^2 = coherence function

δ = boundary layer thickness

η = computational radial coordinate perpendicular to model

ν = kinematic viscosity, m^2/s

$\vec{v}$ = wave velocity

ρ = density, kg/m^3

θ = structure angle (Fig. 3-8), elliptic cone angular coordinate (Fig. 2-1), or phase angle between two hot film probes

θ_c = cone half angle

ξ_x = probe separation in the x-direction (Fig. 3-5)

ξ_y = probe separation in the y-direction (Fig. 3-5)

ξ_z = probe separation in the z-direction (Fig. 3-5)

σ = root mean square

τ = time delay, seconds

ϕ = eigenfunction phase, or phase function of wave

ω = angular frequency of wave

Ψ = wave train function, Eqn (5-1)

ψ = wave angle (normal to constant phase line) relative to edge velocity, deg.

Subscripts

e = boundary layer edge

g = group

max = evaluated at optimum time delay

L = based on model length, 1.016 m

N = Nyquist

p = phase

w = wall

o = stagnation condition, or for disturbance amplitude, at lower neutral branch

∞ = freestream conditions, upstream of model bow shock

Superscripts

$*$ = complex conjugate

1. INTRODUCTION

Boundary Layer Stability and Transition

Boundary layer transition impacts hypersonic vehicle design through the significant increases in heat transfer and skin friction that occur when the boundary layer transitions from laminar to turbulent flow. Transition also impacts engine performance, aerodynamics, and drag. Currently, hypersonic boundary layer transition cannot be accurately predicted due to its complexity. Uncertainty in transition location leads to diminished vehicle performance, primarily because of the additional weight of thermal protection needed to accommodate heating uncertainty. These factors provide motivation for accurate transition prediction. Improved understanding of the physics of hypersonic transition is certainly required to discern new phenomena and to challenge and validate computation and prediction.

It has been recognized for many years that stability theory forms a foundation for the prediction of transition and the interpretation of experimental results.[1,2] Stability theory predicts the growth and decay of periodic disturbances as a function of Reynolds number, over a range of frequencies and wavenumbers. Both streamwise and azimuthal, (circumferential) wavenumbers are considered. Disturbances with non-zero azimuthal wavenumbers are oblique waves, those with zero azimuthal wavenumbers are two-dimensional. Limited experimental results[3] have verified basic predictions that second mode instabilities, which are essentially acoustic waves, dominate hypersonic axisymmetric boundary layer transition. First mode, or vortical disturbances (Tollmien-Schlichting waves) are also present, but not dominant.

Early work in hypersonic boundary layer stability was largely limited to simplified configurations and idealized disturbances. The goal of the current study was to move to a higher level of geometric complexity by examining three-dimensional disturbances on three-dimensional bodies. The first phase of the process involved examination of three-dimensional disturbances on axisymmetric bodies. The second phase involved the study of three-dimensional disturbances on three-dimensional bodies. The following sections provide background on these two phases.

Three-dimensional Disturbances on Axisymmetric Bodies

It is likely that a broad spectrum of wavenumbers and frequencies would be present in a flight environment to excite the boundary layer. Even measurements in "low turbulence" or "quiet" facilities which rely on the background spectrum of the wind tunnel to excite disturbances show a continuous bands of unstable amplified frequencies and nonlinear harmonics.[4, 5, 6] In addition to atmospheric turbulence and inhomogeneities over a range of scales, a thrusting hypersonic vehicle would experience vibration due to turbulent engine exhaust and a turbulent boundary layer over the aft of the vehicle. Such a vibration would not only cause a time-dependent displacement of the body, but would also cause a time-dependent distortion of the shock and create broadband vorticity and acoustic waves.

Each transition prediction method differs in how multiple superimposed frequencies and wavenumbers are handled. Methods include Linear Stability Theory (LST), Parabolized Stability Equations (PSE), and Direct Navier Stokes Simulation (DNS).

LST, by definition, treats each frequency and wavenumber independently. It cannot account for disturbance amplitude, nonlinear wave interactions, or other nonlinear effects. Eigenvalues and eigenfunctions for a spectrum of azimuthal and streamwise wavenumbers can be calculated, but not their interaction. Despite these limitations, LST has been successful at correlating some hypersonic transition results[6] and describing unstable frequencies and wavenumbers in hypersonic boundary layers.[7]

PSE offers the possibility of taking disturbance amplitude and nonlinear wave interaction into account. Herbert, et al.[8] and Malik et al.[9] have identified nonlinear oblique wave interactions which give rise to longitudinal vorticity as a possible breakdown mechanism in the hypersonic boundary layer, based on PSE computations. The PSE method requires initial disturbance amplitudes and their three-dimensional wave number spectrum. Full validation of the nonlinear interaction computations also requires spatially distributed measurements to resolve 3D oblique wave interactions.

DNS computations, given sufficient computational resources, may be carried farther into the breakdown regime than PSE. Pruett et al.[10] used DNS to calculate the breakdown of a boundary layer on an adiabatic wall cone with an edge Mach of 6.8. To alleviate the computational burden, PSE was used to calculate the linear and initial nonlinear disturbance growth. The PSE results were then fed in as initial conditions to the DNS. Pruett also showed oblique wave interactions as being important. Although 2D waves are most unstable for the dominant second mode instability,[1] any given second mode wave at this Mach number initially evolves at lower Reynolds number as first mode, for which oblique waves are most unstable. Computations[9, 10] indicate that oblique waves may play a significant role in the transition process due to their initial first mode history.

In each of these computational approaches, broadband inputs with continuous spectra are modeled with a finite number of wavenumbers. Numerical simulations of low-speed experiments where broadband input has been simulated by impulsive point disturbances have shown that the resulting wave packets may be represented in the small amplitude regime by a sum of linear modes.[11,12] This approach requires judicious selection of the initial computational disturbance spectrum.

Very little experimental work on hypersonic boundary layer stability exists.[3,13,14] These experiments have been single-point, hot wire measurements which have focused on obtaining spatial amplification rates. Nonlinear wave interactions have been observed experimentally in single point measurements,[15] but the full 2D and 3D wavenumber content cannot be extracted from these data. In order to more fully understand the stability and transition process, multiple point measurements which reveal parameters describing the spatial structure of instability waves, such as wavelength, convection velocity, and wave angle, are required.

Spatial correlation measurements in boundary layers of any type are rare. Some notable results include those of Owen and Horstman[16] at Mach 7.2, Demetriades[17] at Mach 9.4, and Spina[18] at Mach 3, all in turbulent boundary layers. Owen and Horstman[19] also measured space-time correlations using hot wires in the transitional hypersonic boundary layer on an axisymmetric ogive-cylinder at a freestream Mach number of 7.4. Their spectral data do not show evidence of second mode instabilities preceding transition or occurring in the transition process. It is possible that the second mode was present in their experiment, but that their instrumentation did not have high-enough frequency response to resolve it.

To address these issues, the Phase I experiment measured space-time correlations in the M_e=6.8 boundary layer of 7 deg., axisymmetric sharp cone. The goal was to document the transition process from the regime of laminar flow, where linear instability waves are present, through the transition process, to turbulent flow.

Disturbances in 3D Boundary Layers

Most realistic configurations include regions of three-dimensional flow. The stability and transition characteristics of three-dimensional boundary layers differ significantly from those of two-dimensional boundary layers. The most fundamental difference is that in addition to the instability waves present in two-dimensional or axisymmetric flow, three-dimensional flows may contain

crossflow instabilities. Crossflow instabilities are stationary (zero-frequency) or traveling co-rotating vortices[20] which are established when the boundary layer edge flow direction differs sufficiently from the flow direction lower in the boundary layer. This crossflow is established by a spanwise or circumferential pressure gradient which induces a flow component perpendicular to the longitudinal axis of a body. Since the boundary layer fluid possesses lower momentum near the wall than at the edge, the interior fluid is skewed more sharply than the exterior fluid. This shearing induces vorticity with a streamwise component. Vortices which increase in strength in the streamwise direction may arise. Under some conditions, these crossflow vortices may be the dominant disturbance leading to transition. These vortices may also convect to produce non-zero-frequency disturbances.[21,22,23] Computations[24] indicate that first and second mode disturbances may still be present in three-dimensional hypersonic boundary layers, but that crossflow affects their amplification rates and the wave angles of the most unstable disturbances.

Few stability computations for fully hypersonic, three-dimensional boundary layers exist.[25] Essentially no experimental stability data exist for these flows. For this reason, it was decided that the extensive experimental data base acquired by the Air Force[3] on axisymmetric hypersonic boundary layer stability should be extended to three-dimensional configurations. An elliptic cone configuration was chosen as the candidate test geometry due to its resemblance to practical flight configurations and the geometrical advantages it offers for probe measurements. The crossflow is established by the pressure differential between the major and minor axes, which causes flow from the high pressure major axis (leading edges) to the minor axis (top and bottom centerlines).

A large portion of the literature on three-dimensional hypersonic transition deals with axisymmetric cones at angle of attack. Elliptic cone experiments of any type are relatively rare. Most elliptic cone measurements have centered on pressure distributions or forces and moments. Experimental data on heat transfer, the boundary layer, and transition are extremely limited. Heat transfer data were obtained by Burke[26] on sharp- and blunt-nosed elliptic cones at $M_\infty = 10$ and 14. The data for a sharp-nosed elliptic cone of eccentricity $e = 1.43$ at $M_\infty = 10$, replotted in Fig. 1-1, show the beginning of transition near the top centerline of the model. This behavior is qualitatively similar to the transition of cones at angle of attack, where the most forward point of transition is usually on the lee centerline.[27,28,29,30,31,32] Other features analogous to cones at angle of attack are the increased heat transfer on the leading edge, due to the higher stagnation line shear, and the lower heat transfer on the top centerline, due to the boundary layer thickening caused by the influx of fluid at this location.

Crossflow instabilities in supersonic and hypersonic flow have generally been inferred experimentally from the observation of streaks in surface visualizations. Arnal et al.,[33] for example, observed such streaks in temperature-sensitive paint on the surface of a swept cylinder at $M_\infty = 10$. The wavelengths of these streaks agreed, within experimental scatter, with predictions of crossflow wavelengths. Murakami, et al.[34], also observed such streaks on a swept cylinder at $M_\infty = 5$ using temperature-sensitive liquid crystals. The boundary layer edge Mach numbers for these cases were supersonic, however, rather than hypersonic, due to the model geometry. Oberkampf et al.[35] observed streaks on a cone at angle of attack at $M_\infty = 8$ using shear-stress-sensitive liquid crystals. Numerous investigators have observed surface streaking at supersonic and subsonic Mach numbers.

Numerous correlating parameters have been proposed to predict boundary layer transition. Correlation methods are subject to much uncertainty, especially when a correlation developed for a specific configuration is applied to a different configuration. Nevertheless, correlation methods provide a rapid means of determining the likelihood of transition. The crossflow Reynolds number is the most common parameter used to evaluate crossflow transition. Pate[36] observed that $150 < Re_{cf} < 200$ correlated transition data from a variety of sources and configurations for $0.3 < M_\infty < 7.4$. Reed and Haynes[37] observed a greater spread in crossflow transition Reynolds number for rotating cones and cones at angle of attack, and proposed a modified crossflow Reynolds number to take compressibility and wall cooling into account. Transition results from cones at angle of attack[37] at $M_\infty = 3$ and 6 were shown to be correlated by the new crossflow Reynolds number and the crossflow

velocity percentage, $100w_{max}/U_e$. These two parameters also correlated the $N = 9$ location on rotating cones calculated by linear stability theory. These results indicated a "universal" parameter, R. Reed and Haynes correlated $R = 44.0$ with transition under quiet conditions, and $R = 33.7$ with transition in conventional facilities.

Lyttle and Reed[38] performed PNS calculations for adiabatic wall elliptic cones with aspect ratios (ratio of major to minor ellipse axes) of 2, 3, and 4 at $M_\infty = 4$, and applied the crossflow Reynolds number correlation to these results. The R-parameter for these configurations peaked near the top centerline, outside of the region of validity of the above correlation. Boundary layer velocity profiles near the top centerline were inflectional and unstable in nature.

Computational analysis was required to design the elliptic cone for several reasons. First, a geometry had to be chosen which provided significant crossflow but which also possessed an extensive laminar region for probing. Second, once a configuration was chosen, computations provided a rational basis for locating instrumentation and survey stations. Third, to determine transition, calculated laminar and turbulent baseline heat transfer was required to determine where the measured heat transfer first departed from its laminar values. Finally, anomalies and uncertainties in the computation which came to light during the test article design could be scrutinized experimentally.

The current investigation of elliptic cones consisted of three phases. In the first phase, Parabolized Navier Stokes (PNS) computations were carried out for three elliptic cone configurations of aspect ratio $e = 1.5$, 2.0 and 4.0. Transition correlations were used to identify candidate configurations for detailed linear stability analysis in the second phase. The candidate configuration, the 2:1 ellipse, was selected for detailed heat transfer and hot film probe measurements.
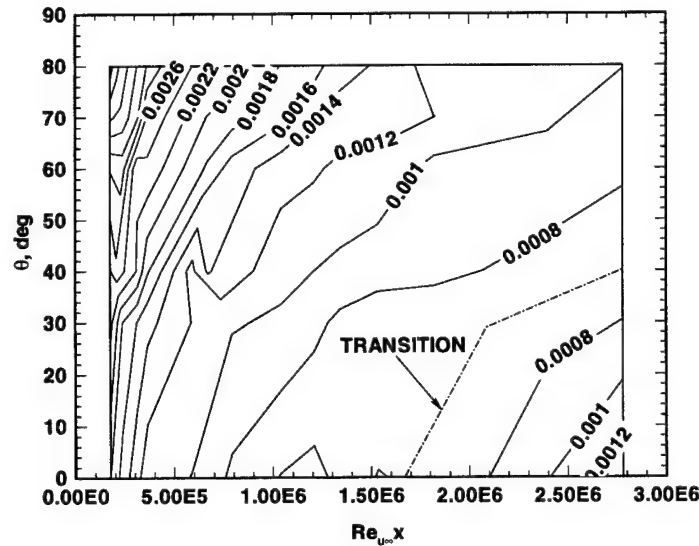

Figure 1-1. Stanton number contours for $e = 1.43$ cone at $M_\infty = 10$.

2. EXPERIMENT

Test Facility

All tests were carried out in the Arnold Engineering Development Center von Karman Facility Tunnel B (AEDC VKF-B). Tunnel B is a closed circuit hypersonic wind tunnel with a 1.27 m diameter test section. Two axisymmetric contoured nozzles provide nominal Mach numbers of 6 and 8, and the tunnel may be operated continuously over a range of stagnation pressure levels from 276 to 2070 kPa at Mach number 6 and 689 to 6200 kPa at Mach number 8. Stagnation temperatures sufficient to avoid air liquefaction in the test section (up to 750° K) are obtained through the use of a natural-gas fired combustion heater. The entire tunnel (throat, nozzle, test section, and diffuser) is cooled by integral, external water jackets. The tunnel is equipped with a model injection system, which allows removal of the model from the test section while the tunnel remains in operation. A description of the tunnel may be found in Reference 39.

Surveys of the flow field were made using a retractable overhead drive mechanism which makes it possible to change survey probes while the tunnel remains in operation. The mechanism is housed in an air lock immediately above the top of the Tunnel B test section. A remotely actuated shield was provided to protect the probes when not in use. An auxiliary on-board probe drive mechanism mounted on the model support sting was used to position a single probe in the model boundary layer at 0.895 m from the model apex. This mechanism traversed in the direction normal to the model sting. No shield was provided for the probe mounted on this auxiliary drive.

The Tunnel B freestream mean and fluctuating flow has been extensively monitored and calibrated.[40] The mean Mach number on tunnel centerline is spatially uniform in the streamwise direction to within 1.2%. Broadband root mean square (rms) freestream mass flux fluctuations on centerline are 1.2% to 1.5% of local mean values, depending on tunnel unit Reynolds number. Broadband rms total temperature fluctuations are an order of magnitude smaller than mass flux fluctuations. The freestream disturbance spectrum maximum is between 2 and 3 kHz, and the power spectrum drops off above this as approximately $1/f$. The spectrum shape is similar for all unit Reynolds numbers for both mass flux and total temperature. At $Re_{u\infty} = 1.64 \times 10^6 \text{ m}^{-1}$, the rms mass flux fluctuations in the second mode frequency band between 60 and 70 kHz are estimated to be 0.07%, based on the Reference 40 data. Modal diagrams[40] indicate a freestream disturbance source in addition to acoustic radiation from the tunnel side-wall boundary layers, perhaps total temperature non-uniformity due to uneven heating of the flow.

Axisymmetric Cone Test Article

The basic axisymmetric model for the investigation was a 7° half-angle cone of 1.016 m length and 0.250 m base diameter, with interchangeable nose sections. A sharp nose was used which had a spherical radius of 0.04 mm. In order to minimize any flow interference due to the on-board probe drive mechanism, a frustum was added to the basic cone model. This 7° frustum extended the model length to 1.283 m. and had a base diameter of 0.315 m. The frustum had a narrow slot which accommodated the movement of the strut which supported the probe mounted on the on-board drive mechanism.

The axisymmetric model was instrumented with 20 pressure orifices and four coaxial surface thermocouple gages. The 0° ray of the model was the location of 18 pressure orifices. Two orifices were located on the 180 ° ray. The four coaxial thermocouple gages were located on the 90 ° ray. In addition, four thermocouples were installed on the inside surface of the model along the 95 ° ray to monitor the equilibration of the model shell temperature.

References 3, 15, and 41 describe detailed measurements of the boundary layer stability characteristics of this model in Tunnel B at freestream Mach 8. The boundary layer is unstable to first and second mode waves, with the second mode being dominant. Reference 3 shows that the second mode waves occur as packets under these conditions. Computations detailing the eigenfunctions and most unstable wave angles for these modes are given in References 7 and 8. PSE computations[9] indicate that the second mode disturbance growth is linear to Reynolds numbers of 2.6×10^6.

Elliptic Cone Test Article

The elliptic cone model consisted of a 0.1524 m long sharp nose and three frusta, two of which were 0.2794 m long, and one which was 0.3048 m long. The nominal nose radius was 0.04 mm in the major axis. The entire model was 1.016 m long, with an elliptical cross section of aspect ratio 2.0:1. The model half angle was 7 deg in the minor axis. The nose tip was solid, and the frusta were cast and machined to final contour with a nominal wall thickness of 6.4 mm. All sections were constructed of 17-4 PH stainless steel and finished to better than 0.8 μm finish. The model geometry and coordinate system are sketched in Fig. 2-1.

One quadrant of the elliptic cone was devoted to pressure instrumentation, and one was devoted to heat transfer. One entire side between the leading edges was devoid of pressure taps and heat transfer gauges and was devoted to hot film probe measurements of the boundary layer. Heat transfer gauges and pressure taps near the leading edge of the model were displaced toward the surface instrumentation side by two degrees to keep the model leading edges clean.

Pressure taps consisted of 1 mm ID stainless steel tubing. Four pressure taps at $x / L = 0.925$ were located on the major and minor diameters. Diametrically opposed pressure taps at this location were connected to a single transducer to read a differential pressure between the two taps. Incidence angle was adjusted to zero, +/- 0.1 ° by nulling out the pressure differential between these taps.

The heat transfer gauges were 4.8 mm diameter Schmidt-Boelter gauges. The Schmidt-Boelter gauge consists of an aluminum wafer wrapped with constantan wire and and half-plated with copper to establish a thermopile of 35-40 thermocouple junctions front and back. A constant heat flux to the front surface generates a constant temperature difference across the wafer, which is measured by the thermopile. The instrumentation locations are shown in Fig. 2-2.

Mean-Flow Survey Probes

Mean flowfield measurements were obtained on the axisymmetric cone only. For mean-flow measurements of the boundary layer, a Pitot probe with a cylindrical tip and an unshielded total temperature probe were used. The Pitot probe outside diameter was 0.4 mm and the inside diameter was 0.2 mm. The tip was telescoped in a succession of larger diameter tubes for installation in the probe rake. The tube section containing the probe orifice was bent to align the probe parallel to the model surface. The total temperature probe was fabricated from a length of sheathed thermocouple wire (0.5 mm OD) with two 0.1 mm diameter wires. The wires were bared for a length of approximately 0.4 mm and a thermocouple junction of approximately 0.1 mm diameter was made.

Anemometer Instrumentation

The correlation measurements on both models were carried out using custom-built hot film probes and constant-current anemometers. The film anemometer probe designs followed the guidelines established in Reference 42. The probes consisted of a four inch long, 2.7 mm diameter twin-bore alumina tube, sharpened at the front end and bearing twin 24-gauge (0.5 mm diameter) platinum leadwires in the bores. Two hot film probe designs were used. In one of the designs, designated 70-series probes, the sharpened end terminated in a short length of 0.5 mm diameter quartz rod held parallel to the probe body. The film sensor was deposited at the tip of this quartz rod. In the other design used, designated 90-series, the platinum leadwires were stepped down to a diameter of 0.1 mm, and their ends were cemented with potter's glaze on the sharpened alumina tip. The sensor film was then applied between the tips of the two leadwires. In both designs the platinum sensor film was first painted on the quartz or glaze substrate using a liquid platinum resinate solution, and then fired at high temperatures to remove the liquid vehicle.

Typical film thicknesses were about 0.03 μm. The films were about 0.5 mm long (in the direction parallel to the test surface and normal to the flow vector) and about 0.2 mm wide (in the direction normal to the test surface). Electrical resistance of such films typically ranged from 10 to 20 ohms. For several months prior to their use in the experiment the probes and their spares were subjected to periodic resistivity calibration in a controlled oven, to monitor their condition and measure their electrical properties. The coefficients α and β of these probes in the resistance-temperature relation $R = R_0(1 + \alpha T + \beta T^2)$ were found to average 2.5×10^{-3} $^{\circ}C^{-1}$ and about -5×10^{-7} $^{\circ}C^{-2}$, respectively.

The probes have been found capable of enduring continuous exposure to temperatures of 870 $^{\circ}$F and dynamic pressures of order 140 kPa.

Flow fluctuation measurements were made using constant-current anemometry techniques. Three channels of constant-current anemometer electronics were used. One channel was based on the Philco-Ford ADP12/13 anemometer used in the earlier studies of boundary-layer stability at AEDC. Two channels were based on the VKF-91 pair of anemometers built by AEDC/VKF in 1991. In each channel the anemometer current control which supplies the heating current to the sensor is capable of maintaining the current at any one of 15 preset levels. The anemometer amplifier which amplifies the sensor response signal contains the circuits required to electronically compensate the signal for a 6-dB per octave roll-off which is characteristic of a hot-wire sensor. Unlike the frequency response of hot wire anemometers, which theoretically depends only on the wire time constant, the response of film probes depends on two parameters: the film inherent time constant in the absence of the substrate, and the so-called loss factor which combines film, flow, and substrate characteristics[42]. While the inherent time constant for the probes used in this test were estimated in the range 10-20 μsec, the loss factors were higher than 100. Under such circumstances one can easily show[43] that the thermal-lag attenuation of the probes is 3 dB/octave, and the phase lag is 45°, over most of the frequency range of interest. Therefore no differential phase lag was expected between two probes at different points in the flow in this experiment. On the other hand some quantitative distortions of the flow fluctuation spectrum were expected, since the compensating amplifiers had a 6 dB / octave gain. However, these distortions were uniform for all probes, and thus have little effect on the measurement of correlation coefficients.

The sensor heating current and mean voltage were fed to auto-ranging digital voltmeters for a visual display of these parameters and to a Bell and Howell model VR3700B magnetic tape machine for recording. The sensor response AC voltage was fed to an oscilloscope for visual display of the raw signal and to a wave analyzer for visual display of the spectra of the fluctuating signal and was recorded on magnetic tape for subsequent analysis. More details of the anemometer instrumentation are given elsewhere.[44]

Data were band-pass filtered between 10 Hz and 500 kHz and recorded using the analog FM tape recorder. Initial signal analysis for the axisymmetric cone was performed using an HP3562-A digital signal analyzer. The HP3562-A samples at 256 kHz, and the FM tape was played back at 1/8th speed for analysis, giving an effective sample rate of 2.048 MHz. Data were low-pass filtered below 1.024 MHz to prevent aliasing. The HP3562-A performed software fast Fourier transforms on the data, which provided the basis for the power and cross spectra. The data were later digitized from the FM tapes using a CAMAC data acquisition system from Kinetic Systems, Inc., and stored on a Pentium PC for analysis. The two or three channels of data were digitized simultaneously at an effective sampling rate of 1.0 MHz in records of $2^{21} = 2097152$ contiguous samples per channel. For convenience, the tape was typically replayed at half-speed and sampled at 500 kHz. The software for controlling the CAMAC crate and analyzing the data was written in-house in the C++ and FORTRAN 77 programming languages.

Most of the data analysis algorithms were adapted from the book by Bendat and Piersol[45]. The power spectral density S at frequency f is the magnitude of the Fourier spectra at that frequency, averaged over the total number of records, N, thus

$$S(f) = \frac{1}{NT} \sum_{i=1}^{N} |X_i(f)|^2 \qquad (2\text{-}1)$$

The cross spectrum G(f) of signals from two probes, designated 1 and 2, is obtained by multiplying the complex conjugate of the Fourier coefficient of signal 1 by the Fourier coefficient of signal 2, and averaging over N records, thus

$$G(f) = \frac{1}{NT} \sum_{i=1}^{N} X_{1i}^{*}(f) X_{2i}(f)$$

(2-2)

The cross spectrum, being complex, contains the phase information needed to extract time delays between the two signals as a function of frequency, and the amplitude information describing the frequency-by-frequency correlation between them, or the coherence. The cross spectrum may be written in complex form as

$$G(f) = C(f) - jQ(f) = |G(f)| e^{-j\phi(f)}$$

(2-3)

where the phase angle $\phi(f)$, is given by the inverse tangent of the ratio of the quad- to co-spectrum

$$\phi(f) = \tan^{-1}\left[Q(f) / C(f)\right] \ ]$$

(2-4)

The coherence function, γ^2, is simply the cross spectrum normalized by the product of the power spectra of the two signals at a given frequency,

$$\gamma^2(f) = \frac{|G(f)|^2}{S_1(f) S_2(f)}$$

(2-5)

The above statistical quantities were averaged over $N=120$ records of 2048 points each for streamwise and circumferential probe spacings, and $N=60$ records of 2048 points each for vertical separations.

Test Procedure: Axisymmetric Cone

The experiment was conducted at a freestream Mach number of 7.93. The stagnation temperature was 720 K, and the cone wall condition was adiabatic. Tests were carried out at freestream unit Reynolds numbers $Re_{u\infty}$ = 1.64x10^6, 3.28x10^6, 3.94x10^6, 4.92x10^6, and 6.56x10^6 per meter by varying tunnel stagnation pressure. Measurements were carried out at a nominal x-location 0.895 m aft of the model tip, producing local x-Reynolds numbers, Re, of 2.0x10^6, 4.1x10^6, 4.9x10^6, 6.1x10^6, and 8.1x10^6 based on the local boundary layer edge unit Reynolds number and x-running length along the model surface.

One hot-film probe was mounted in the on-board drive at a fixed location x=0.895 m aft of the model tip. A rake containing up to four additional hot film probes was mounted on the tunnel overhead drive (see sketch in Fig. 2-3). The axis of the overhead drive was swept back 7 deg. so that all surveys with the drive were normal to the model surface. Measurements in the circumferential (or z) direction, were carried out by positioning the probes at the maximum energy location in the boundary layer, holding the rake fixed, and rolling the model to drive the on-board probe away from the rake. The maximum energy location is defined here as the y-location in the boundary layer at which the broadband rms signal from the hot film probe is a maximum. Measurements were taken at increments of 3.18 mm circumferential separation, up to 63.5 mm between the on-board probe and the rake probe nearest it. Streamwise correlations were obtained by holding the on-board probe fixed with a circumferential separation of 6.36 mm from the nearest rake probe, and moving the rake downstream in increments of 3.18 mm, up to 25.4 mm downstream of the on-board probe. The on-board probe was held fixed at the maximum energy location, and the downstream probe was relocated at the maximum energy point at each downstream station.

The boundary layer basic state was documented with surveys of mean Pitot pressure and total temperature. During these surveys, two additional hot film probes were mounted on the rake along with the Pitot and total temperature probes. These additional hot film probes were separated in the

vertical (y) direction by 1.47 mm. Vertical correlations through the boundary layer were thus obtained during the mean flow surveys.

Test Procedure: Elliptic Cone

Heat transfer measurements were made by injecting the model into the tunnel airflow, recording the Schmidt-Boelter output, and retracting the model. The model was cooled between runs to room temperature, approximately 300 K. The tunnel nominal freestream Mach number was 7.93, and the stagnation temperature was 720K, producing a wall-to-stagnation temperature ratio of 0.42. The tunnel unit Reynolds number was changed by changing stagnation pressure. Length Reynolds numbers of $Re_L = 1.7 \times 10^6$, 2.0×10^6, 2.7×10^6, 3.3×10^6, 4.0×10^6, 5.0×10^6, 6.0×10^6, and 6.7×10^6 were tested.

Several heat transfer runs were made at $Re_L = 1.7 \times 10^6$ using roughness strips in an attempt to fix stationary crossflow vortices. Strips containing spherical roughness elements of 2 mm and 1.3 mm diameter spaced four diameters on center were placed in an arc around the model between zero and 90 degrees in the heat transfer quadrant, at $x / L = 0.225$. An additional run was made with a strip 0.165 m in length with 1.3 mm diameter roughness, placed near the leading edge of the model at $\theta = 86°$ and centered at $x / L = 0.45$. This location for leading edge roughness was selected by tracing computed surface streamlines forward from the instrumentation locations at $x / L = 0.65$ to the leading edge. Because the roughness strips covered large regions of the model, the boundary layer thickness varied along the roughness strips. For strips placed at $x / L = 0.225$, the roughness heights d / δ at $\theta = 45°$ were 0.40 and 0.62 for the 1.3 and 2.0 mm diameter roughness, respectively, based on computed boundary layer thickness. For the strip placed at $\theta = 86°$, d / δ was 0.77 at the center of the strip.

Schlieren photographs were taken at $Re_L = 1.7 \times 10^6$ with the model heated to recovery temperature and rolled to various locations. A limited number of shadowgraphs were obtained with the model at room temperature and rolled 90°. Oil-flow visualization was also obtained at $Re_L = 1.7 \times 10^6$. The oil mixture consisted of silicone pigment suspended in a silicon oil. The model was covered with machinist's blueing to enhance contrast with the oil mixture, and several runs were taken with the oil painted on in a variety of configurations. Each run lasted several minutes, during which numerous photographs were taken as the oil streamed. Model temperature for these runs was between room and recovery temperature.

Hot film probe measurements were made on the elliptic cone using the overhead drive mechanism. For the elliptic cone, the drive axis was swept 10.4°. from vertical (the average of the major and minor axis half angles), so that it traversed in a direction approximately normal to the model surface. The probe system on the overhead drive consisted of a probe foot with three hot film probes with a lateral spacing of 3.18 mm. Two probes (designated LAT and US) were positioned at the same x-location to measure lateral time delay. One probe (designated DS) was positioned 3.18 mm downstream to measure streamwise time delay.

Measurements at different circumferential locations were made by rolling the model, rolling the probe foot to orient the probe tips tangent to the model surface, and traversing the boundary layer to the maximum energy location. The majority of measurements were made at $x / L = 0.8$ at roll angles between the top centerline ($\theta = 0°$) and the leading edge ($\theta = 90°$). The data were taken under adiabatic wall conditions at a freestream unit Reynolds number of 1.97×10^6 per meter for a local Reynolds number $Re_x = 1.6 \times 10^6$.

Data Uncertainty

The quantities derived from the hot film measurements of greatest interest in this study are the coherence and phase angle. Of these two, the phase angle is more prone to error. Some possible sources of significant phase error include differential phase lag in the anemometer and recording electronics, probe-to-probe differences in phase response, and phase differences incurred from inaccuracy in probe spatial positioning. Pre-test calibration of the anemometers revealed that below 200 kHz, channel-to-channel phase differences were less than 2°. Since the thermal loss factors of the probes were relatively high, the probes could be expected to show a constant phase shift over the frequency band of interest, thus eliminating probe-to-probe differences as a significant error source. Error in the probe relative x- and y- spatial locations produces phase error due to the components of convection velocity in these directions. Assuming that disturbances convect at near the edge velocity

(which is demonstrated in the Section 3), phase error due to x-positioning error is approximately 3×10^{-4} degrees per mm of misalignment per Hz. An estimated 0.1mm uncertainty in the relative x-location of two probes thus leads to an uncertainty of 6° in phase angle at 200 kHz. The error is proportionally less at lower frequencies. The error due to vertical displacement of the probes was estimated by measuring phase angle as one probe was held fixed at the maximum energy location, while the other probe was displaced relative to the other by +/- 0.1 mm and +/- 0.25 mm in the y-direction, with a constant ξ_z separation of 9.5 mm. This y-sensitivity arises from the eigenstructure of the second mode, i.e., the inclination of constant phase lines in the $x - y$ plane. Results obtained for the second mode at a Reynolds number of 4.1×10^6 show a sensitivity of 43° per mm of y displacement. An estimated uncertainty of 0.03 mm in ξ_y thus produces an uncertainty of 1.3° in the second mode phase at the maximum energy location in the boundary layer. This should be a worst case, since the change in phase with y is maximized at the second mode frequency and at the maximum energy location.[46] The summation of these errors leads to a worst case error of 9.3°.

The cross-spectrum and the phase angle are subject to random errors due to the finite sample size used to estimate them. The cross-spectrum and phase angle errors depend on the number of samples used to estimate them and the coherence of the two signals. Bendat and Piersol[45] give formulas for the standard deviation of cross spectrum and phase for normally distributed signals. The normalized rms error in the magnitude of the cross-spectrum (the rms error in the magnitude divided by the magnitude) is equal to $1/\left(|\gamma|\sqrt{N}\right)$. The rms error in the phase angle, in radians, is given as $\left(1-\gamma^2\right)^{1/2}/\left(|\gamma|\sqrt{2N}\right)$. Although the signals obtained in this study are not normally distributed, these estimates may be used to demonstrate the trend in rms phase error with coherence. For $N = 120$ records and $\gamma^2 = 0.9$, the rms phase error is 1.2°. For the same number of records and $\gamma^2 = 0.2$, the rms phase error increases to 7.4°.

Finally, it must be remarked that no decomposition of the fluctuations into mass flux or total temperature was attempted in this measurement. According to linear stability theory the configuration of the disturbances is the same from one mode to the other. For example, the phase velocity and amplification rate should be the same for both density and total temperature fluctuations. The probe outputs were also linear combinations of these modes. For these reasons the correlations of the probe outputs should closely resemble the correlations of the flow fluctuation modes themselves. Hot wire anemometry measurements of this same flowfield[3] in which the disturbances were separated into their mass flux and total temperature components showed identical amplification rates for both components

The primary sources of inaccuracy in the transition measurements are the accuracy of the heat transfer gauges and the uncertainty in the location of maxima and minima in heat transfer due to gauge spacing. Donaldson and Hatcher[47] ascribe an accuracy of +/- 5% to the gauges. Measurements show good run-to-run precision, with variations of less than 1%. The in-situ accuracy of the Schmidt-Boelter gauges was assessed previously[48] by comparing predicted to measured laminar heat transfer on a cone. Most of the gauges fell within +/- 5% of theoretical, although a few fell outside of this band. A more conservative estimate of transducer accuracy would be +/-10 %. Gauge spacing over most of the model was $0.05L$ in the axial direction and 10 deg or less in the circumferential direction.
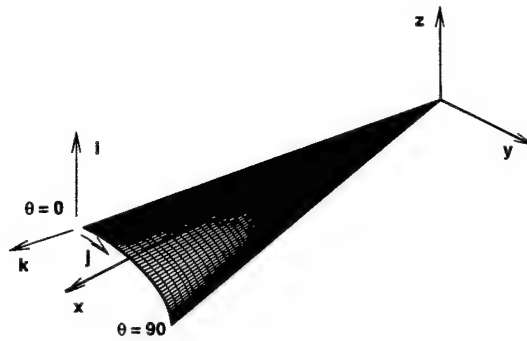
Figure 2-1. One quadrant of elliptic cone and coordinate system.
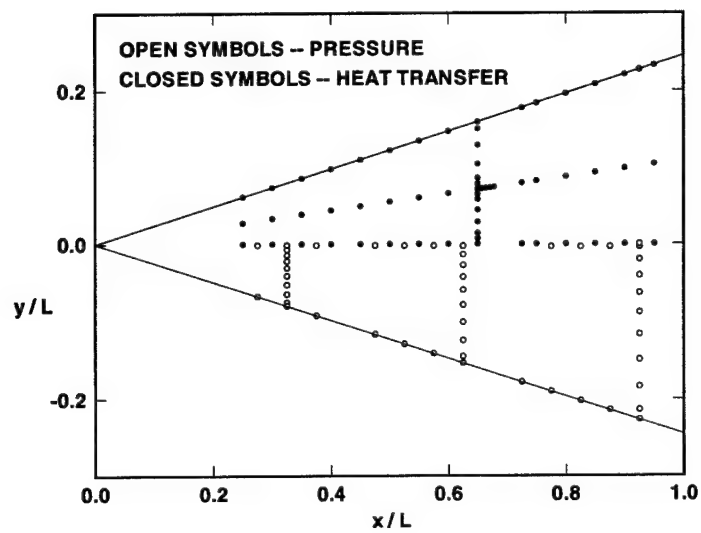

Figure 2-2. Elliptic cone static pressure taps and heat transfer gauge locations. Vertical scale exaggerated for clarity.
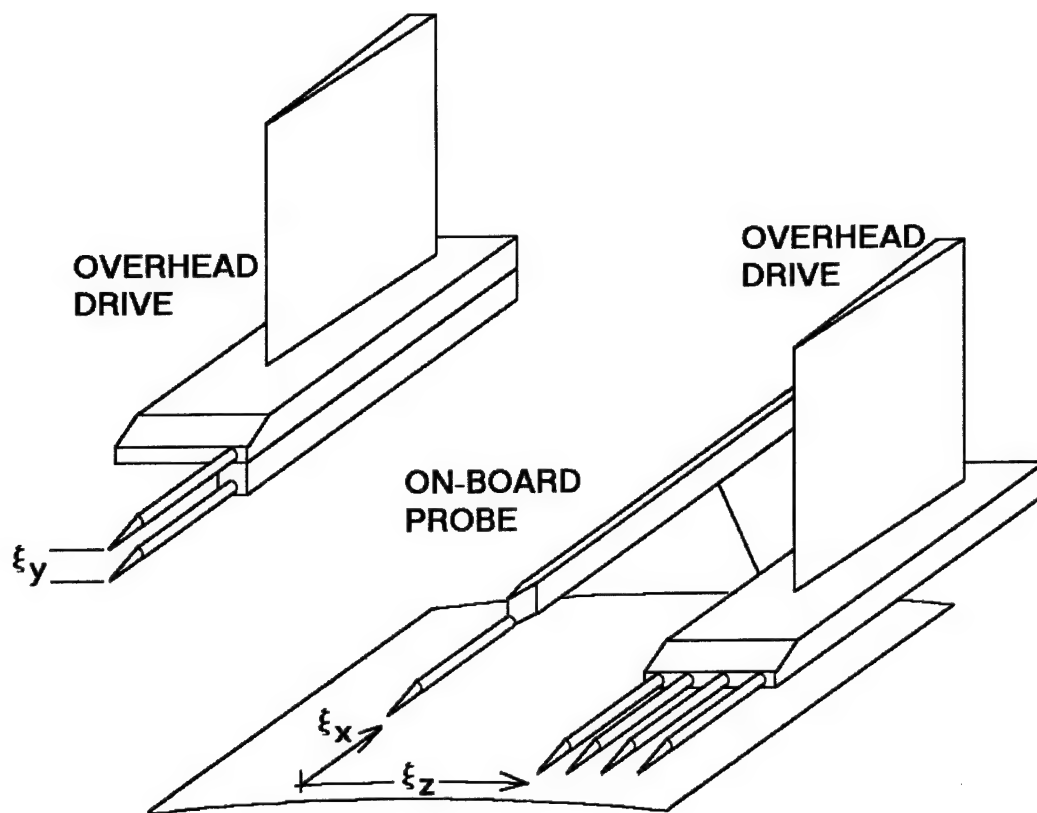
Figure 2-3. Probe drive system for correlation measurements.

3.   CIRCULAR CONE MEAN FLOW AND CROSS CORRELATIONS

Mean-Flow and Power Spectra

Mean boundary layer surveys are presented in Fig. 3-1. The boundary layer profiles are laminar at $Re = 2.0 \times 10^6$, 4.1×10^6, and possibly at 4.9×10^6. Profiles at $Re = 6.1 \times 10^6$ and 8.1×10^6 are clearly transitional. Previous hot wire studies[41] show that transition for this configuration, as defined by the x-location where the second mode amplitude reaches a maximum before decaying, begins at $x = 0.895$ m at $Re = 4.1 \times 10^6$, approximately. Heat transfer measurements reported in Ref. 48 show that the end of transition at $x = 0.895$ m, as defined by the peak in heat transfer, should occur at approximately $Re = 8.1 \times 10^6$.

Power spectra are presented in Fig. 3-2. The second mode is clearly apparent at each Reynolds number up to 8.1×10^6. The power spectra amplitudes are normalized by the broadband mean square of the signal. Previous work has shown that the peak second mode frequency scales on the boundary layer thickness and edge velocity[41] and is equal to approximately $U_e/2\delta$. This scaling occurs because the most amplified second mode wavelengths tend to be approximately twice the boundary layer thickness, and the second mode phase velocities tend to be approximately equal to the edge velocity.[7] These ratios vary little with Reynolds number and frequency. Thus, when the power spectrum frequency is scaled by U_e/δ, the second mode occurs at a nearly constant normalized frequency $f\,\delta/U_e$ of 0.5. Because of this property, the U_e/δ scaling is used here rather than the non-dimensional frequency $2\pi f/U_e\,Re_{ue}$ that is typically used in stability theory. A nonlinear harmonic[15] of the second mode occurs at a normalized frequency of approximately 1.0.

Measurements of amplification rates by Stetson, et al.,[41] on this configuration show that the second mode amplifies as Reynolds number increases until transition occurs, and that the transition is clearly second-mode dominated. The raw anemometer signal at the second mode frequency does increase with Reynolds number, but the contribution of the second mode to the overall signal rms decreases with Reynolds number, so that the normalized second mode amplitude decreases with increasing Reynolds number. The spectra of Fig. 3-2 are in general agreement with spectra measured under similar conditions on the same model in the same wind tunnel, as reported in Refs. 3 and 41, but have not been corrected for the probe frequency response. Therefore, Fig. 3-2 provides a qualitative guide to the spectral content of the signals, but cannot be considered quantitative.

Circumferential Probe Separation

The coherence as a function of frequency at minimum z-separation is presented in Fig. 3-3. The minimum circumferential separation ξ_z is a constant 3.18 mm at each Reynolds number, but the normalized separation ξ_z/δ varies due to the change in boundary layer thickness. The peak in the coherence at the second mode frequency and harmonic is evident at each Reynolds number up to 8.1×10^6. At the lower Reynolds numbers, there is a notable coherence in the 0.1 to 0.2 range of normalized frequency, which is in the first mode range.[7] Above Reynolds numbers of 2.0×10^6 there is little coherence at frequencies higher than the second mode except for the harmonic, indicating that disturbances at these frequencies have a predominant circumferential scale less than 3.18 mm.

In Fig. 3-4 the coherence function at the peak second mode frequency is plotted as a function of circumferential separation. The peak second mode frequency is defined here as the frequency at which the coherence is a maximum at $\xi_z = 3.18$ mm. Data at $Re = 8.1 \times 10^6$ are not plotted because there is no clearly definable second mode at this Reynolds number. Fig. 3-4 indicates that the circumferential scale of the second mode wave packets, which tends to be 4δ or less, based on a coherence level of 20%, decreases with Reynolds number. The second mode peak coherence at minimum spacing also decreases as Reynolds number increases, indicating that the circumferential scale of the second mode wave packets decreases as the Reynolds number increases. Experiments in subsonic boundary layers have shown that the circumferential scale of wave packets grows as Reynolds number increases.[49] Since there is no evidence of breakdown at a Reynolds number of 4.1×10^6, the decrease in circumferential scale may be due to a decrease in the scale of the freestream input disturbances. Since breakdown has begun at a Reynolds number of 4.9×10^6, as evidenced by previous studies,[41] the decrease in coherence at this Reynolds number may be due to some combination of breakdown and a decrease in input disturbance scale.

Streamwise Probe Separation

The convection velocity is the primary data of interest to be extracted from the cross-spectrum for streamwise probe separation. The probes were separated in the circumferential as well as the streamwise direction to avoid interference between the upstream and downstream probes. Since the cross-spectrum with circumferential separation showed that the waves are on average two dimensional, negligible error should be incurred due to the circumferential separation. The circumferential separation does create a problem at higher Reynolds numbers due to the drop in coherence with circumferential spacing. As noted in the discussion of statistical errors in the Experiment section, the uncertainty in cross-spectral quantities increases as the coherence decreases. Results for Reynolds numbers of 6.1×10^6 and 8.1×10^6 are not presented due to the low coherence and noisy phase results. Due to the rapid drop-off in coherence in the z-direction for the higher Reynolds numbers, meaningful convection velocities could not be extracted even using the broadband cross correlation. In order to obtain convection velocities at these Reynolds numbers, the probes would have to be spaced closer together in the z-direction.

The convection velocity was extracted using the phase angle at the maximum streamwise separation of $\xi_x = 25.4$ mm for Reynolds numbers of 2.0 and 4.1×10^6. Using the maximum separation is desirable because the relatively large phase angle at this separation provides a good signal-to-noise ratio. Because of the overall low coherence at a Reynolds number of 4.9×10^6, the convection velocity is extracted using the minimum x-separation, where coherence is highest. The streamwise convection velocity is defined as $c_r = \xi_x/\tau(f)$. The time delay as a function of frequency is obtainable from the phase, since τ will be $\phi/360$th's of a period, or $\tau = \phi(f)/360 f$, when ϕ is expressed in degrees. Convection velocities are presented in Fig. 3-5. At Reynolds numbers of 2.0×10^6 and 4.1×10^6 the normalized convection velocity c_r/U_e at the second mode frequency is between 0.95 and 1.0, in agreement with Mack's results for this configuration.[7] The data scatter increases with Reynolds number and away from the second mode frequency due to lower coherence. Data are not presented where the coherence is less than 0.05. At a Reynolds number of 2.0×10^6, the normalized

convection velocity increases as frequency decreases, up to a level of about 1.1. The measured convection velocity of $0.984\,U_e$ at the second mode frequency $f = 0.434\,U_e\,/\,\delta$ at Reynolds number 2.0×10^6 indicates a wavelength of $2.3\,\delta$, which is in agreement with Mack's computations.[7]

Vertical Probe Separation

At a Reynolds number of 2.0×10^6, coherence measurements with vertical spacing of 1.47 mm $(0.201\,\delta)$ between probes (Fig. 3-6) show a maximum coherence above 0.6 in the second mode range near the edge of the boundary layer. In principle, a second mode wave should be coherent throughout the boundary layer. Away from the boundary layer edge, however, the coherence for $\xi_y = 0.201\,\delta$ spacing is less than 0.2 due to the extremely low second-mode signal levels. The low coherence in the second mode range above the boundary layer edge indicates that any forcing input from the tunnel wall boundary layer noise is dwarfed by the second mode.

The maximum coherence (Fig. 3-6) within the boundary layer for probes separated vertically by 1.47 mm at a Reynolds number of 8.1×10^6, well into breakdown, is lower than the maximum coherence at $Re = 2.0 \times 10^6$, indicating that the vertical scale of disturbances has decreased due to the boundary layer breakdown. However, the coherence in the interior of the boundary layer and above the boundary layer edge is higher, indicating that this scale of disturbance is more uniformly distributed over the boundary layer. Power spectra taken at $Re = 8.1 \times 10^6$ (Fig. 3-2) show that disturbance energy is distributed across a broader range of frequencies due to the boundary layer breakdown. Coherence measurements near the maximum energy point in the boundary layer (Fig. 3-7) show that at a Reynolds number of 2.0×10^6, coherence on this scale is limited to the second mode and lower frequencies. At a Reynolds number of 8.1×10^6, the peak coherence is lower, but the high-frequency coherence increases, reflecting a coherent high frequency component of the flow.

Phase information for vertically separated probes is typically presented as a "structure angle," θ, for turbulent boundary layers. The structure angle is determined by the time delay between the top and bottom probes as $\theta = \tan^{-1}(\xi_y\,/\,c_r\tau)$, where τ is obtained from the cross-spectrum phase angle between the top and bottom probe. Structure angles must be interpreted differently for second mode waves than for organized turbulent structures, since second mode waves are periodic in the streamwise direction. Structure angles for second mode waves represent the inclination of a line of constant phase in the $x - y$ plane. Examination of this angle gives some indication of how the eigenstructure of the second mode wave evolves into turbulent structures. Structure angles for all of the Reynolds numbers tested are shown in Fig. 3-8. Data are not presented where the coherence is less than 0.05. The angles for Reynolds numbers between 2.0×10^6 and 6.1×10^6, inclusive, are for the peak second mode frequency. The angles for $Re = 8.1 \times 10^6$ were obtained from the cross spectrum at $f\,\delta/U_e = 0.5$. Broadband results at this Reynolds number (not shown) are similar in shape, but about 8 ° higher. The convection velocity, c_r, was taken equal to $0.95\,U_e$. This is appropriate for the lower Reynolds numbers, but is probably an overestimate for $Re = 8.1 \times 10^6$. Refs. 16-19 indicate normalized convection velocities between 0.8 and 1.0 for compressible turbulent and transitional boundary layers. A convection velocity of 0.8 would increase the measured wave angle by approximately 8 °. The structure angles at $Re = 8.1 \times 10^6$ show a relatively constant angle across the boundary layer of approximately 25° to 30°. This is in general agreement with the results of Owen and Horstmann[16,19] for low frequency disturbances in a hypersonic turbulent boundary layer for $y\,/\,\delta \leq 0.6$. The present data, however, do not show the structure angle increasing with y, as Owen and Horstman[16,19] do, a trend which was also observed by Spina et al.[18] in a Mach 3 turbulent boundary layer. Structure angles are also generally less than observed by Spina et al. [18] These results indicate that the boundary layer has not relaxed to a fully turbulent structure at this Reynolds number.

The second mode waves show a much different structure. Their structure angle within the boundary layer is generally less than the structure angle at $Re = 8.1 \times 10^6$. This structure angle decreases with y to a minimum of approximately 15° at $y / \delta = 0.7$. Above the boundary layer edge, the inclination angle is higher at these Reynolds numbers compared to $Re = 8.1 \times 10^6$. This second mode structure retains its identity through a Reynolds number of 6.1×10^6, although the change in structure angle begins to become evident at this Reynolds number. The structure angle changes abruptly as the boundary layer breaks down between $Re = 6.1 \times 10^6$ and 8.1×10^6.
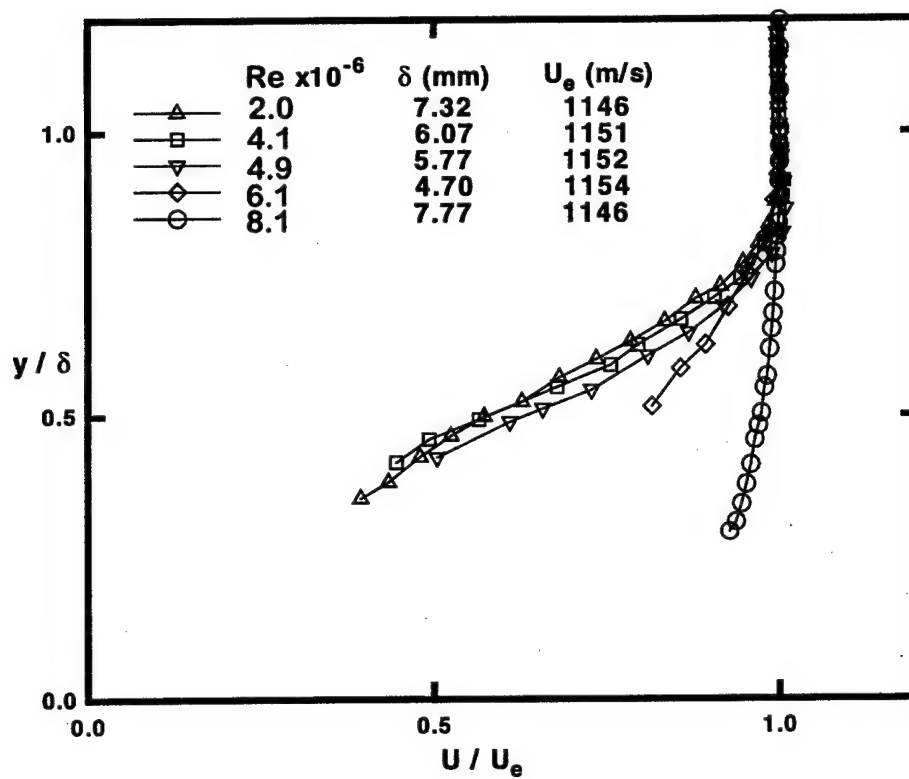
Figure 3-1. Mean boundary layer profiles.
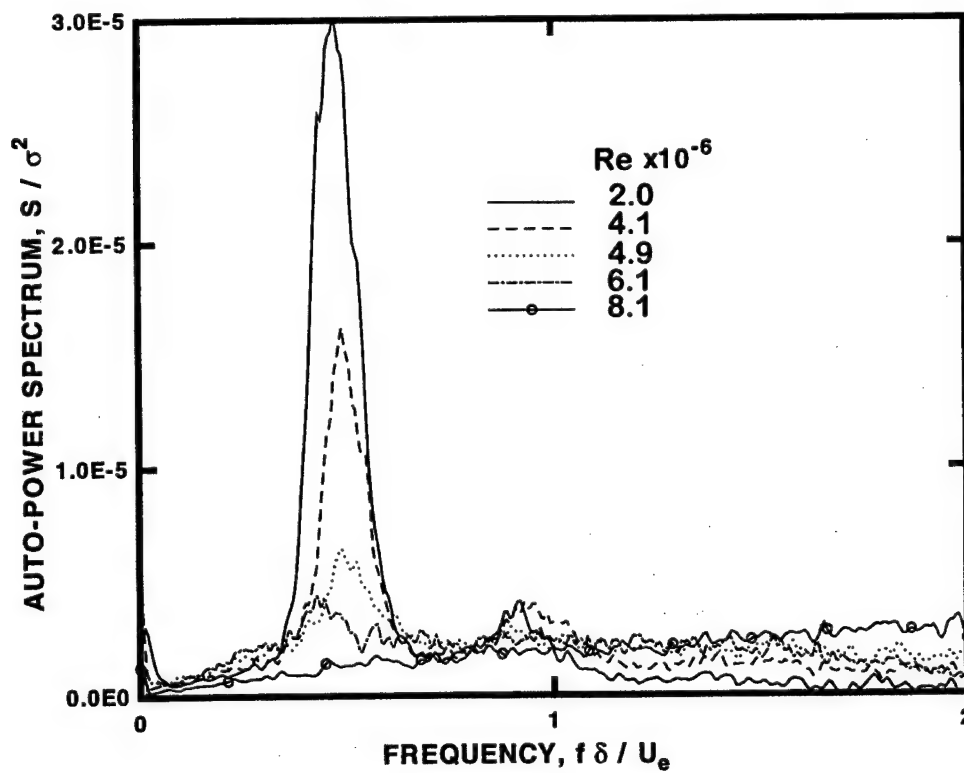
Figure 3-2. Power spectra at maximum energy location.
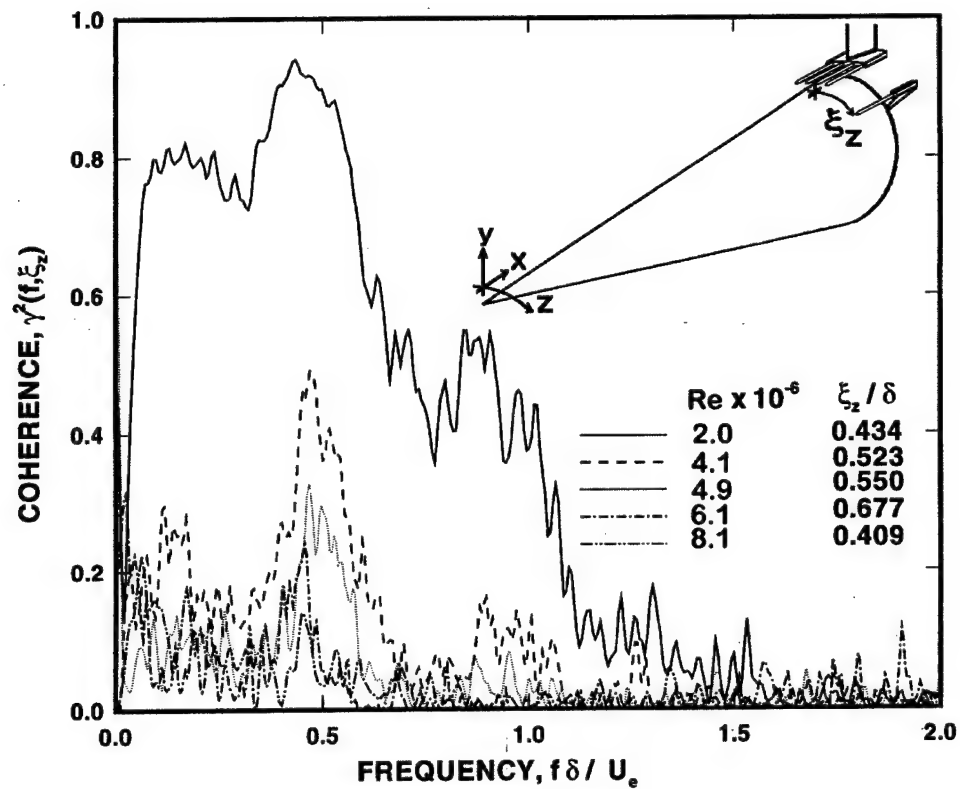
Figure 3-3. Coherence function at minimum z-separation.
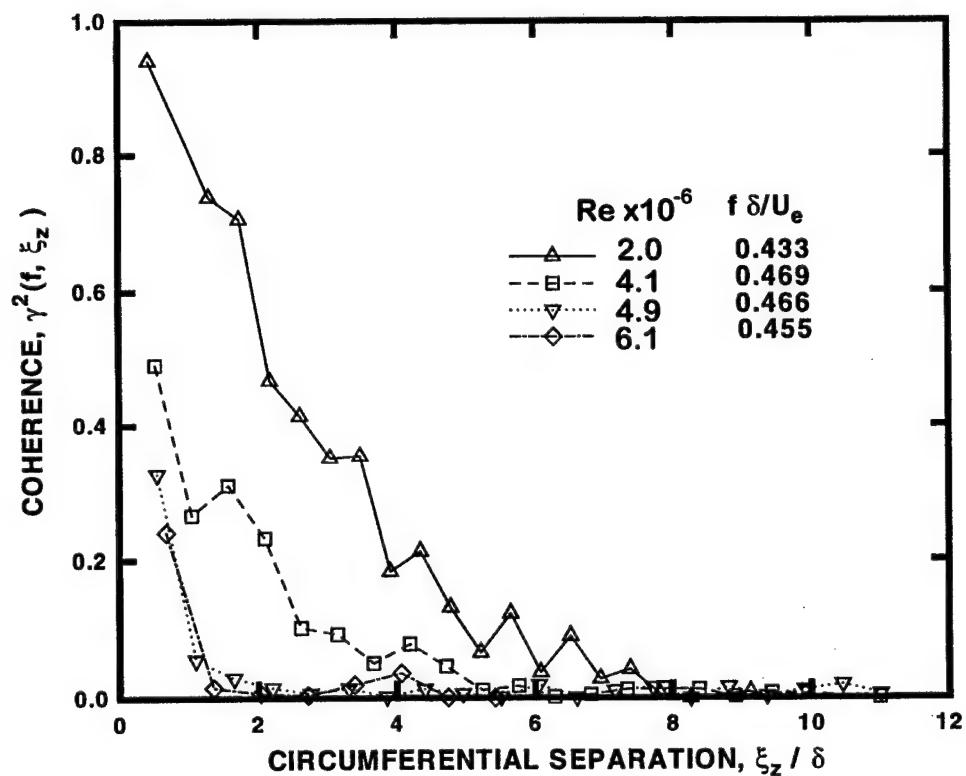
Figure 3-4. Peak second mode coherence vs. circumferential separation.
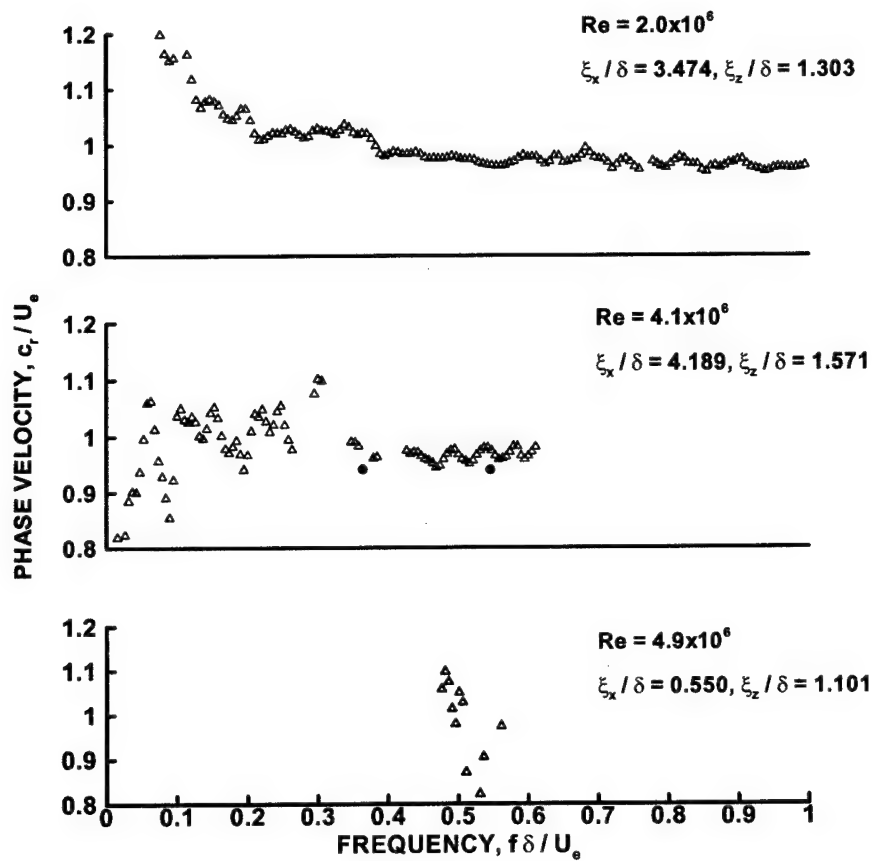
Figure 3-5. Phase speed as a function of frequency: solid circles at $Re = 4.1 \times 10^6$ are computational results of Mack.[7]
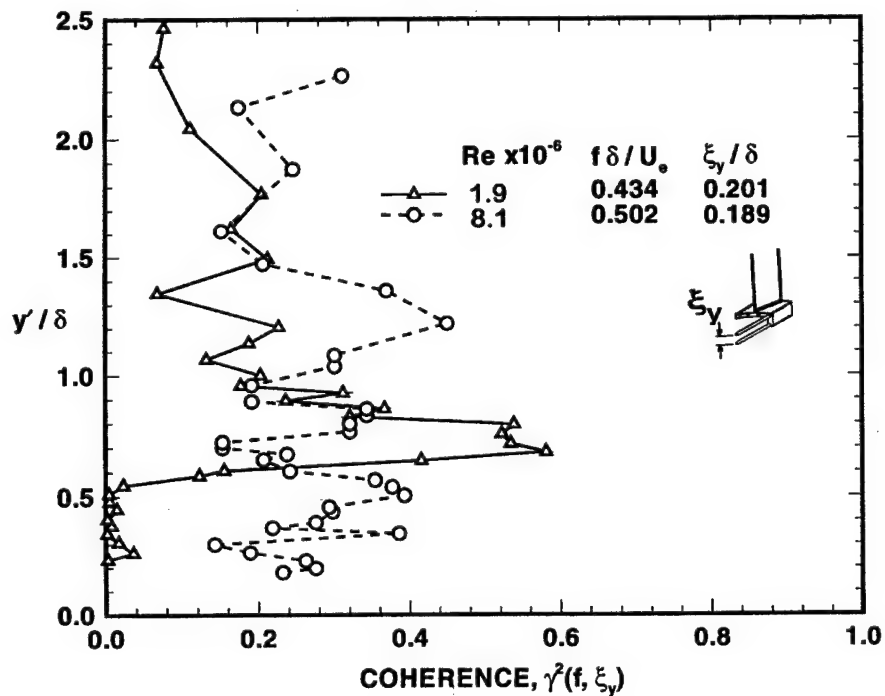
Figure 3-6. Coherence for vertical probe separation through boundary layer.
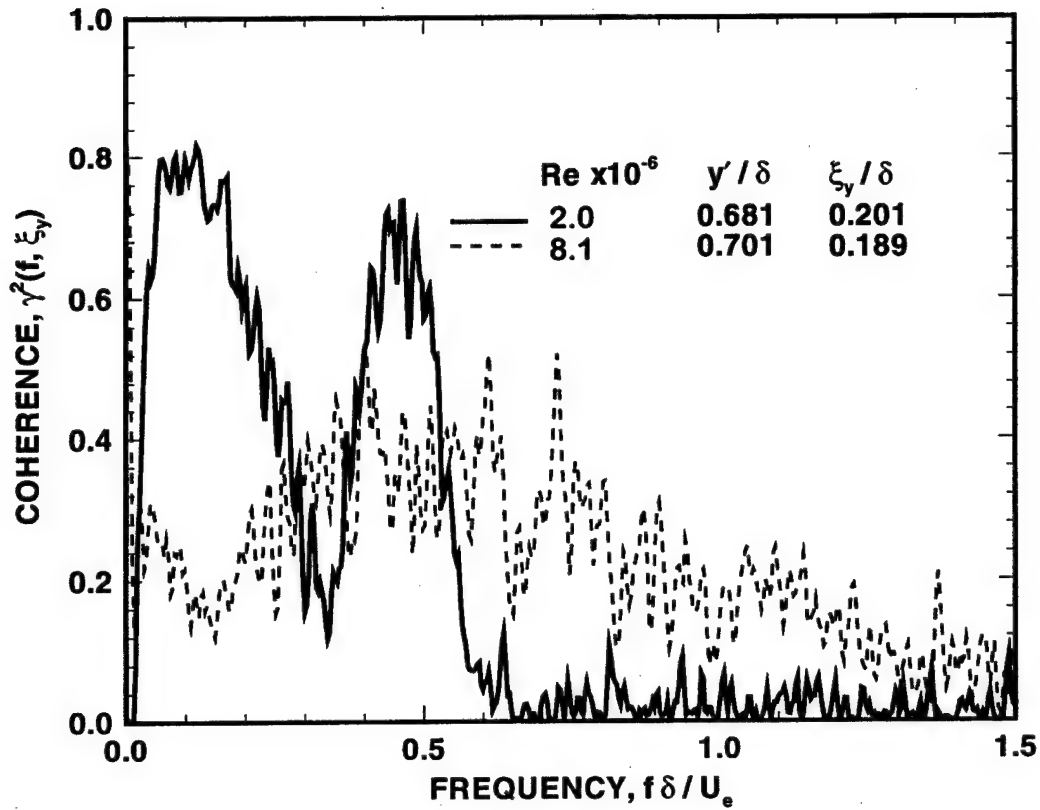
Figure 3-7. Coherence for vertical probe separation vs. frequency near maximum energy location in boundary layer.

Figure 3-8. Structure angle variation through boundary layer.

4. CIRCULAR CONE ENSEMBLE-AVERAGED STRUCTURE

Circumferential Probe Separation

Broadband space-time cross correlation coefficients for circumferential probe separation data at x-Reynolds numbers of 2.0×10^6, 4.1×10^6, and 4.9×10^6 are shown in Fig. 4-1. The circumferential separation, ξ_z, is normalized by the boundary layer thickness, and the time delay τ is normalized by $\del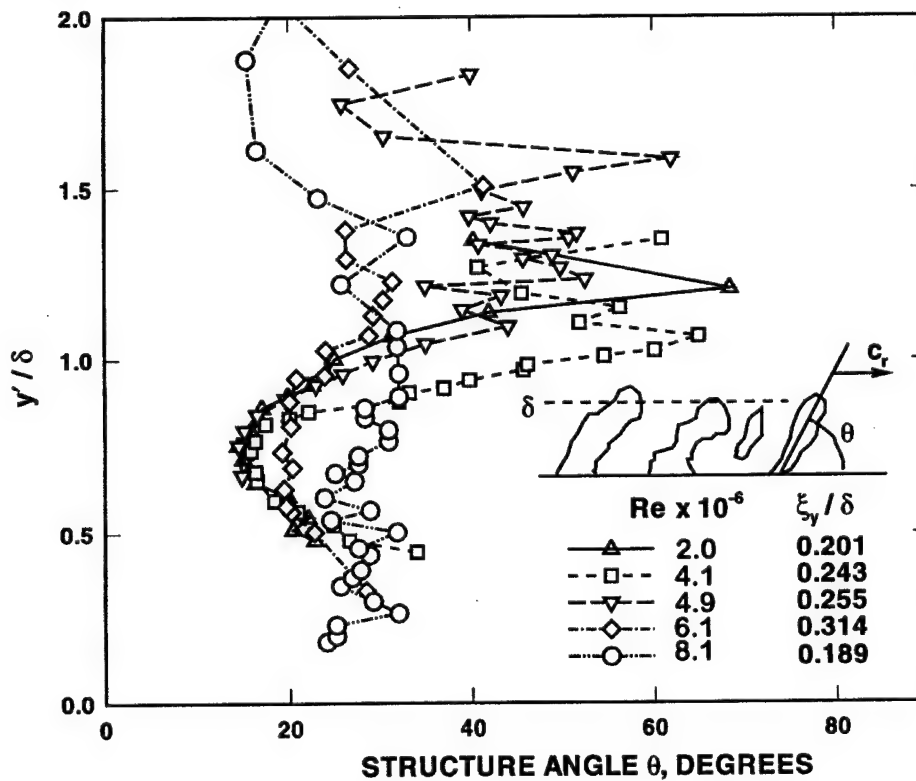ta / U$. Since the disturbances convect at near the edge velocity, the τ axis approximates a streamwise separation normalized by δ. The disturbances are periodic in time (or streamwise direction), with a wavelength of approximately two boundary layer thicknesses, which is the second mode wavelength. This is expected, since spectra show the second mode to be dominant. The correlation is modulated in time and space, with a maximum at zero time delay, and drops off with increasing τ, approaching 0 at $+/- 4 \tau U / \delta$, reflecting the limited streamwise coherence of the signal and its packet structure.

Although Fig. 4-1 resembles wave packets observed by Gaster,[11,50] one must recall important differences between Fig. 4-1 and Gaster's results. Gaster presented contours of velocity fluctuations which were obtained by placing a hot wire at various x,z locations downstream of the disturbance source and ensemble averaging the signal. The Fig. 4-1 results were obtained by cross correlating two circumferentially separated probes. The second mode packets are presumed to be generated upstream, with some random distribution in time and space due to the stochastic nature of the freestream input disturbances. Fig. 4-1 thus presents a region in time and space over which second mode disturbances are coherent, and does not necessarily represent a disturbance amplitude level. The circumferential scale over which the signal is coherent is approximately 7.5δ or less for $Re \leq 4.1\times10^6$.

Since the peak occurs at zero time delay for all circumferential separation, the second mode waves are, on average, two-dimensional, without any preferred obliquity. Since the cross correlation was reconstructed from the ensemble averaged cross spectrum, this is not unexpected. A random distribution of positively and negatively skewed waves would tend to cancel out during the ensemble averaging process. The instantaneous wave angle is addressed in the next section.

There is no evidence of a circumferential periodicity developing as Reynolds number increases, as might be expected from a subharmonic. Some variation in the optimum time delay with ξ_z is evident in the cross correlation obtained at $Re = 4.1\times10^6$. The predominant variation with Reynolds number is in the amplitude and circumferential scale of the correlation. Disturbances remain correlated out to a slightly larger ξ_z separation at $Re = 2.0\times10^6$ compared to 4.1×10^6. Between $Re = 4.1\times10^6$ and 4.9×10^6 there is a drastic rolloff in the circumferential correlation, although there is still a distinct streamwise periodicity at the second mode wavelength. Previous measurements[41] correlated $Re = 4.1\times10^6$ with transition on this configuration. The drop in correlation between these two Reynolds numbers indicates a rapid transition from the circumferentially organized second mode waves to structures with a much smaller circumferential scale. The transition front observed on shadowgraphs is observed to fluctuate upstream and downstream to some degree. The observed cross correlation is probably the result of second mode wave packets alternated with turbulent, or quasi-turbulent flow which is circumferentially coherent only on a lesser scale.

A wavenumber spectrum derived from the circumferential correlations at 68 kHz (near the second mode peak at $Re = 2.0\times10^6$) is shown in Fig. 4-2. The filtered cross correlation for $f = 68$ kHz at zero time delay was Fourier transformed with respect to circumferential separation to obtain the wavenumber spectrum. The data

are normalized so that the area beneath the curve is one. The Nyquist, or maximum resolvable, wavenumber k_N, is equal to one-half the spatial sampling frequency in analogy with the temporal Nyquist frequency. Spatial anti-alias filtering is not possible with this configuration, but the roll-off in the wavenumber spectrum at higher wavenumber indicates that a significant portion of the higher wavenumber content was captured. The Nyquist wavenumber is 2.3 times the second mode streamwise wavenumber, and corresponds to an azimuthal wavenumber of 108. The lowest azimuthal wavenumber resolvable is 13.5. Note that if the circumferential extent of the wave packet is limited, there is no requirement that the azimuthal wavenumber be an integer. The circumferential wavenumber spectrum peaks at low wavenumber, but some energy content is distributed over higher wavenumbers.

Correlations were obtained in the freestream (upstream of the model bow shock) with the same probe configuration used for circumferential correlations in the boundary layer. The low signal level in the second mode frequency band in the freestream makes interpretation difficult. Donaldson and Coulter[40] showed that the shape of the freestream spectra was similar at different Reynolds numbers, but the maximum resolvable frequency increased with increasing unit Reynolds numbers. Their measurements at $Re_u = 9.8 \times 10^6$ per meter show 0.07% mass flux and 0.013% total temperature fluctuations between 60 and 70 kHz, which is the second mode frequency band at $Re_u = 2.0 \times 10^6$ per meter. This Reynolds number is a worst case. Since the freestream spectrum decreases with increasing frequency, the percentage freestream fluctuation in the second mode band drops as tunnel unit Reynolds number increases, due to the increasing second mode frequency. Freestream cross spectra were obtained at $Re_u = 3.9 \times 10^6$ per meter in the current experiment. The coherence obtained from the cross spectrum in Fig. 4-3 show the signal to be uncorrelated above 50-75 kHz at minimum z-separation in the freestream. The phase shows a large rms variation due to the low coherence level, but appears to be distributed about zero.

Vertical Probe Separation

The phase angle obtained by traversing two probes with a fixed vertical separation through the boundary layer was compared to linear stability calculations. The phase angle obtained from linear stability theory is the phase of the instability wave relative to the phase at some reference location. The phase angle obtained from the measured cross spectrum in this experiment is really the difference in disturbance phase between the two y-locations. Therefore, a second order Runge-Kutta integration of the measured phase angle was carried out before it was compared to computation. Phase was referenced to zero at the first measurement point. A second consideration is that the phase depends on the quantity considered. The hot film anemometer voltage is a combination of its response to total temperature and mass flux fluctuations. Therefore, it is necessary to consider the computed phase of both total temperature and mass flux fluctuations.

The vertical probe separation was fixed at 1.47mm. Since the boundary layer thickness varied with tunnel unit Reynolds number, the probe separation in terms of δ varied from 0.189 δ to 0.314 δ. The effect of this vertical separation on the measured phase was assessed by simulating the measurement with the computed phase. The difference in the computed phase at the experimental y-locations was integrated using the same Runge-Kutta procedure used on the experimental data. The results in Fig. 4-4 show that the probe separation does indeed smear out the phase angle, but this smearing amounts to at most a 30 ° error.

Experimental phase is compared to computed phase in Fig. 4-4. The experimental results agree with computed phase for total temperature fluctuations. The relative sensitivity of the hot film to total temperature and mass flux fluctuations depends on the hot film overheat ratio. At low overheats, the film is more sensitive to total temperature than mass flux fluctuations. The overheat ratio for the data shown in Fig. 4-4 was 13% (the film resistance was 13% higher than its resistance at recovery temperature). The Fig. 4-4 results are thus consistent with the relatively low overheats used in this experiment, and indicate that the probes were responding primarily to total temperature fluctuations. These results show that even with the relatively large probe separation used in this experiment, this technique is useful for mapping disturbance eigenfunctions.

Broadband correlations derived from measurements made with probes separated vertically and traversed through the boundary layer are shown in Fig. 4-5. Since these measurements were made with a fixed probe separation, the reconstruction of the correlation contours requires some additional effort, similar to that described by Spina et al.[18] The survey point nearest the wall is taken as a reference. This correlation gives an optimum time delay for a fixed probe separation at this point in the boundary layer, $\tau_{max}(y_1)$. Given $\tau_{max}(y_1)$

and the distance between this point and the next survey point, $\Delta y = y_2 - y_1$, the correlation at y_2 is indexed in time by $(\Delta y / \xi_y) \tau_{max}(y_1)$. Since the zero of the time delay axis is arbitrary in this scheme, the contours for convenience have been time-shifted to place the maximum positive correlation near the boundary layer edge at zero time delay.

The correlation should, in the context of linear stability theory, be unity across the boundary layer at the optimum time delay for each vertical point. Due to the presence of background disturbances and the extremely low signal level away from the edge of the boundary layer, the correlations at the lower Reynolds numbers drop off above and below the maximum energy location. The correlation contours thus reflect, to a certain extent, the signal-to-noise ratio. As the Reynolds number increases, the maximum correlation extends farther into the boundary layer. This indicates that the disturbance level in the interior of the boundary layer is increasing as the boundary layer progresses to turbulence.

The second mode waves at the lowest Reynolds number are periodic, with a streamwise wavelength of approximately two boundary layer thicknesses. The correlation persists several second mode wavelengths away from the zero reference. The waves tend to have a flattened or elongated structure. This agrees qualitatively with shadowgraphs of "rope" waves shown in Fig. 4-6 for the same configuration. Since the rope waves appear near boundary layer breakdown and have approximately the same wavelength as the second mode, they are most likely the second mode in a late, nonlinear stage of development. One must be careful not to make too literal a comparison between the shadowgraphs, which are images of the second derivative of density, and correlations of total temperature. Nevertheless, both show highly inclined wavefronts, i.e., large phase changes across the boundary layer. As the Reynolds number increases and the boundary layer begins to transition, the streamwise coherence length decreases and the disturbances begin to stand more erect (i.e., their phase shift in the y-direction decreases). At the highest Reynolds number, the angle between the correlation contours and the wall have increased further, reminiscent of typical "turbulent structures" seen in boundary layers.[16,18,19] Also, the dominant disturbances have shifted to a shorter wavelength, reflecting the spread of energy from the second mode to higher wavenumbers.

Bicoherence Analysis

Cross-bicoherence analysis between streamwise separated probes was carried out. Bicoherence on single channel measurements was also carried out. The bicoherence, defined as

$$b^2(f_1, f_2) = \frac{\left| E\left[X(f_1) X(f_2) X^*(f_1 + f_2) \right] \right|^2}{E\left[\left| X(f_1) X(f_2) \right|^2 \right] E\left[\left| X(f_1 + f_2) \right|^2 \right]}$$

(4-1)

is a measure of nonlinear phase locking among frequency components in a single signal.[51] The cross bicoherence between signals x and y,

$$c^2(f_1, f_2) = \frac{\left| E\left[Y(f_1 + f_2) X^*(f_1) X^*(f_2) \right] \right|^2}{E\left[\left| X(f_1) X(f_2) \right|^2 \right] E\left[\left| Y(f_1 + f_2) \right|^2 \right]}$$

(4-2)

quantifies nonlinear phase locking among frequency components between two signals.[52] The bicoherence and cross-bicoherence vary from zero to one, where one indicates total quadratic coupling.

The cross-bicoherence was near zero at all Reynolds numbers in this experiment. Two factors probably account for this. First, at the lower Reynolds numbers, there was little nonlinear coupling. Second, the streamwise separated probes were also separated in the circumferential dimension by 6.35 mm to avoid interference. At higher Reynolds numbers, the circumferential correlations between probes dropped so rapidly that even at the minimum separation there was very little correlation.

The bicoherence measured at $Re = 4.1 \times 10^6$, shown in Fig. 4-7, is essentially identical to the bicoherence measured using hot wire, rather than hot film, probes, and measured on the same model during a different test entry.[15] This emphasizes the repeatability of this nonlinear interaction, which has been observed in other boundary layers subjected to broadband input. Higher harmonics were observed in hypersonic transition in

quiet facilities[4,5] and in subsonic flow with broadband acoustic input and roughness strips for acoustic receptivity.[6] The bicoherence measured at $Re = 4.9 \times 10^6$, shown in Fig. 4-8, shows a broader range of nonlinear interactions. Nonlinear interaction of the subharmonic with itself and other frequencies is apparent in the bispectrum, although the subharmonic is not pronounced in the power spectrum.[3,15] The fundamental second mode also shows nonlinear interaction distributed across the spectrum. At both of these Reynolds numbers, the maximum bicoherence was approximately 0.4. This value is less than the maximum of one due to electronic noise and flow fluctuations.[15]
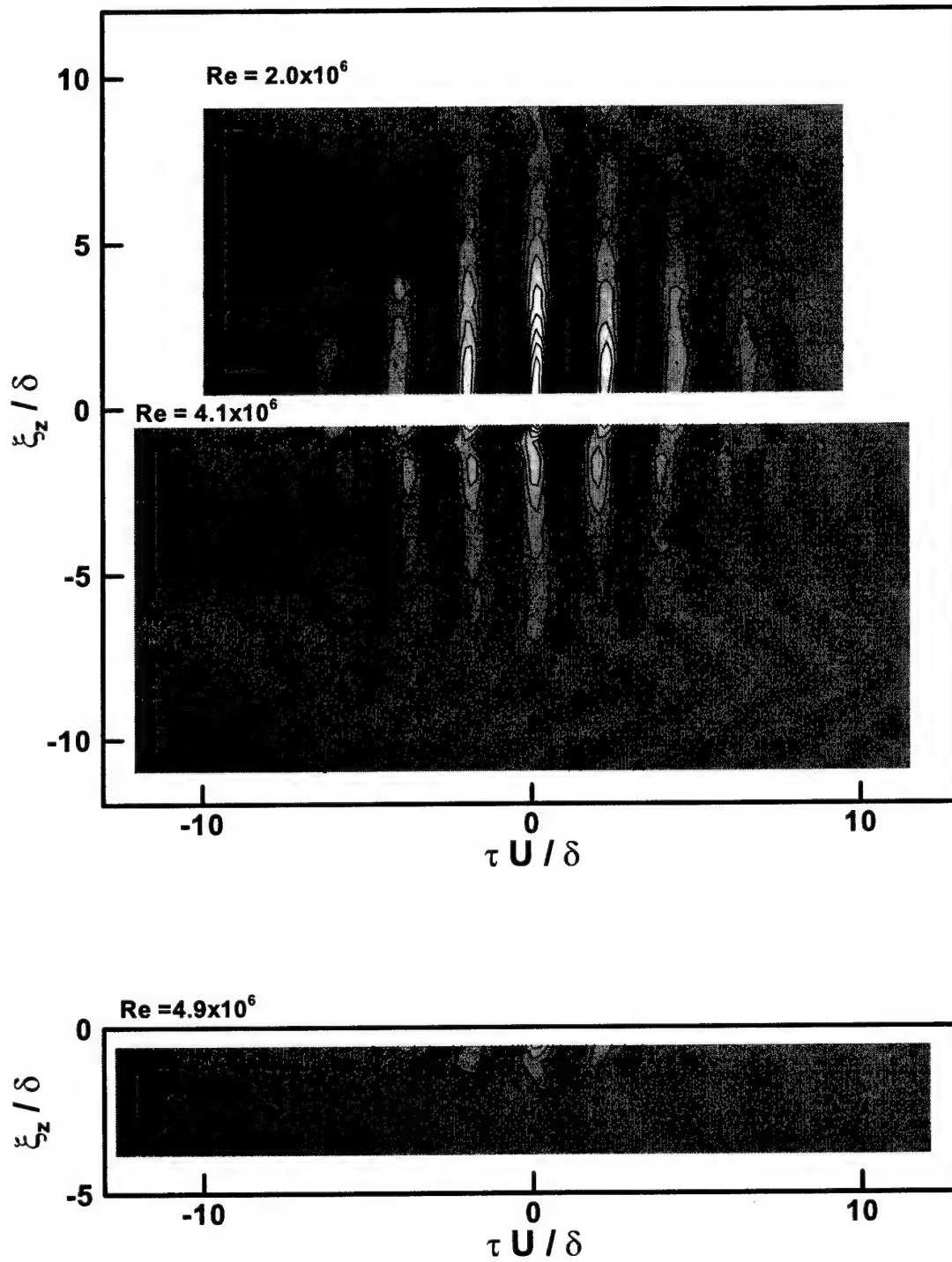
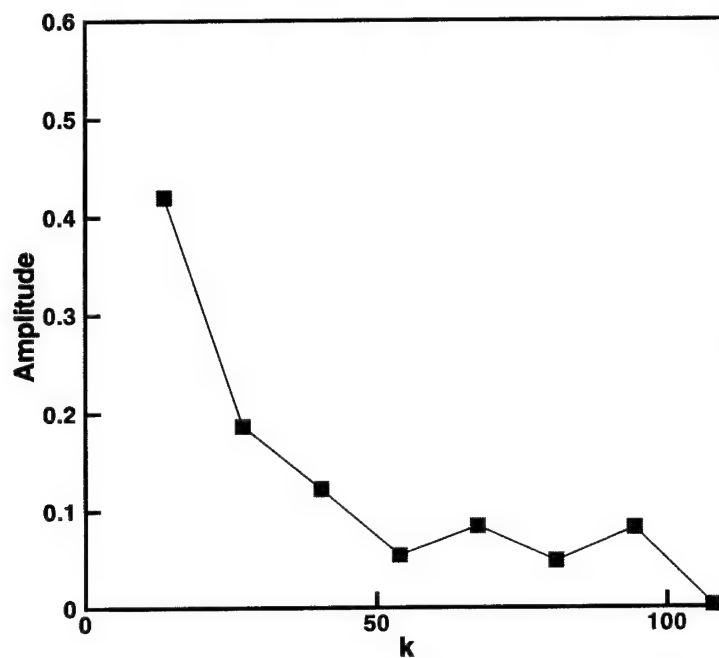Figure 4-1. Circumferential correlations at $Re = 2.0 \times 10^6$ and 4.1×10^6, and 4.9×10^6.

Figure 4-2. Circumferential wavenumber spectrum for f= 68 kHz at $Re = 2.0\text{x}10^6$.
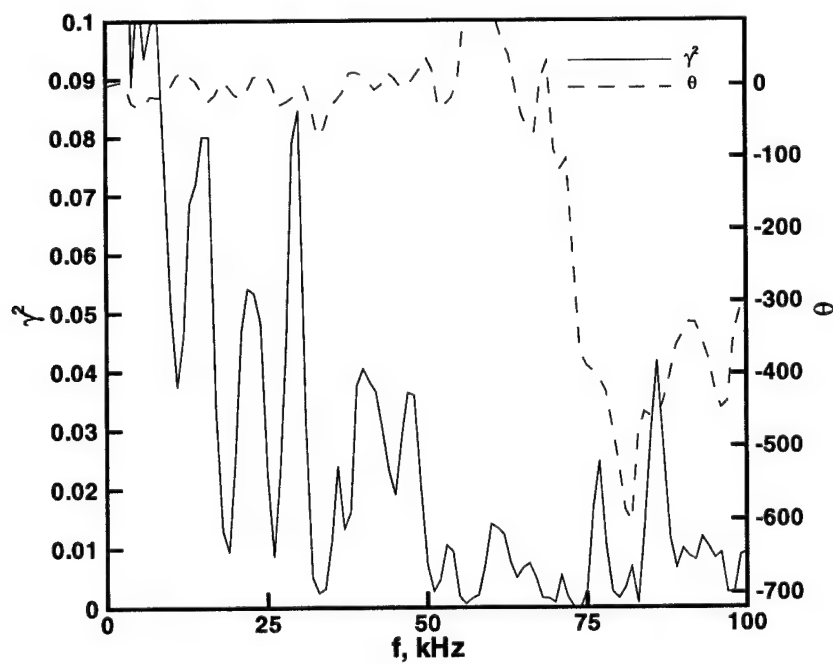

Figure 4-3. Freestream coherence and phase.
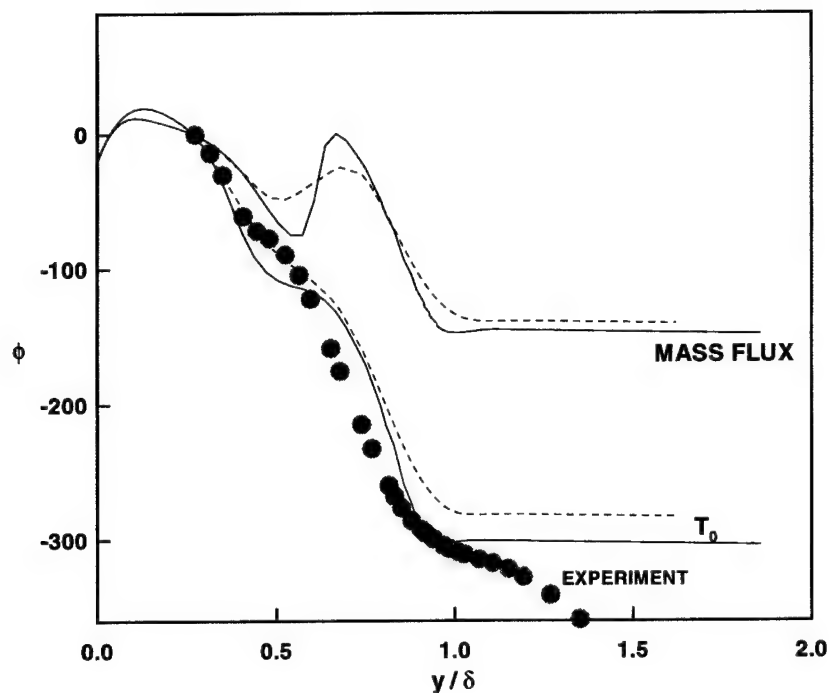
Figure 4-4. Phase angle through boundary layer. Symbols are experimental results, lines are computation. Dashed lines indicate effect of finite probe spacing on computed phase angles.
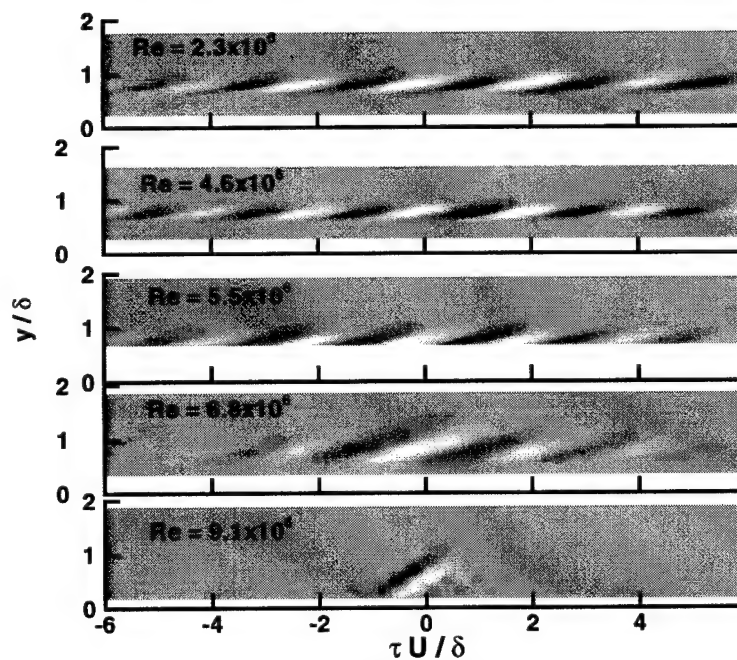

Figure 4-5. Vertical correlations.
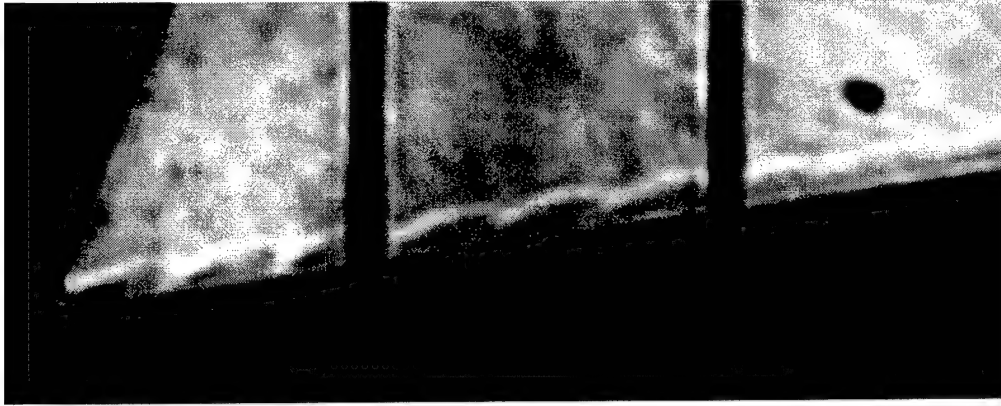
4-7

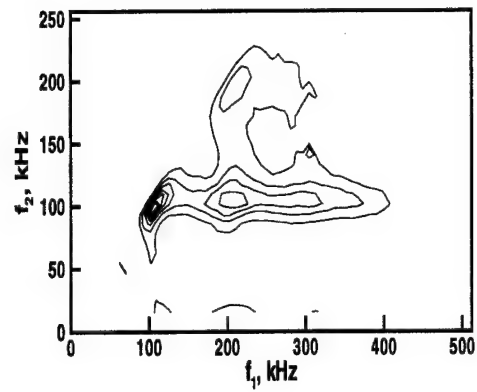Figure 4-6. Shadowgraph of rope waves. Flow is from left to right.

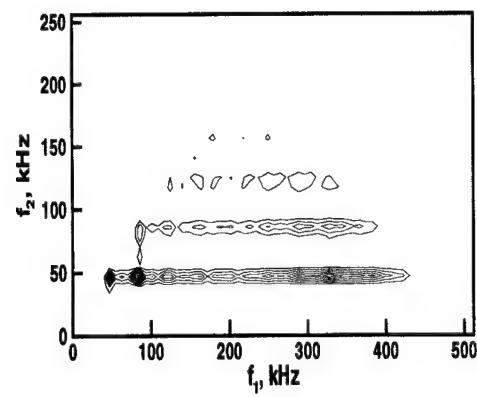Figure 4-7. Bicoherence at $Re = 4.1\text{x}10^6$. Contour interval is 0.05.

Figure 4-8. Bicoherence at $Re = 4.9\text{x}10^6$. Contour interval is 0.05.

4-8

5. CIRCULAR CONE TIME RESOLVED STRUCTURE

Wave packets in boundary layer stability

Since the hot film signal appeared packet-like in nature, this aspect of the signal was examined in more detail. Wave packets appear to be a universal feature of 'natural' transition in a relatively low-disturbance environment. For a low-speed, flat-plate boundary layer flow, for example, the oscillograms presented in the famous experiments of Schubauer and Skramstadt[53] show a low-level signal alternating intermittently with high-amplitude 'bursts.' At hypersonic Mach numbers, Potter and Whitfield[54] observed packets of 'rope waves' in schlieren photographs of a hypersonic flow over a cone.

A number of researchers have examined a simplified wave packet problem, in which a short, localized pulse is introduced into a laminar boundary layer flow.[11,50,55,56] The resulting wave packet is studied as it travels downstream in the boundary layer. A short input pulse has a very broad and flat spectrum in frequency-wavenumber space, so all unstable modes tend to be excited evenly. After the transient component dies out, the wave packet takes on an asymptotic form that is independent of the initial conditions. In incompressible boundary layers, this form appears as a corrugated, kidney-shaped patch.[50,57]

A complication arises for wave packets in a hypersonic boundary layer. Linear stability theory identifies two important unstable modes, the Tollmien-Schlichting mode and second (Mack) mode. Linear stability theory also predicts that the most unstable first mode disturbance becomes increasingly skewed to the freestream direction as the Mach number increases from zero to the supersonic range, but that the most unstable second mode disturbance is oriented normal to the freestream.

As a disturbance of constant frequency travels downstream through increasing values of the Reynolds number, a skewed first mode component is initially most amplified, and later a two-dimensional second mode component is most amplified.[10] This result suggests that the development of a wave packet in a hypersonic boundary layer is significantly different from the analogous problem in incompressible flow, and that the asymptotic form of the wave packet is a strong function of Mach number and the streamwise station where the disturbance originates.

Further, the phenomenon of transition, in contrast to stability, depends on the total growth of boundary layer disturbances. Point disturbances are introduced randomly all over the boundary layer, and transition is caused by the flow that results from a sum over the histories of all the resulting wave packets.[1]

Kinematic Approach

A kinematic approach to the study of boundary layer disturbances is of interest because of the complexity of the dynamics of the transition process. Boundary layer transition data can be difficult to interpret in terms of normal modes when the disturbances are in the form of wave packets or when they grow into the nonlinear regime. Important kinematic features include the frequency of occurance of the packets, as well as their length scale, lifetime, orientation, and velocity. Valuable data for transition modelling can be obtained by tracking the changes in these features from the initial onset of instability, through the formation of Emmons spots, to the development of the organized structures observed in fully developed turbulent boundary layers.

A kinematic approach to describing wave motion was developed independently by Landau and Lifshitz[58] and Whitham.[59] This approach generalizes the idea of a traveling plane wave to a slowly-varying, quasi-planar wave train. A wave train Ψ is assumed to have the form:

$$\Psi(\vec{x}, t) = A(\vec{x}, t) \cos \phi(\vec{x}, t) \tag{5-1}$$

where A is the amplitude function and ϕ is the phase function.

The basic assumption is that, over space and time scales corresponding to one cycle of $\cos\phi$, the amplitude function A is approximately constant and the phase function ϕ is nearly linear (see Segel[60] for a more precise statement of this restriction). In consequence, the extrema of the wave train (the crests and troughs) coincide approximately with extrema of $\cos\phi$, so that lines of constant phase can be associated with wavefronts.

The angular frequency is defined to be the rate of decrease of the phase function with time ($\omega = -\partial\phi/\partial t$), while the wavenumber vector is defined as the gradient of the phase function ($\vec{k} = \nabla\phi$). Since the amplitude A has been assumed to be a slowly-varying function, the quantity $\omega/2\pi$, which represents the instantaneous rate at which cycles of $\cos\phi$ cross a given point, can be interpreted as the instantaneous rate that waves cross that point. Similarly, $k/2\pi$ can be interpreted as a local measure of the number of waves per unit length along the direction normal to a wave front.

The speed of a crest or trough identified with a particular value of the phase can be determined by taking the time derivative of the equation $\phi(\vec{x}, t) = $ const.:

$$\frac{d\phi}{dt} = \frac{\partial\phi}{\partial t} + \frac{d\vec{x}}{dt} \cdot \nabla\phi = 0 \tag{5-2}$$

where $\vec{x}(t)$ describes the trajectory of a point on the iso-phase surface, and $\vec{v} = d\vec{x}/dt$ is its velocity. Using the definition of the unit normal to the surface ($\vec{n} = \nabla\phi / |\nabla\phi|$), we get an expression fixing the normal component of the velocity:

$$\vec{v} \cdot \vec{n} = \frac{-\partial\phi / \partial t}{|\nabla\phi|} = \omega / k \tag{5-3}$$

Thus, an observer moving at a velocity with a component normal to the iso-phase surface equal to ω/k sees a constant phase. The component of the observer's velocity tangential to the iso-phase surface is arbitrary - wave motion parallel to the wavefront cannot be detected. Thus we define the phase velocity as $\vec{v}_p = (\omega/k)\vec{n}$, which is the velocity of the iso-phase surface normal to itself.

If we add the time derivative of the wavenumber vector to the gradient of the angular frequency we can derive an equation relating the two quantities.

$$\frac{\partial\vec{k}}{\partial t} + \nabla\omega = 0 \tag{5-4}$$

Under the assumption of nearly-planar waves, Equation (5-4) can be interpreted as an expression of wave conservation. To see this result, we integrate Equation (5-4) between two points $\vec{x}_0$ and $\vec{x}_1$ over a path C, and divide by 2π.

$$\frac{\partial}{\partial t} \int_C \frac{\vec{k}}{2\pi} \cdot d\vec{r} = \frac{\omega(\vec{x}_0)}{2\pi} - \frac{\omega(\vec{x}_1)}{2\pi}$$ (5-5)

The term on the left-hand-side represents the time rate of change of the total number of cycles of $\cos\phi$ over the path of integration. The terms on the right-hand-side represent the difference in rates at which cycles of $\cos\phi$ cross the points $\vec{x}_0$ and $\vec{x}_1$. Thus, under the nearly-planar wave assumption, the equation can be interpreted as follows: the rate of change of the number of waves along C is equal to the rate at which waves enter at $\vec{x}_0$ minus the rate at which waves leave at $\vec{x}_1$. In other words, quasi-planar waves retain their identity as they travel.

If the group velocity is defined as $\vec{v}_g = \partial \omega / \partial \vec{k}$, and we take the scalar product of the group velocity with Equation (5-4), we get:

$$\frac{d\omega}{dt} = \frac{\partial \omega}{\partial t} + \vec{v}_g \cdot \nabla \omega = 0$$ (5-6)

implying that an observer moving with the group velocity sees a constant frequency. An analogous equation for the wave number vector can be derived if $\omega = f(\vec{k})$, otherwise (e.g., $\omega = f(\vec{k}, \vec{x})$) the wavenumber vector changes for an observer moving with the group velocity.

The quasi-planar wave assumption seems to be consistent with experimental observations of boundary layer disturbances upstream of the breakdown to turbulence. Boundary layer properties typically vary slowly in the direction of propagation of a disturbance, and experimental data seem to be consistent with a nearly constant amplitude and approximately linear phase. Many flow visualization experiments show convincing wave trains.[13,61,62] Thus, the kinematic theory of wave motion is applicable to disturbances in transitional boundary layers, and can be used to define a number of parameters describing experimental measurements of wave packets. In particular, the frequency, wavenumber, phase velocity, group velocity, and wave identity are well-defined in the context of the kinematic wave theory, without reference to the underlying dynamics that cause the wave motion.

General Character of Signal

Sound radiation from the turbulent boundary layers on the tunnel side-walls is believed to be the primary source of disturbances driving transition for experiments in conventional supersonic and hypersonic wind tunnels.[3] For compressible flow, linear stability theory[1,63] predicts that boundary layer disturbances will be amplified in two frequency ranges, corresponding to the first and second modes. Measurements in the freestream of AEDC VKF-B[3] indicate that most of the energy content of the tunnel background noise is concentrated in a frequency range much lower than the characteristic frequency of the second mode instability ($f \approx U_e/2\delta$). In experimental data one would thus expect to see a second mode component arising from this 'quiet' frequency range, a relatively lower frequency first mode component driven by the tunnel background noise, and a modulation arising from the random nature of the tunnel noise.

Fig. 5-1 shows sample time-series plots at Reynolds numbers Re of 2.0×10^6, 4.1×10^6, 6.1×10^6, and 8.1×10^6. These data were obtained at the value of y'/δ where the highest signal energy was detected. The

streamwise station was held constant at $x = 896$ mm, and the Reynolds number was varied by changing the tunnel stagnation pressure.

The lowest Reynolds number case (Fig. 5-1a) shows the expected wave-packet character. There is a dominant periodic component in the signal with a relatively low frequency modulation, and relatively quiescent periods alternate with packets of high-amplitude fluctuations. At a somewhat higher Reynolds number (Fig. 5-1b), the quiescent periods are less frequent and the packets more prominent. As the Reynolds number is increased still further, the signals acquire a less regular character (Figs. 5-1c and 5-1d), although some of the features of the initial instability are still detectable even at the highest Reynolds number.

Plots of the corresponding power spectral densities (PSD) are shown in Fig. 5-2. The two lower Reynolds number cases (Figs. 5-2a and 5-2b) are dominated by a strong peak at the characteristic second mode frequency. Weak harmonics of this frequency are also evident in the plots, possibly indicating the initial onset of non-linearity in the transition process. There is suprisingly little energy content in the frequency range below the second mode. For higher values of the Reynolds number, the disturbance energy begins to be distributed over a range of frequencies (Fig. 5-2c), and eventually the instability breaks down into turbulence (Fig. 5-2d).

Figs. 5-3 and 5-4 show, respectively, time-series plots and probability density functions for four different stations in the boundary layer at a Reynolds number of $Re_x = 4.1 \times 10^6$. For the lowest station shown (Fig. 5-3a), the most striking features are high-amplitude, predominantly negative 'spikes' in the signal. The probability density function (Fig. 5-4a) shows a corresponding negative skewness. Higher in the boundary layer (Figs. 5-3b and 5-4b), the negative spikes become more frequent, and the negative skewness of the PDF becomes quite striking.

Between $y/\delta = 0.76$ and $y/\delta = 0.78$ there is a qualitative change in the behavior of the signal: the negative tail on the PDF is balanced by a positive tail (Fig. 5-4c) and both positive and negative "spikes" are seen in the time series plots (Fig. 5-3c). The highest intensity of fluctuations are detected in the vicinity of this change in behavior. (The maximum signal energy occurs at $y/\delta = 0.78 \pm 0.02$.) Still farther from the wall (Figs. 5-3d and 5-4d), the PDF fills out, eventually forming a symmetric, Gaussian distribution.

In summary, the single-point time-series data are dominated by the second mode instability. The signals are intermittent, consisting of a random modulation imposed on a periodic signal. Power spectra are dominated by a peak at the characteristic frequency of the second mode, with surprisingly little energy at lower frequency, where wind tunnel background noise would be expected to drive the first mode. A qualitative change in the signal behavior was observed across the y/δ station of maximum energy, presumably corresponding to the critical layer.

Disturbance Wave Orientation

One interesting aspect of the disturbance structure is the orientation in a surface parallel to the wall (x-z) represented by the skewness angle ψ. Over a range of supersonic and hypersonic Mach numbers, linear stability theory predicts that the most unstable second mode disturbance is oriented normal to the freestream ($\psi = 0$), and that the most unstable first mode disturbance is skewed to the freestream direction ($45° \leq \psi \leq 65°$ over $1 < M < 10$). Wave skewness was investigated experimentally by acquiring data from probes with a circumferential separation (ξ_z).

Fig. 5-5 shows an example of the broad-band cross-correlation for a Reynolds number of $Re = 4.1 \times 10^6$. The cross-correlation displays a periodic component with a time scale characteristic of the second mode instability and a larger scale decay in time reflecting the limited streamwise coherence of the disturbance wave packets in the flow. If skewed waves were present in the flow, a pair of extrema, symmetric about zero time delay, would be expected in the cross- correlations. For a convection velocity of $0.9U_e \approx 1.04$ mm/μsec, a probe separation of $\xi_z = 12.7$ mm, and a wave angle of $\phi = \pi/4$, there should be maxima at time delays of $\tau \approx \pm 12$ μs. Instead, the optimal correlation occurs at zero time delay for the present case as well as for the other Reynolds numbers for which data is available (not shown).

The skewness of the different disturbance modes may not be apparent in the cross-correlation because it contains no frequency-dependent information about the signals - the skewness may 'wash out' in the

calculation. An alternate way of looking at the two signals is through the cross-spectrum. Plots of coherence (e.g., Fig. 5-6) do show that the signals have frequency-dependent features: a low-frequency component that may be related to the first mode and/or wind tunnel noise, the second mode, and the first harmonic of the second mode.

If, over a range of frequencies, there were a constant time shift τ between the two signals, we would expect to see a linear segment with slope $2\pi\tau$ in a plot of the phase versus frequency. Fig. 5-7 shows the phase of the cross-spectrum for the $Re = 4.1 \times 10^6$ case. Surprisingly, there is no time delay detectable in the data.

To examine the possibility that the instantaneous orientation of the boundary layer disturbances was different from the ensemble-averaged orientation, the probability density function (PDF) of the phase of the cross-spectrum was computed. The phase PDF was computed by dividing each pair of contiguous records into windows of $2^6 = 64$ points (the window size was selected to correspond approximately to the characteristic time scale of the autocorrelation), computing the cross-spectrum and its phase for each pair of windows, and incrementing a two dimensional array with indices corresponding to the phase and the frequency. For the present circumferential probe separation, a bimodal distribution of the phase would be expected if skewed waves were present in the flow.

Fig. 5-8 shows the PDF of the phase for a Reynolds number of $Re = 2.0 \times 10^6$, plotted with frequency as a parameter. In this figure the horizontal axis corresponds to frequency in Hertz, the vertical axis corresponds to the phase, which ranges from $-\pi$ to π, and the contours correspond to the probability density. At the higher frequencies, there is essentially a uniform distribution of phase, as would be expected for uncorrelated noise. In the vicinity of the second mode frequency, however, there is a clear peak evident in the distribution of phase, centered near zero. A second peak is apparent at lower frequency.

Fig. 5-9 shows the corresponding results for a Reynolds number of $Re = 4.1 \times 10^6$. Again, a uniform distribution of phase is observed for relatively high frequency, and a distribution peaked near zero phase is seen in the vicinity of the second mode frequency. The low-frequency peak apparent in the previous case is also present here. The major difference between the two cases is that for the high Reynolds number case the distribution is broader in the second mode frequency range and there is more separation in frequency between the second mode and the low-frequency component of the data.

These results are consistent with two-dimensional waves traveling in the direction of the freestream: each crest or trough of such a horizontal wave would intersect both hot-film probes simultaneously, creating no phase difference in the two signals. There is no evidence of oblique waves in the data.

Summary

Two-dimensional, second-mode waves were detected in the Mach 8 flow over a 7° half-angle cone studied in the present project. No evidence of the first mode was found. Little energy was detected in the lower frequency range, and no evidence of wave skewness was apparent.

According to stability theory[10,63] the amplification of a boundary layer disturbance is very history-dependent in compressible flow. As a disturbance of constant frequency travels downstream in a compressible boundary layer, it is first amplified in the region of first mode instability, and farther downstream is amplified in the region of second mode instability. If disturbances originate at different streamwise stations (Reynolds numbers), as would be expected in a wind tunnel with background noise, early first mode growth might be averaged out by second mode amplification of disturbances originating farther downstream.

The problem with conventional transition experiments is that the origin - in space and time - of the disturbances entering the boundary layer is not known, so that it is not possible to examine a disturbance at a known stage in its amplification history. This question could be resolved by carrying out an experiment in a hypersonic flow similar to the experiment of Gaster and Grant,[50] in which a localized, short-duration disturbance was introduced into an incompressible boundary layer, and synchonized measurements were made downstream.
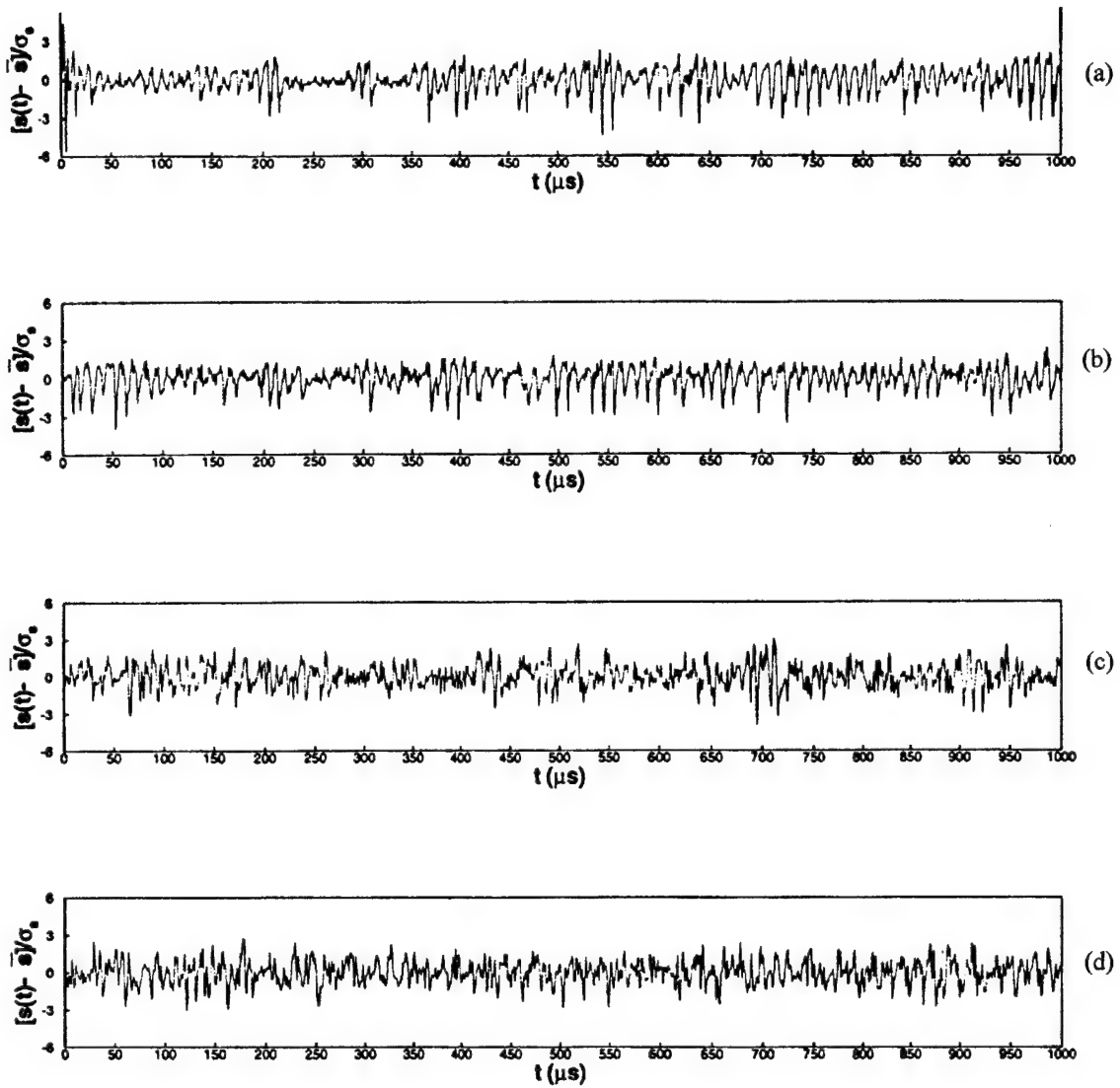
Figure 5-1. Time-series plots of the hot-film signal at the maximum energy station. (a) $Re_x = 2.0 \times 10^6$. (b) $Re_x = 4.1 \times 10^6$. (c) $Re_x = 6.1 \times 10^6$. (d) $Re_x = 8.1 \times 10^6$.
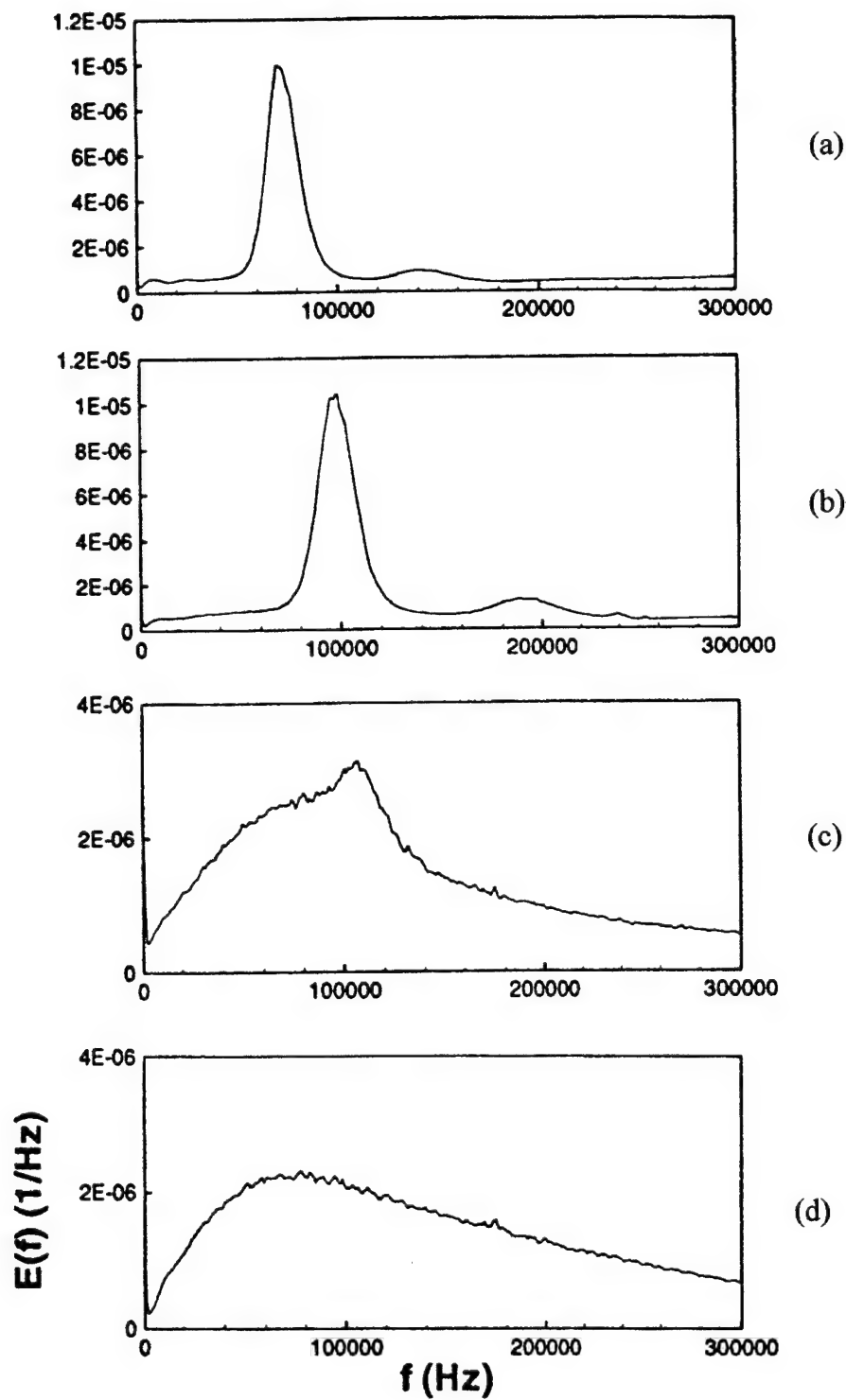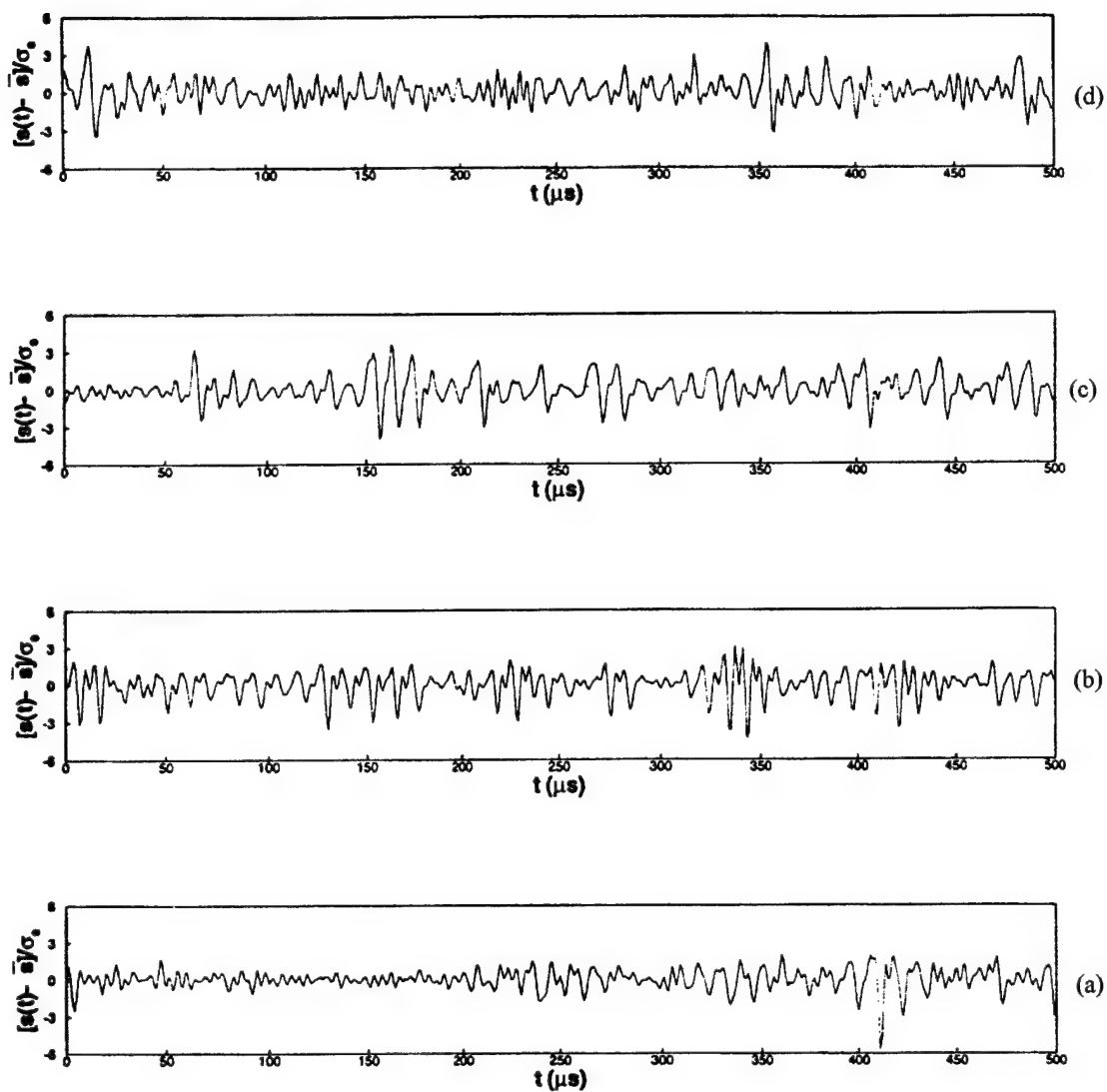
Figure 5-2. Power spectra at the maximum energy station. (a) $Re_x = 2.0 \times 10^6$. (b) $Re_x = 4.1 \times 10^6$. (c) $Re_x = 6.1 \times 10^6$. (d) $Re_x = 8.1 \times 10^6$.

Figure 5-3. Time series plots for four stations across the boundary layer at $Re_x = 4.1 \times 10^6$. (a) $y'/\delta = 0.64$. (b) $y'/\delta = 0.76$. (c) $y'/\delta = 0.78$. (d) $y'/\delta = 0.86$.
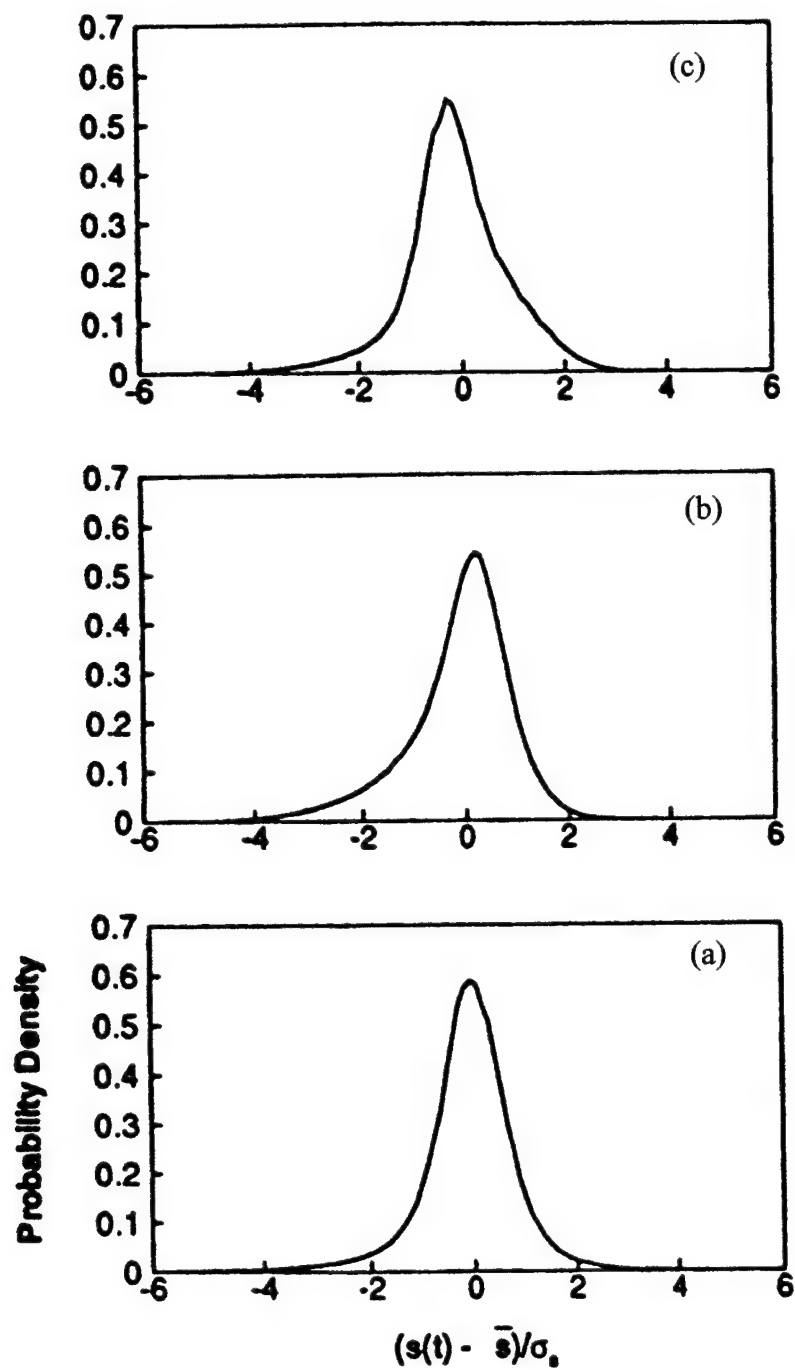
Figure 5-4. Probability density functions for four stations across the boundary layer at $Re_x = 4.1 \times 10^6$. (a) $y'/\delta = 0.64$. (b) $y'/\delta = 0.76$. (c) $y'/\delta = 0.78$. (d) $y'/\delta = 0.86$.
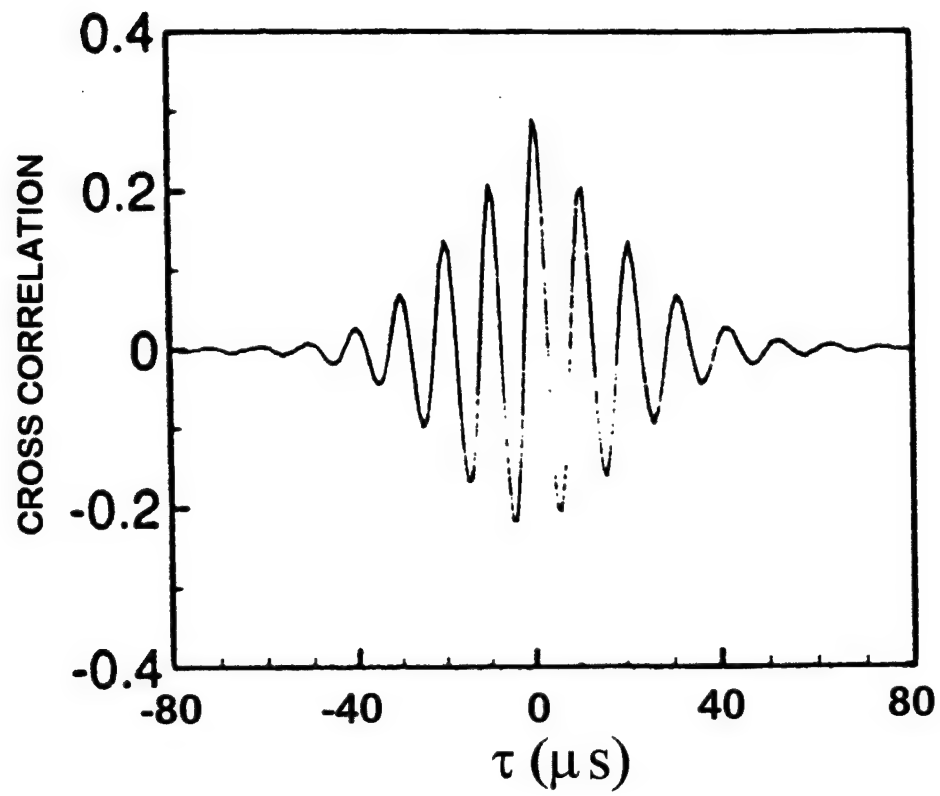
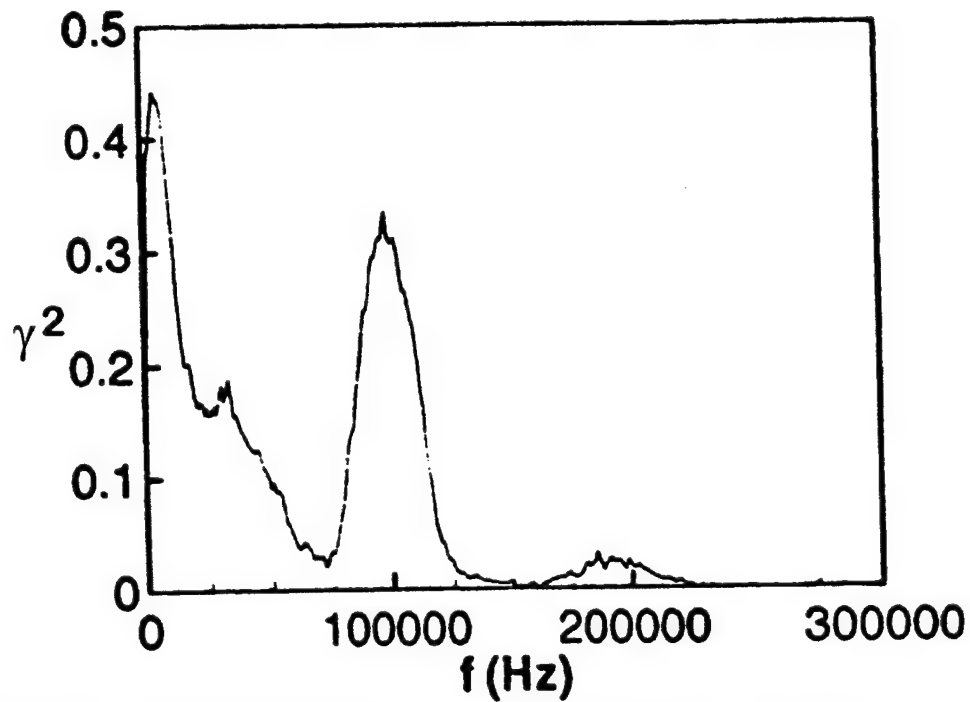Figure 5-5: Broad-band cross-correlation for $Re_x = 4.1 \times 10^6$ and $\xi_z/\delta = 2.1$.

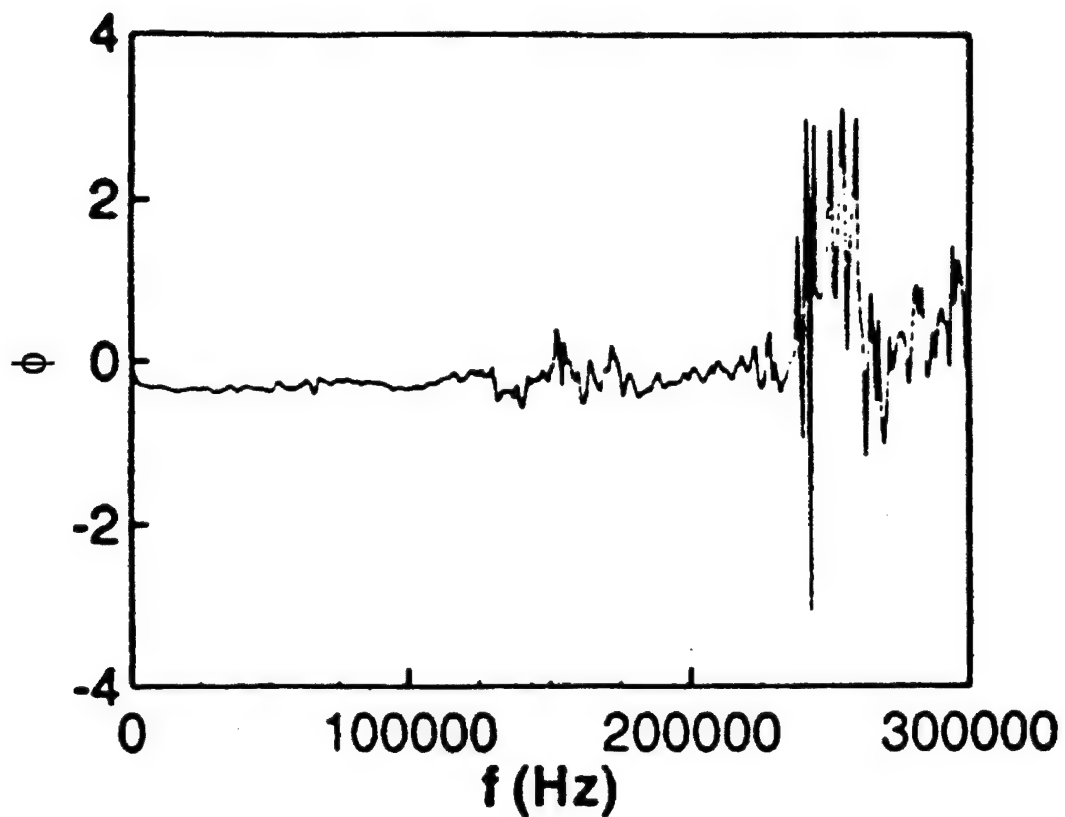Figure 5-6: Coherence derived from the cross-spectrum for $Re_x = 4.1 \times 10^6$ and $\xi_z/\delta = 2.1$.

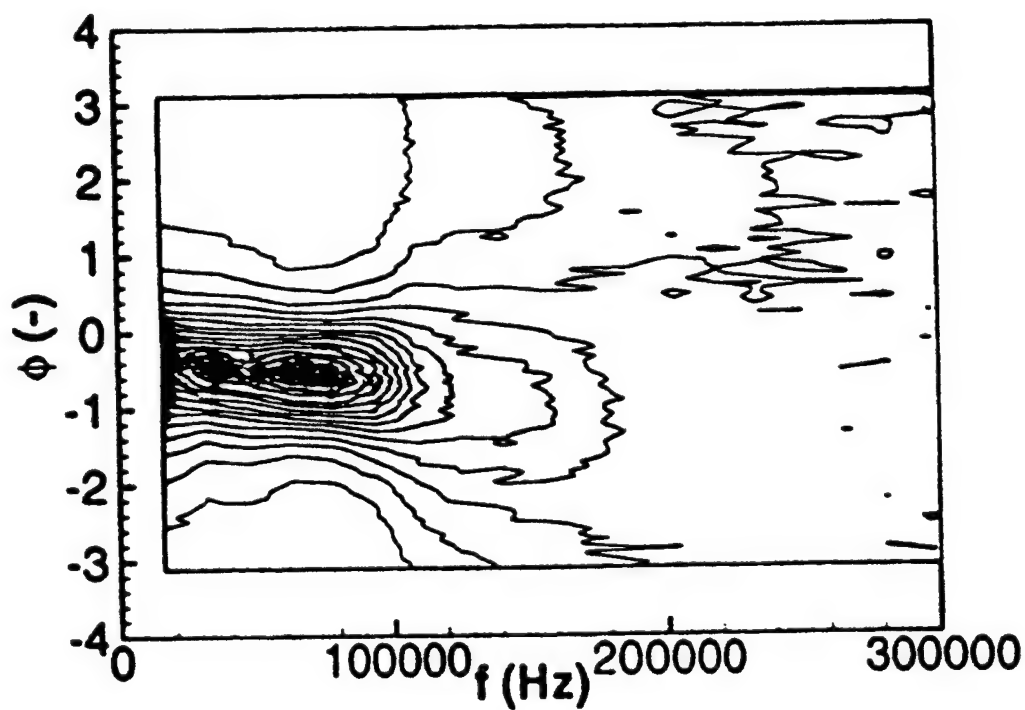Figure 5-7: Phase of the cross-spectrum for $Re_x = 4.1 \times 10^6$ and $\xi_z/\delta = 2.1$.

Figure 5-8: PDF of the phase as a function of frequency for $Re_x = 2.0 \times 10^6$ and $\xi_z/\delta = 1.3$. Contour interval 0.05.
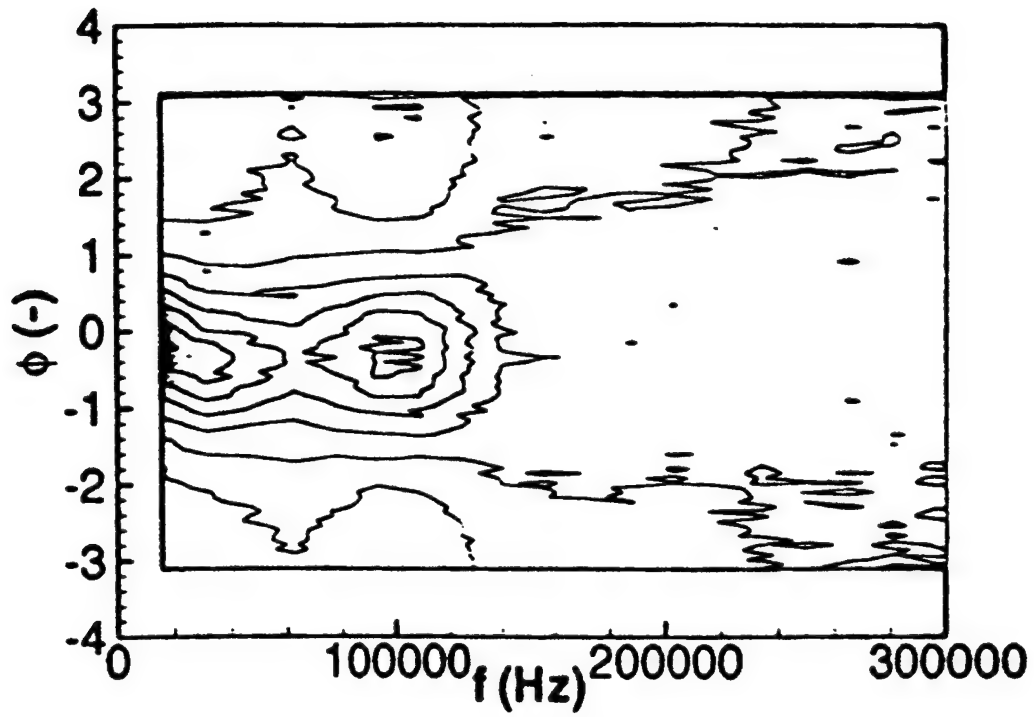
Figure 5-9: PDF of the phase as a function of frequency for $Re_x = 4.1 \times 10^6$ and $\xi_z/\delta = 2.1$. Contour interval 0.05.

6.   ELLIPTIC CONE COMPUTATION

Computational Procedure

Parabolized Navier-Stokes and linear stability computations were used to design the elliptic cone model. Computations were carried out for $e = 1.5$, 2.0, and 4:1 cross-sections for the expected nominal freestream conditions of Mach 7.95 and $Re_{u\infty} = 3.3 \times 10^6$ per meter. After the wind tunnel test, additional computations were carried out for the $e = 2.0$ configuration at the actual wind tunnel conditions. These detailed computations are compared to experimental results in Section 7. Section 6 compares computational results for the three configurations.

Most of the laminar boundary layer basic state computations were carried out using the UPS Parabolized Navier-Stokes code[64], as modified by Lockheed-Martin Tactical Aircraft Systems. The code uses a central difference scheme for inviscid fluxes and a fourth order smoothing model. All results, with the exception of heat transfer, are for adiabatic wall conditions. The e^{Malik} code[65] was used to calculate boundary layer stability.

The coordinate system is shown in Figure 6-1. The nose solution for the first 25.4 mm of each model was obtained with the Navier-Stokes Nose Solution Code (NSC). Both CFD codes employed shock fitting to model the outer boundary. The computational grid shown in Fig. 6-1 was generated by distributing points along the circumference of the model at each axial cross-section (x constant), and projecting the radial lines outward, normal to the body, in the yz-plane. The interior points were spaced algebraically in two radial layers. The inner layer resolved the boundary layer, and the outer resolved the remainder of the flowfield. Two spacings were employed in the inner layer. Near the wall, the spacing was 100% of even spacing within the inner layer. Grid points were spaced more closely at the edge of the boundary layer to resolve gradients there. Spacing at the boundary layer edge was 66% of even spacing. For the outer layer, the spacing at the shock was 150% of even spacing, and the spacing at the edge of the boundary layer was set to match the spacing of the neighboring point. Each layer contained approximately half of the total radial points. The UPS code automatically adapted the grid to keep the grid layer interface at the edge of the boundary layer. Solutions were confined to one 90 degree quadrant of the cone.

Grid resolution studies were conducted on the $e = 1.5$ and 2.0 configurations. The ijk grid dimensions were changed from 61x51x875 to 121x61x875. Only the fine grid results results are presented for these configurations. Only a 61x71x875 case was run for the $e = 4.0$ configuration. Results were insensitive to grid resolution except for the high-frequency amplification rates calculated near the top centerline. At 50 kHz, for example, the amplification results were about 10% lower when the boundary layer edge was more poorly resolved. Since this frequency range and region were of little consequence to the overall results, no further grid refinement was undertaken in this portion of the study. Detailed computations for the $e = 2.0$ configuration at the exact experimental conditions, reported in the next section, used a 121x51x875 grid.

The effect of numerical smoothing on the basic state can be very important to a linear stability code. Too much smoothing can change the boundary layer profile derivatives and lead to erroneous results. For this study, only fourth order smoothing was present in the CFD solution. The smoothing constant was halved for the $e = 1.5$ fine grid case to assess these effects. The only variations in the linear stability results were in the region near the edge of the boundary layer build-up near the top

centerline. A finer grid would be desirable here to resolve the higher flowfield gradients in this region.

Tests were conducted on the $e = 1.5$ configuration to determine the effects of linear stability approximations on stability predictions. Results should be qualitatively similar for the other configurations. Several parameters control the location of the outer boundary and the region the e^{Malik} internal grid is clustered to. Clustering of the e^{Malik} internal grid and the outer boundary location were varied, but no significant effects were observed. In the final results, the outer boundary location was set to 20 times the boundary layer height, and the clustering parameter was set to 80% of the boundary layer height.

The version of the e^{Malik} code used did not include the coordinate system curvature terms. The axial curvature of the coordinate system as it moves along a streamline should be small and of little consequence since there is no destabilizing concave curvature. The transverse curvature should be more like that seen on a conical body, however. Accordingly, the conical coordinate system curvature terms were introduced into the code to get some idea of their effect. These showed amplification reductions over many regions that averaged around 10%. This calculation is not rigorously correct, but it does give some idea of the uncertainty in the results. A PSE code could more easily include the curvature and non-local effects that the present linear stability analysis ignores.

Basic State Results

The pressure distributions about the circumference of the three configurations are shown in Fig. 6-2. The pressure gradients between the major and minor axes establish the crossflow, and the strength of the crossflow depends on the magnitude of these gradients. The crossflow is defined relative to the boundary layer edge velocity, with positive crossflow defined as inboard toward the model centerline. The boundary layer edge velocity is not, in general, parallel to a ray emanating from the model nose. At most locations the edge velocity possesses a component directed inboard due to the circumferential pressure gradient, and a component directed toward the model surface since the conical bow shock does not turn the streamlines completely parallel to the model surface. Thus a boundary layer edge velocity direction must be defined for each radial grid line. The total enthalpy profile was used to identify the boundary layer edge since it is unaffected by shock curvature and has been shown previously to correlate well with the velocity thickness for circular cones[41]. Since the Prandtl number is less than unity, the total enthalpy profile varies from less than freestream at the wall to a maximum 3% to 4% above freestream within the boundary layer. The boundary layer edge is taken as the location above the peak where the total enthalpy ratio is 1.005. At each circumferential station the boundary layer edge was identified and the edge total velocity vector noted. The cross product of the body normal with the edge velocity vector defined the crossflow direction for each radial grid line.

Contours of w_{max} / U_e for the $e = 2.0$ configuration are shown in Fig. 6-3. The crossflow contour shapes for the other two configurations were similar. The maximum boundary layer crossflows were 6.5%, 10%, and 14.5% for the $e = 1.5$, 2.0, and 4.0 configurations, respectively. The 10% maximum crossflow ratio for the $e = 2.0$ configuration compares to a peak of about 4% for the $e = 2.0$ configuration[38] at $M_\infty = 4.0$. The increased crossflow in the present study is due to the stronger circumferential pressure gradient created by the higher Mach number.

The crossflow is illustrated by the surface (or limiting) and boundary layer edge streamlines for the $e = 2.0$ configuration shown in Fig. 6-4. The edge streamlines are directed approximately along rays from the nose of the configuration, but the surface streamlines (computed from the first point off the body surface) are sharply deflected toward the centerline. The surface streamlines run parallel to but do not cross a locus near the centerline. This feature is typical of a crossflow separation, and was observed by Lyttle and Reed[38].

To further investigate the existence of crossflow separation, sectional streamlines in the crossflow plane are plotted in Fig. 6-5. These velocity vectors are described in a spherical coordinate system, in which a zero length vector represents either zero velocity magnitude or flow directed entirely along a

ray from the origin at the model nose. The vectors in Fig. 6-5 represent flow perpendicular to rays from the origin. Although sectional streamlines may in some cases be misleading[66], Fig. 6-5 provides strong evidence of crossflow separation. Cross flow separation is indicated by the liftup of sectional streamlines from the model surface near $\beta = 1.2$ deg. (coincident with the surface line of convergence), and the spiral focus located near $\beta = 0.8$ deg and $\alpha = 7.2$ deg. The vortex would be difficult to identify experimentally due to its close proximity to the model body.

The crossflow separation or near-separation has implications for boundary layer stability. The boundary layer thickness perpendicular to the model surface in Fig. 6-6 illustrates the ballooning of the boundary layer near the model centerline. These results are typical of the other two configurations. This ballooning is due to the influx of low momentum fluid from around the model circumference, and increases with increasing crossflow. A thick, decelerating boundary layer would be expected to be unstable, a conclusion which is born out by the velocity profiles in Fig. 6-7, and stability results described below. Velocity profiles near the leading edge and the model "shoulder" are full and typical of accelerated flows. The velocity profile at the model centerline is inflectional and typical of a decelerated flow.

Heat transfer for the $e = 2.0$ cold wall case is shown in Fig 6-8. Heat transfer is highest on the leading edge, due to the attachment line heating. The heat transfer decays exponentially with x, as observed by Burke[26] for the elliptic cone at Mach 10. The boundary layer build-up on the model centerline is reflected in the low heat transfer at $\theta = 0$ degrees.

Transition Correlation Results

Transition correlations based on mean flow parameters are notoriously uncertain but often are the only prediction tool available. Since the flow stability is related to factors such as Reynolds number and Mach number, transition correlations provide at least a gross indicator of whether a flow is near or far from transition. For these reasons, several transition criteria were examined for this study.

The conventional crossflow Reynolds number, Re_{cf}, is plotted in Fig. 6-9 for the $e = 2.0$ configuration. A typical value for crossflow transition in incompressible boundary layers is $Re_{cf} = 150$. The conventional crossflow Reynolds number over the bulk of the $e = 2.0$ configuration is about an order of magnitude larger than this. Reed and Haynes[37] suggest scaling the conventional crossflow Reynolds number to take into account the increase in boundary layer thickness which occurs as Mach increases. Their modified crossflow Reynolds number, $Re_{cf(new)}$, is defined as $HLRe_{cf}$. L is unity for an adiabatic wall, and H is defined as $\eta(\delta_{10}) / \int_0^{\eta(\delta_{10})} (T / T_e)d\eta$, where η is the computational coordinate perpendicular to the model wall. Since T/T_e is unity or greater over an adiabatic wall boundary layer, H is less than one, and as can be seen from Fig. 6-9, has the effect of scaling the conventional crossflow Reynolds number back into a range typical of incompressible boundary layers near transition.

Reed and Haynes[37] further suggest correlating compressible crossflow transition with the parameter R, defined as $R = Re_{cf(new)}U_e / w_{max}$, and present data over a range of $0.02 < w_{max} / U_e < 0.08$ indicating that transition occurs in conventional facilities at a value of $R = 33.7$. The loci of $R = 33.7$ locations for the three configurations are shown in Fig. 6-10. Although the $R = 33.7$ contours lie, for the most part, outside the range of $0.02 < w_{max} / U_e < 0.08$ for which the correlation was developed, they do indicate the presence of significant crossflow on each configuration. N-factor contours (discussed below) of 4 and 5 are also shown on these plots. Contours of $R = 33.7$ do not correlate with any particular N-factor.

Since velocity profiles on the model centerlines are inflectional and unstable, traveling-wave dominated transition might occur here. In order to assess centerline transition, contours of the correlating parameter Re_θ / M_e of 100 were plotted. In all cases, a value of Re_θ / M_e of 100 is attained on centerline at less than 20% of the body length, indicating the instability of this region.

The $Re_\theta / M_e = 100$ contours are nearly coincident with contours of $R = 33.7$. It might have been expected that their shapes would be similar. When the crossflow Reynolds number is multiplied by U_e / w_{max}, w_{max} cancels, leaving a Reynolds number based on δ_{10} and edge values of U and v, so all dependence on the crossflow velocity drops out.[37] H is a boundary layer integral parameter like θ, and θ, like H, can be expressed as an integral of temperature over the boundary layer through the thermodynamic and Crocco-Busemann relations.[67] The 10% crossflow thickness, δ_{10}, is equal to about 90% of δ over most of the elliptic cone. It remains to be seen, however, whether the contour shapes are similar or even coincident on other configurations.

Stability Results

Zero-frequency linear stability analysis was conducted on all configurations, and multiple frequency analysis was conducted for the $e = 1.5$ and 2.0 configurations. Zero-frequency wavelengths and wave angles are illustrated in Fig. 6-11. The wave angles are inclined approximately 90 deg to the boundary layer edge velocity vectors, i.e., the vortices are approximately aligned with the boundary layer edge streamlines. The zero-frequency wavelengths tend to be between two and three boundary layer thicknesses, and can thus be pictured as being somewhat flattened. The $e = 2.0$ results are typical of the other two configurations.

Since the N-factor method is a correlation method, transition prediction requires that a correlating N-factor be chosen. Previous computations[7] indicated that a correlating N-factor for second-mode-dominated transition for a 7 deg half angle sharp cone in AEDC tunnel B is between four and five. Experimental studies by King[31] in the NASA Langley Mach 3.5 quiet tunnel indicated that the effect of wind tunnel "noise" on putatively crossflow-dominated transition was much less than the effect of noise on traveling-wave-dominated transition. This effect might be due to the fact that the wind tunnel noise field consists primarily of convecting acoustic waves, and stationary crossflow vortices have a phase velocity of zero. The stationary disturbances might be expected to be more sensitive to zero-frequency disturbances, i.e. perturbations in the mean flow due to model roughness or wind tunnel flow non-uniformity. These results imply that N-factors for zero-frequency disturbances in AEDC tunnel B might be higher than four or five. Without further prior knowledge, an N-factor for crossflow transition in this facility cannot be determined. Therefore, an N-factor of five was chosen as a benchmark value indicating significant disturbance growth.

Fig. 6-10 shows $N = 5$ contours for zero-frequency disturbances. Since the maximum N-factor on the $e = 1.5$ configuration is less than five, the $N = 4$ contour is shown instead. The N-factor contour shapes correspond to the crossflow contours in Fig. 6-3, indicating that for these configurations, percentage crossflow is a gross indicator of crossflow instability. The integrating effect of the N-factor procedure causes the peak N-factor contours to be shifted inboard slightly relative to the maximum crossflow contours

Since the top centerline of the model was expected to be unstable to traveling disturbances, instabilities with frequencies of 20, 40, 60, 80, 100, 130, and 160 kHz were also calculated for the $e = 1.5$ and 2.0 configurations. Figure 6-12 shows that a large portion of the $e = 2.0$ cone (typical) is unstable over a broad range of frequencies. This contrasts with the axisymmetric cone case,[7,41] which shows a well-defined first and second-mode merged instability region with damped disturbances outside of this range. The 3-D instability behavior is reminiscent of the results of Stetson[30] on the leeward centerline of a 7 deg. sharp cone at 2 deg. angle of attack, which exhibited broad-band instability.

N-factors were calculated for each of the above frequencies, integrating along both the streamline and group velocity directions. The differences between streamline and group velocity integration were negligible. Contours of 40 and 60 kHz, which attained N-factors of five earliest, are shown in Fig. 6-13. These contours show a double-lobed appearance, in contrast to the single-lobed contours for zero frequence disturbances seen in Fig. 6-10. The outboard lobe is associated with the region of maximum crossflow, and the inboard lobe is associated with the unstable profile near the model centerline.

The $e = 4.0$ configuration was eliminated as a test configuration since an N-factor of five for zero-frequency disturbances occurred at about 30% of the body length, indicating possible early transition, leaving little room for probing the boundary layer prior to transition. Also, the boundary layer build-up on the model centerline was larger than the other two configurations, indicating a possible early transition on the centerline which might contaminate the off-centerline transition process.

The $e = 1.5$ and 2.0 configurations were unstable to a broad band of traveling disturbances. These configurations displayed traveling-wave N-factors of five early on the model centerline. In the crossflow region, traveling-wave N-factors of five occurred at 40-50% of the model length. Given that N-factors of stationary and traveling waves are roughly equivalent, the transition process is likely to be mixed-mode, with contributions from both traveling and crossflow instabilities. It may be necessary in the experiment to place roughness on the model surface in order to force standing wave dominance. The $e = 2.0$ configuration was chosen for fabrication since it showed higher crossflow N-factors than the $e = 1.5$ configuration.

The build-up and instability of the centerline boundary layer is a problem which must be dealt with in any flight configuration which exhibits inboard-directed crossflow. It is possible that the body might be contoured in some way to alleviate this build-up and stabilize the boundary layer. Future research should also consider the blunt-nose elliptic cone configuration. This configuration offers a more complex but more realistic flight geometry. Also, bluntness can stabilize second mode instabilities on axisymmetric cones.[68] If traveling waves could be sufficiently stabilized, the crossflow instability might be isolated.
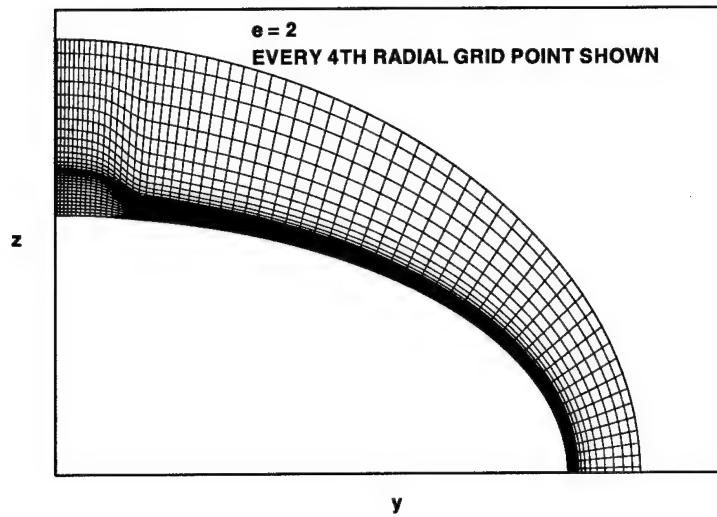
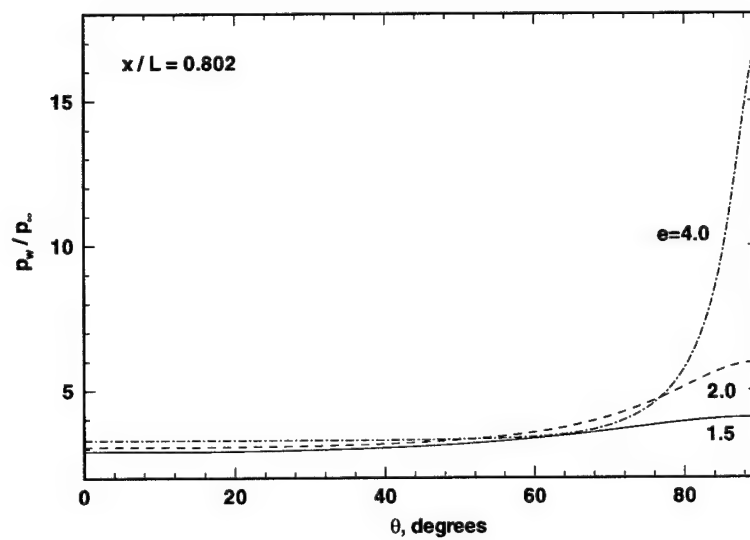Figure 6-1. PNS computational mesh on *e* = 2.0 elliptic cone.

Figure 6-2. Circumferential distribution of wall-to-freestream static pressure ratios.
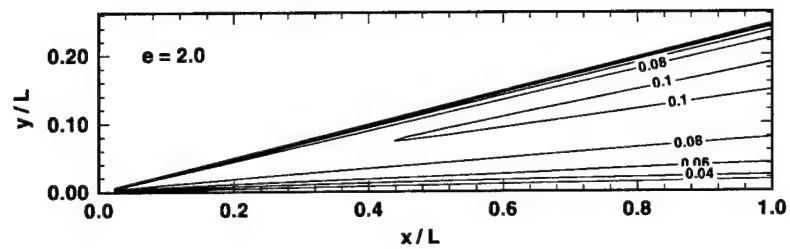
Figure 6-3. Top view of crossflow velocity contours for $e = 2.0$ elliptic cone.
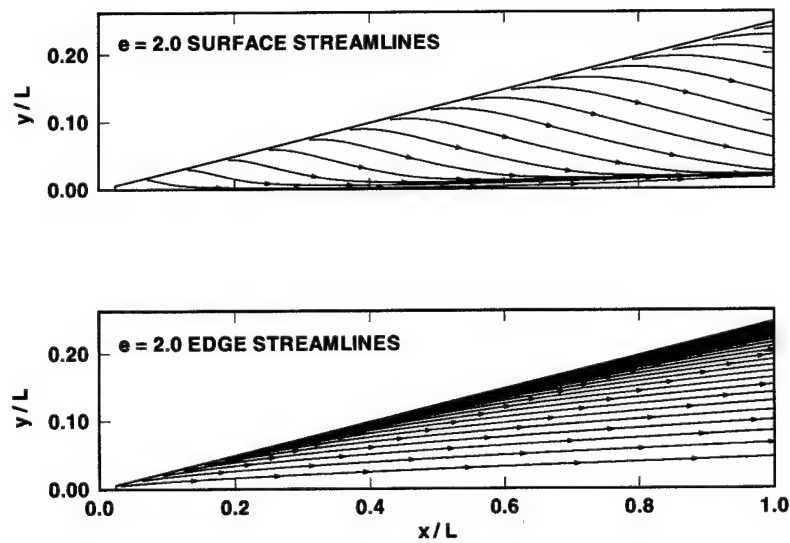

Figure 6-4. Top view of surface and boundary layer edge streamlines for the $e = 2.0$ configuration.
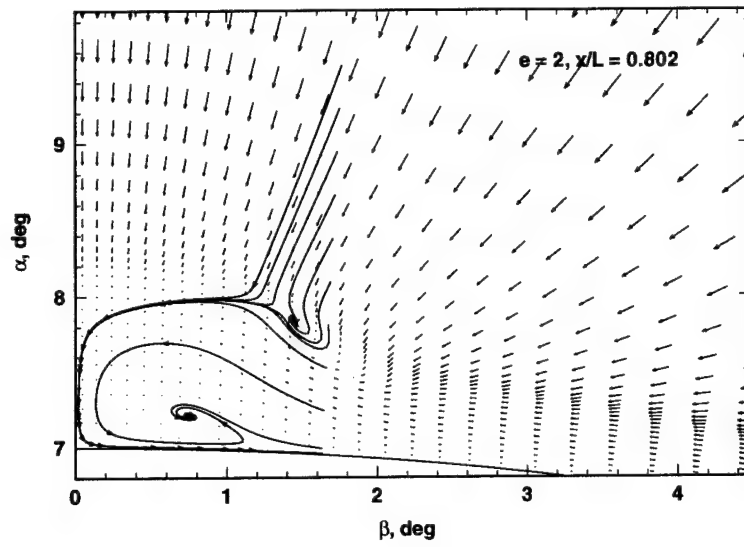
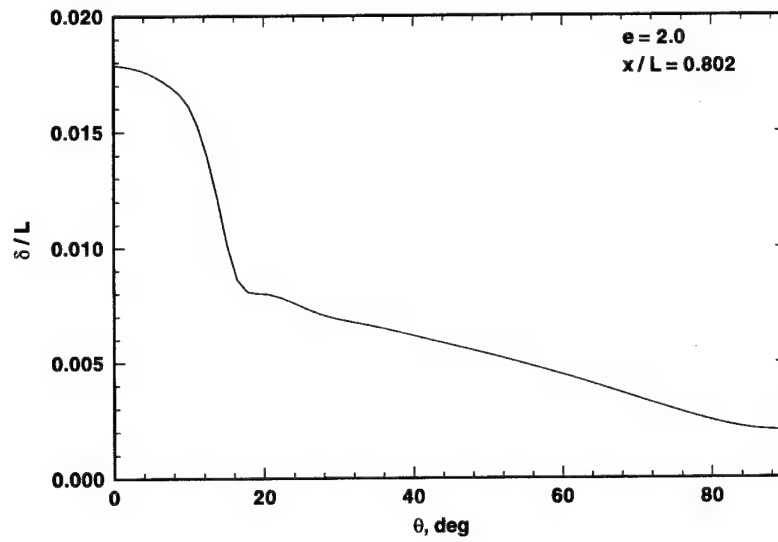Figure 6-5. Sectional streamlines in spherical coordinate system. Every 4th radial point shown.
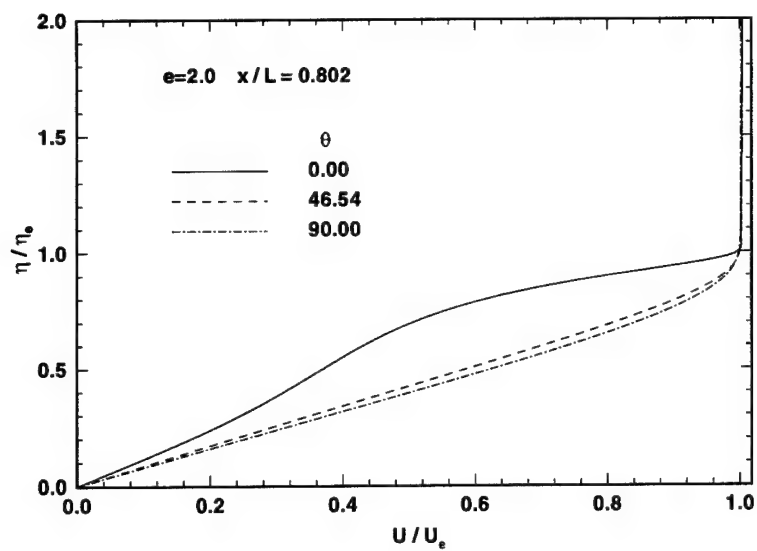

Figure 6-6. Boundary layer thickness for the $e = 2.0$ configuration.

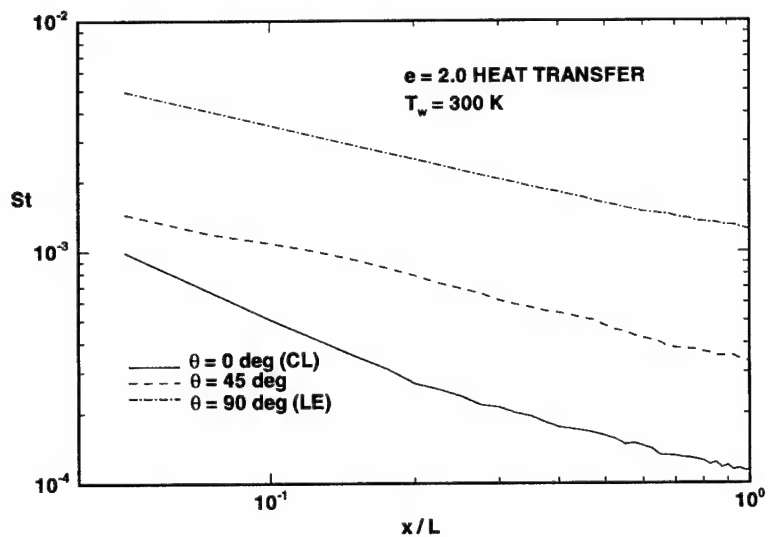Figure 6-7. U-velocity profiles for the $e = 2.0$ configuration.

Figure 6-8. Computed heat transfer for the $e = 2.0$ configuration, $T_w / T_0 = 0.42$.
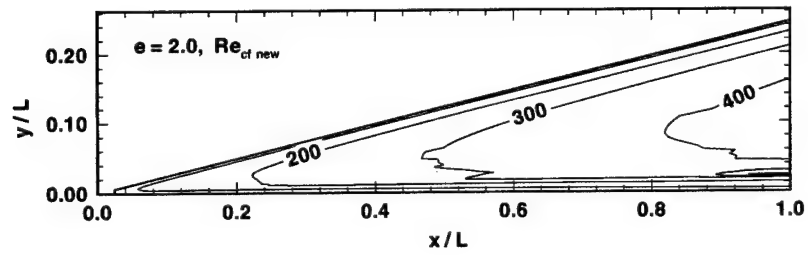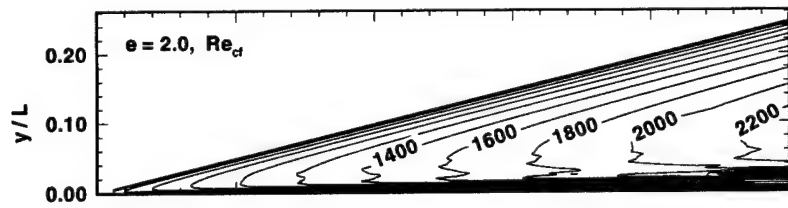
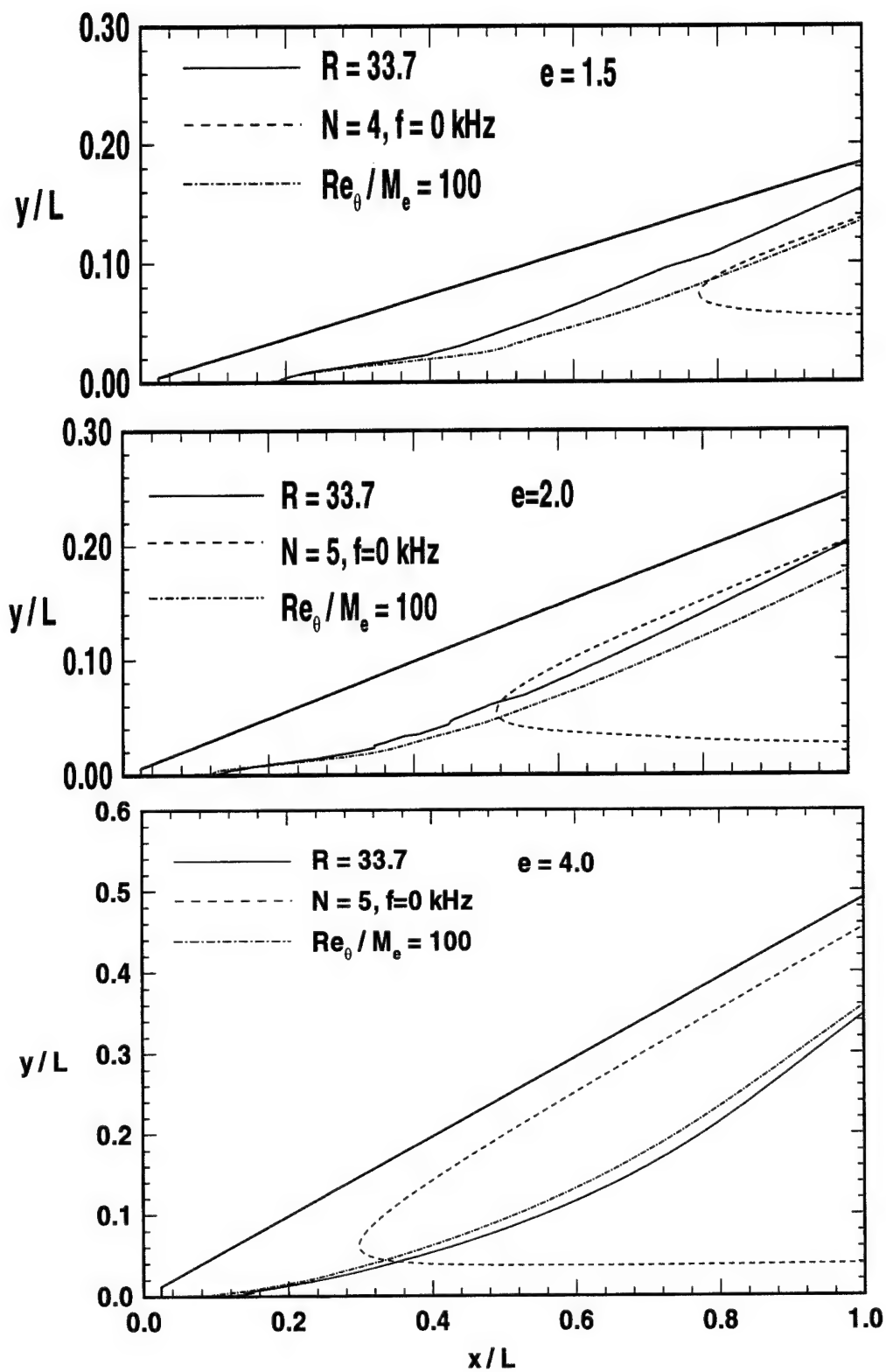Figure 6-9. Crossflow Reynolds number contours for the $e = 2.0$ configuration.
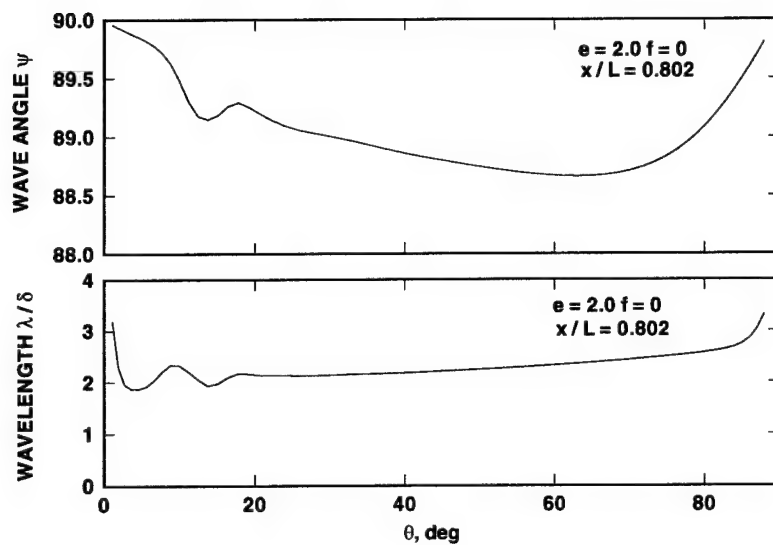
Figure 6-10. Transition correlations.

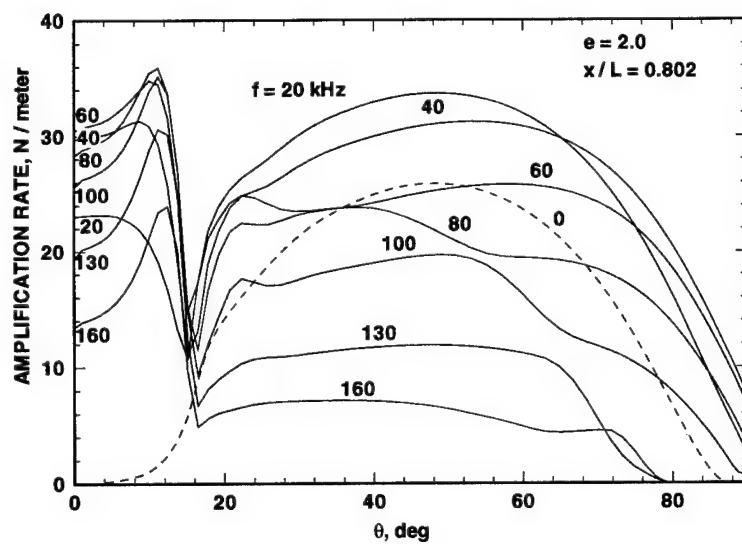Figure 6-11. Zero-frequency wave angles and wavelengths for the *e* =2.0 configuration.

Figure 6-12. Amplification rates around the circumference of the *e* = 2.0 configuration.
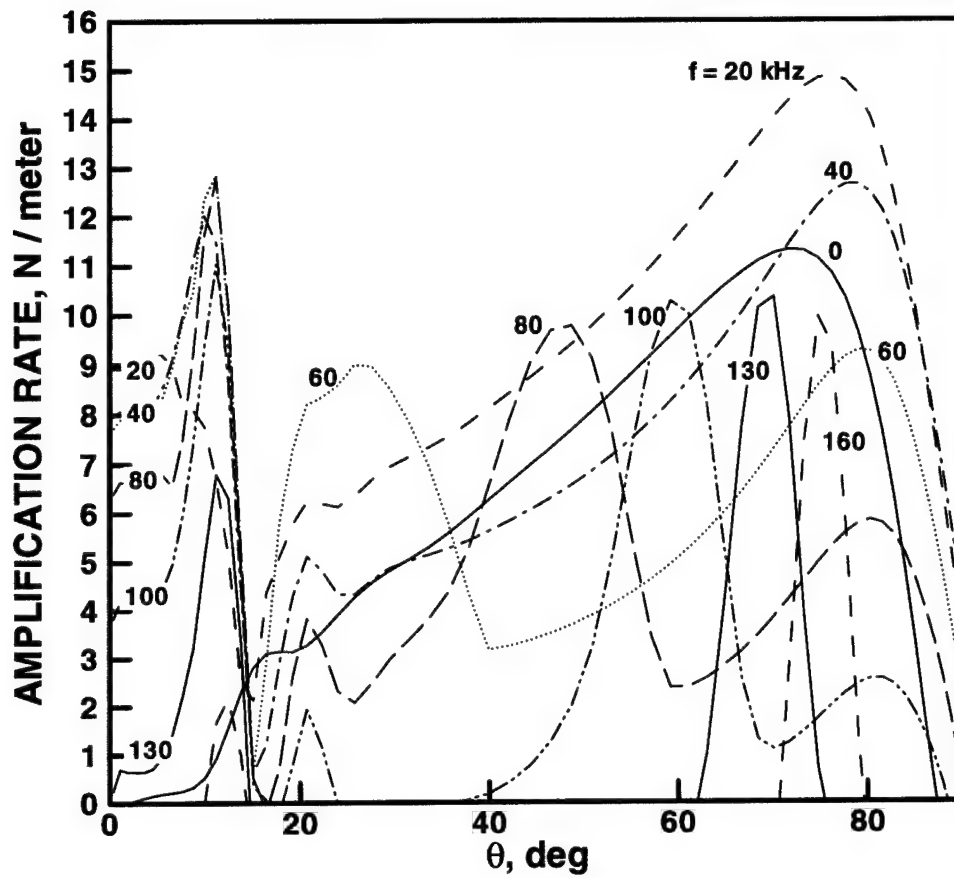
Figure 6-13. $N = 5$ contours for 40 and 60 kHz traveling waves.

7.   ELLIPTIC CONE MEASUREMENTS

Measured surface pressures are compared to computed pressures in Fig. 7-1. Computations were carried out at $Re_L = 3.3\text{x}10^6$. Measurements were obtained at $Re_L = 6.7\text{x}10^6$ for optimum transducer resolution. Measured pressures agree with computation to within approximately 5%. Leading edge and centerline measured pressures are somewhat lower than computed, probably due to the reduced viscous interaction at the higher Reynolds number. Viscous interaction, as evidenced by the length it takes for pressure to relax to a constant value along a ray, is more pronounced on the model centerline than the leading edge due to the thick centerline boundary layer.

Schlieren photographs taken with the model at 0 deg roll (minor axis up, Fig. 7-2) show boundary layer breakdown beginning at $x / L \approx 0.5$. A portion of the model from approximately $x / L \approx 0.1$ to $x / L \approx 0.5$ is visible in this window. At the top of the model on the right, structures resembling rope waves with wavelengths approximately 2-3δ are visible preceding breakdown. Schlieren images taken at $Re_L = 6.7\text{x}10^6$ (not shown) showed distinct rope waves in the leading edge boundary layer. Traveling waves are thus evident on both major and minor axes.

In both the top and bottom boundary layer, unusual structures consisting of elongated streaks, inclined approximately 5 deg to the model surface, are visible. These structures appear in every schlieren photograph at this roll angle, and at other roll angles up to about 26.1 deg. They are perhaps cores of crossflow vortices, projections of highly skewed rope waves, skewed compression waves produced by the local increase in displacement thickness near the centerline, or some other phenomenon. Their inclination is greater than the centerline Mach wave inclination, and they appear on both the clean (top) and instrumented (bottom) sides of the model, so their source is not surface instrumentation roughness. Because the boundary layer balloons up locally on the centerline, two boundary layer edges project above the model silhouette when the model is inclined at a small roll angle. One edge is due to the centerline boundary layer, and the other is due to the thinner boundary layer off of centerline. Judging from its thickness, the boundary layer edge visible in Fig. 7-2 is the centerline boundary layer. The dark streaks observed on the schlieren do not appear to be the edge of the peripheral boundary layer, since this runs approximately parallel to the model centerline, rather than at an angle to it, like the streaks in the photograph do.

An example of surface oil streak flow visualization is shown in Fig. 7-3. The model was rolled 90 deg (major axis up), and was photographed through a side window. Oil was applied at four locations on the model leading edge at the top and allowed to drip from top to bottom, forming four starting lines approximately perpendicular to the airflow. Two indications of transition appear in the oil flow. First (best observed in the set of streaks nearest the model trailing edge), oil near the centerline has been dragged farther downstream than oil near the leading edge, indicating higher shear due to turbulent flow in this region. Second, oil streaks in this region appear to be aligned roughly with rays emanating from the model apex. This is contrasted with (for example), the second set of streaks downstream of the model apex, which show large angles near the centerline and are more similar to the computed laminar surface streamlines (shown in the previous section). Higher wall shear within the turbulent boundary layer causes reduced crossflow, and would be expected to produce streaks more closely aligned with the edge streamlines, as is observed here. Also, the linear stability calculations for this model showed that crossflow vortices should also be approximately parallel to edge streamlines. However, based on the heat transfer data (shown later), the region with oil streaks parallel to edge streamlines lies beneath turbulent flow. It seems unlikely that crossflow vortices would survive intact this far into the turbulent region. Also, the streak spacing is less than the expected crossflow wavelength.

Crossflow separation is not evident in the oil flow within the turbulent region. However, within the region of laminar flow, two long streaks of oil appear near centerline in the streak pattern second from the nose tip. Any crossflow separation would be expected to be very close to centerline, and the resolution of the oil streaks here precludes the visualization of any well-defined coalescence lines. However, the parallel lines of oil accumulation in this region may well signify crossflow or incipient crossflow separation.

Fig. 7-4 shows heat transfer from the leading edge at the highest and lowest Reynolds numbers, $Re_L = 6.7 \times 10^6$ and $Re_L = 1.7 \times 10^6$. Transition occurs at a Reynolds number of $Re = 4.9 \times 10^6$, as evidenced by the rise in heat transfer above computed laminar values. The relative stability of the leading edge is demonstrated by comparing heat transfer here to heat transfer on the model centerline at the lowest Reynolds number, shown in Fig. 7-5. Transition occurs here at $Re_x = 0.5 \times 10^6$. For comparison, transition on a cold wall, sharp-nosed axisymmetric cone of 7 deg. half angle in AEDC Tunnel B[69] at Mach 8 is $Re = 2.7 \times 10^6$. Flowfield computations show a thick centerline boundary layer with strongly inflected velocity profiles on the elliptic cone. As evidenced by the heat transfer measurements, this boundary layer is highly unstable. Leading edge transition is typically more of a design consideration than leeside or centerline transition due to the high heating here. However, since the centerline transition occurs so far forward and covers such a large region of the model, its effects are not insignificant.

Fig 7-6, which illustrates roughness effects, shows heat transfer at $x / L = 0.65$ around a 90 deg. quadrant of the model for $Re_L = 1.7 \times 10^6$. Increased heat transfer occurs between $\theta = 20$ and 70 deg. when 2 mm and 1.3 mm diameter roughness is placed around the circumference of the model at $x / L = 0.225$. A weak circumferential periodicity in the heat transfer near $\theta = 45$ deg on the smooth model amplifies with increasing roughness. The crossflow wavelength here is expected to be approximately 13.7 mm, or approximately 6.2 deg. of arc at $\theta = 45$ deg. and $x / L = 0.65$. Spacing on center for the 2 mm and 1.3 mm diameter roughnesses was 7.9 mm (2.2 deg.) and 5.2 mm (1.8 deg.), respectively. The five heat transfer gauges between $\theta = 38$ deg. and 52 deg. are spaced at 3.5 deg intervals. Heat transfer from these transducers shows a circumferential periodicity of about 7 deg. Although the circumferential transducer spacing is near or slightly greater than the expected Nyquist wavenumber for crossflow instabilities, the fact that the heat transfer pattern persists and amplifies with increasing roughness (regardless of the circumferential spacing of the roughness) is strongly suggestive of a stationary crossflow vortex signature. Also, Fig 7-6 shows that roughness placed along the leading edge has essentially no effect on heat transfer at this station. Linear stability calculations indicate that stationary cross flow vortices will have their axes aligned with the boundary layer edge streamlines. These results indicate that disturbances engendered by the roughness elements propagated along the same directions as the crossflow vortices, rather than the surface streamlines.

Heat transfer contours are shown in Fig. 7-7. These contours were constructed with data obtained at each of the unit Reynolds numbers tested. The locations of the individual transducers in Re_x, θ coordinates used to construct the contours are superimposed. Discontinuities in heat transfer at $Re_x = 10^6$ and 4.8×10^6 are artifacts due to interpolation between the grid of circumferentially arrayed transducers and transducers located along rays of the model. The measured heat transfer was divided by the calculated laminar heat transfer to obtain a ratio, h, which was near unity for laminar flow, and greater than unity for turbulent flow. Since the computations underpredicted heat transfer somewhat, a threshold value of $h = 1.5$ was chosen to indicate transition. A third order, least squares polynomial was fitted through the transition front obtained in this fashion. This transition front coincides with the first departure of heat transfer values away from their local minima. A unit Reynolds number effect was observed in the data, i.e., the transition Reynolds number Re_x varies with freestream unit Reynolds number. This variation was up to 20% at $\theta = 45$ deg.

Data presented in Re_x, θ coordinates suffer from a greatly exaggerated scale near the nose. The data of Fig. 7-7 are presented in Fig 7-8 on the developed, or unwrapped, surface of the cone. It can be seen from this figure that the high heat transfer on the leading edge and near the centerline are confined to relatively small areas. Local peak heating due to transition near the shoulder is distributed over a wider area.

The transition front extracted from Fig. 7-7 is compared in Fig. 7-9 to computed cold wall Re_θ / M_e contours. As pointed out by Stetson[70], Re_θ / M_e is a less than desirable correlation parameter due to the uncertainty in correlating Re_θ / M_e values, which produces large uncertainty in transition location. Nevertheless, it is still widely used due to its simplicity and the fact that it embodies at least rough transition trends in Reynolds number and Mach. Comparison of the measured transition front to Re_θ / M_e contours shows that transition corresponds to Re_θ / M_e of approximately 100. As shown previously, this value of Re_θ / M_e coincides approximately with the Reed and Haynes[37] correlating parameter of $R = 33.7$ on the adiabatic wall elliptic cone.

Since transition occurs first at the model centerline, due to the unstable boundary layer here, it must be questioned how much of the transition front around the circumference of the model is influenced by this early centerline transition. Certainly, some circumferential spreading is to be expected. However, given the centerline edge Mach number of approximately 6.8 and the fact that most of the flow is directed axially or toward centerline, circumferential contamination should be minimal. Wind tunnel experiments[71] on the windward side of the Space Shuttle Orbiter indicate that transition due to roughness placed to one side of an attachment line was contained to that side of the attachment line.

Hot Film Measurements

Spectra for six roll locations are plotted in Fig. 7-10. These stations show the most dramatic trends in stability. For $\theta > 55$ deg., the boundary layer shows only a low frequency component centered at less than 20 kHz. For $\theta < 25$ deg., the boundary layer spectrum appears turbulent, with a build-up in amplitude to approximately 100 kHz, followed by a roll-off. The nature of the spectra change markedly between $\theta = 25$ and 58 deg. The low frequency component disappears abruptly between $\theta = 45$ and 55 deg. Between $\theta = 55$ and 58 deg., a spectral component centered at approximately 70-90 kHz appears. Between $\theta = 45$ and 55 deg., this component increases in amplitude relative to the rest of the spectrum and shifts to lower frequencies. As θ decreases, this feature becomes less prominent relative to the rest of the spectrum, and is no longer evident at $\theta = 25$ deg. This non-dimensional frequency of this feature is approximately $0.5U_e/\delta$. It has been shown previously[3] that $0.5U_e/\delta$ is the characteristic frequency of second mode disturbances in axisymmetric boundary layers.

The nature of the lower frequency peak in the power spectrum is more difficult to determine. Low frequency peaks measured in a crossflow may be due to traveling crossflow vortices. However, low frequency peaks in the power spectrum have also been measured with hot wires on axisymmetric cone boundary layers in AEDC VKF-B[3] at freestream Mach 6 and 8, and in a NASA Langley quiet tunnel[5] at Mach 6. The shape of these low-frequency peaks appears similar to the freestream acoustic disturbance spectrum.[40] Measurements made in the axisymmetric cone boundary layer in AEDC VKF-B, using the same hot film probes used in this test also showed a low frequency peak. In contrast to the hot wire measurements, the hot film low-frequency peak was much less pronounced compared to the rest of the spectrum. This difference between the two sensors is most likely due to the over-compensation of high frequencies measured with the hot films. The low frequency peaks measured on the elliptic cone appear more prominent than those measured on the axisymmetric cone. Also, the prominence of the low frequency peak on the elliptic cone depends on the circumferential location. Based on these observations, the low frequency peaks may be associated with crossflow. Both the low and high frequency peaks show a good degree of circumferential coherence (Fig. 7-11).

These conclusions are further supported by comparing the measurements with linear stability computations. Computed amplification rates for eight selected frequencies at $Re = 1.6 \times 10^6$ are shown in Fig. 7-12. Only positive growth rates (negative α_i) are shown. High rates near the model centerline for $\theta < 16$ deg. are associated with the unstable, highly inflected mean velocity profiles there, and give rise to the early centerline transition observed in the experiment. For $16 < \theta < 90$ deg., two regions of high amplification are observed. One occurs near the model leading edge for

$72 < \theta < 84$ deg., and appears to be associated with crossflow. Peak amplification occurs at about 15 kHz. A second amplification peak occurs between approximately 20 and 80 deg. The location of this peak varies with each frequency and depends on the local boundary layer thickness.

Computed N-factors for the same Reynolds number are plotted in Fig. 7-13. The N-factors were computed by integrating α_i for the most unstable wave angle along the group velocity vector for each frequency. The group velocity vector was generally within 2 deg. of the edge streamlines, which in turn were similar to rays emanating from the model apex. To a rough approximation, the N-factors in Fig. 7-13 may be thought of as being integrated along rays from the apex. Integration was not carried out when growth rates became negative (α_i greater than 0). The plotted N-factors will thus be larger than actual in regions where these frequencies have crossed the upper neutral bound and begun to decay. The most-amplified frequencies over a large portion of the circumference are 15-30 kHz. This is in general agreement with the experiment. Away from the centerline, N-factors for traveling waves generally decrease monotonically with increasing frequency. No dramatic peak appears in the N-factor curves as it does in the experiment, indicating that the amplification of the higher frequencies may be underpredicted by linear theory.

For stations where the flow is laminar and unstable and distinct maxima can be identified in the cross-spectra, the frequencies corresponding to these peaks are plotted in Fig.

Cross-spectra from the three hot-film probes (LAT, US, and DS) were used to estimate disturbance wave angle.[72] Keeping in mind that the phase velocity (the speed of a constant-phase surface normal to itself) does not obey the ordinary rules of vector addition, the following geometric relationship holds for a quasi-planar wave intercepted by a pair of point probes lying in the x-y plane:

$$c_r \tau = \xi_x \sin \psi + \xi_y \cos \psi$$

The probe separations, ξ_x and ξ_y, are known for each pair of probes, and τ is obtained from the cross spectrum as demonstrated in Section 3. For any set of two pairs of probes a pair of simultaneous equations may be solved to obtain c_r and ψ. With the two probe pairs labeled 1 and 2, the equation for the wave angle is

$$\psi = \arctan\left[\frac{\tau_2 \xi_{y1} - \tau_1 \xi_{y2}}{\tau_1 \xi_{x2} - \tau_2 \xi_{x1}} \right]$$

and the phase speed is given by

$$c_r = \left(\xi_{x1} \sin \psi + \xi_{y1} \cos \psi \right) / \tau_1$$

Conclusions

The earliest transition occurred on model centerline due to the highly inflected, unstable boundary layer profiles here. The most downstream transition occurred on the leading edge. Traveling waves were evident on both leading edge and centerline in schlieren photographs. The transition pattern was correlated roughly with Re_θ / M_e contours of 100. Signatures of stationary crossflow vortices in surface oil flow or heat transfer were weak to nonexistent. This may be due to the attenuation of crossflow vortex eigenfunctions near the wall, unsteadiness in crossflow vortices, or simply their weakness or nonexistence. Roughness

placed along the model leading edge had little effect on heat transfer, but circumferentially spaced roughness caused increased, circumferentially periodic heating downstream. These results indicate that disturbances from surface roughness propagated along streamlines external to the boundary layer, rather than along surface streamlines. The circumferential variation in heat transfer thus appears to be due to crossflow vortices.

The salient feature of transition on the elliptic cone is the early centerline transition, which appears to be the result of traveling waves. Off-centerline transition appears to be affected by traveling waves also to some extent. These results are reminiscent of those obtained[22] on a delta wing at Mach 3.5. Stationary waves on this configuration were also weakly manifested except in the presence of roughness, and traveling waves appeared to be dominant, based on comparison of transition results with linear stability theory calculations. Two peaks were observed in the spectrum. The lower frequency peak appears to be due to traveling crossflow instability. The higher frequency peak is probably due to second mode instability. These observations are based on comparison of the experimental results to computed linear stability characteristics. Linear stability theory appears to underpredict the second mode amplification.

Two ramifications for transition prediction arise from this experiment. First, the demonstrated dominance of traveling waves in crossflows highlights the accuracy with which they must be calculated for transition prediction. Also, their relative influence compared to stationary waves must be accurately predicted. Second, leeside flow or influx due to crossflow at symmetry planes must also be accurately predicted, both in mean flow and stability analysis. Although heating rates here are generally lower than windward or leading edge locations, these flows are highly unstable, and transition here can spread laterally. This lateral contamination must also be calculated for three-dimensional transition fronts.
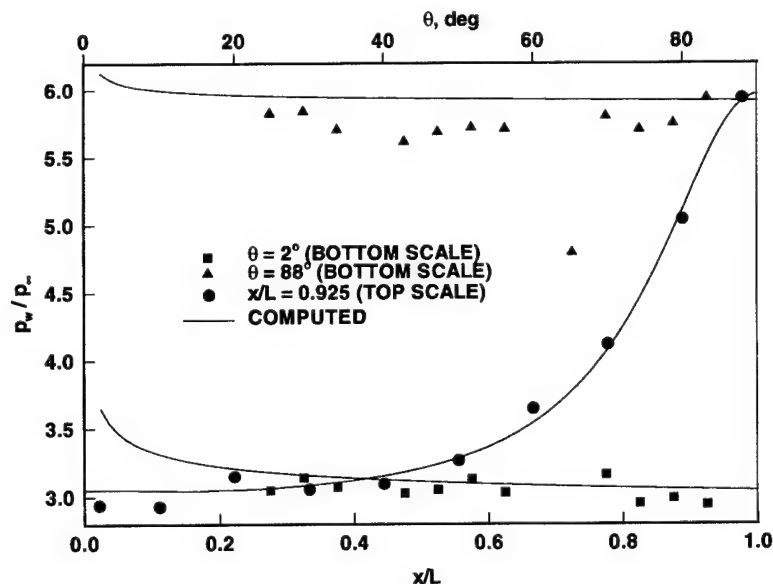

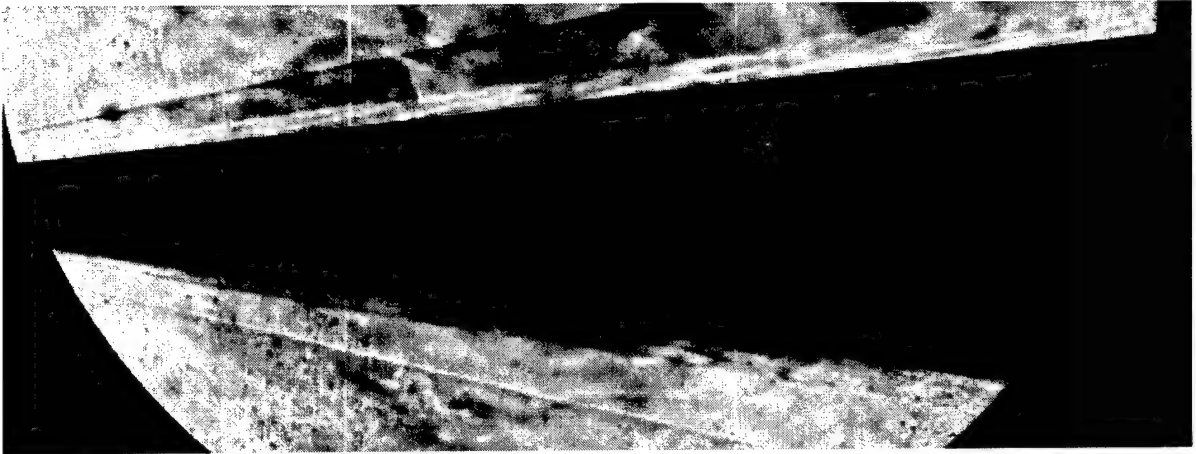Figure 7-1. Surface static pressures.

Figure 7-2. Schlieren.

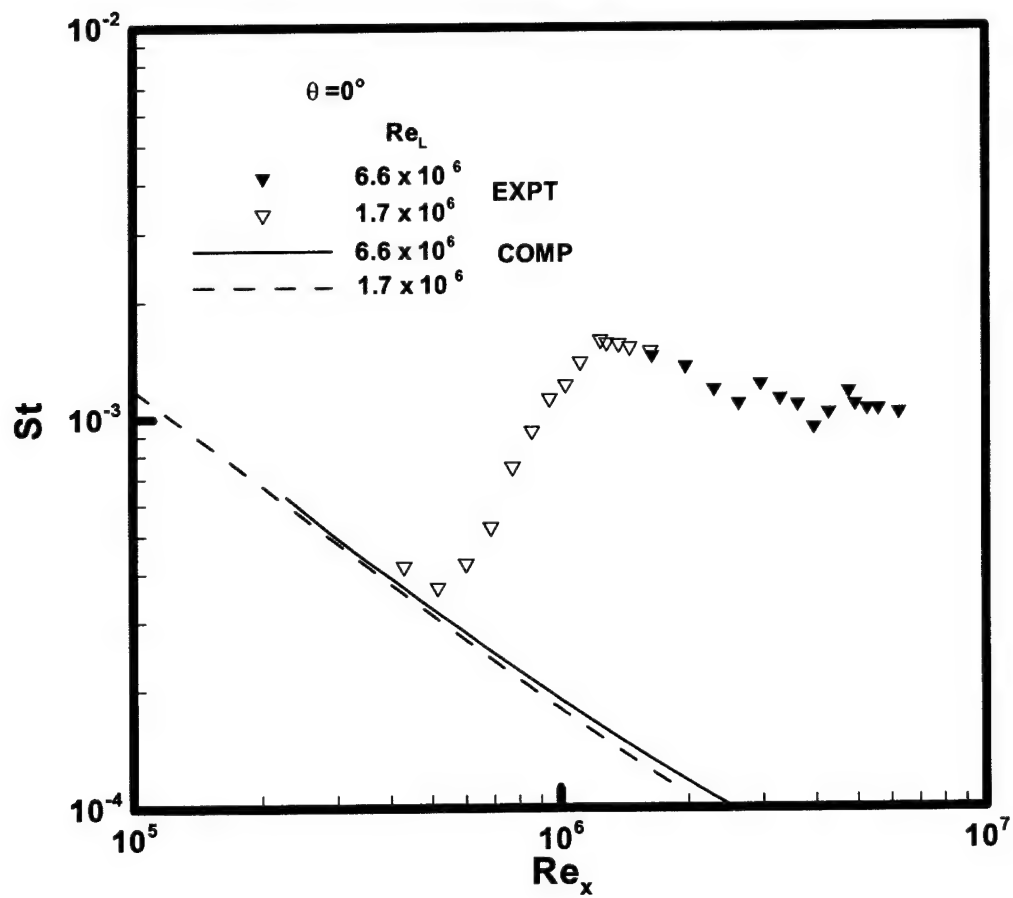Figure 7-3. Surface oil flow visualization.

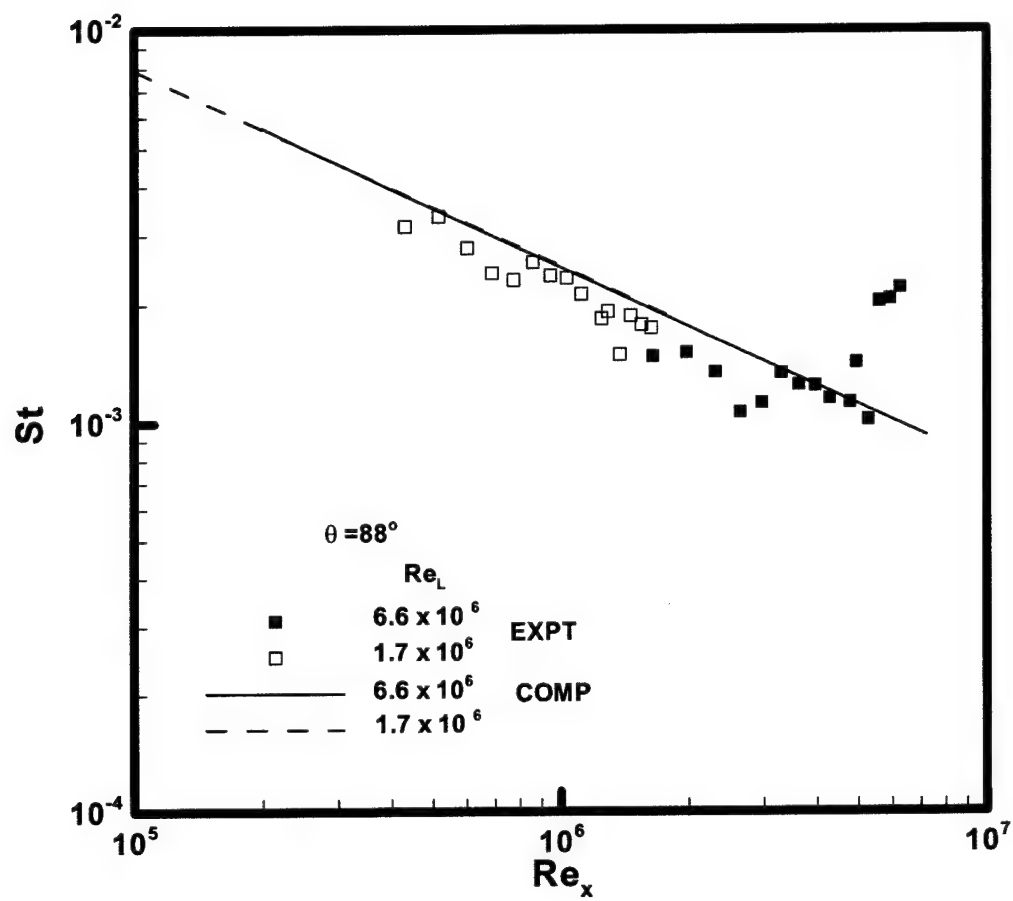Figure 7-4. Heat transfer on elliptic cone leading edge.

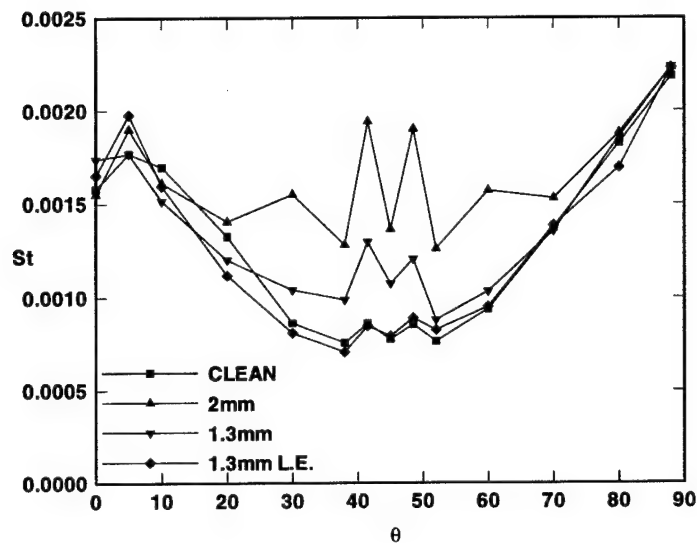Figure 7-5. Heat transfer on elliptic cone centerline.

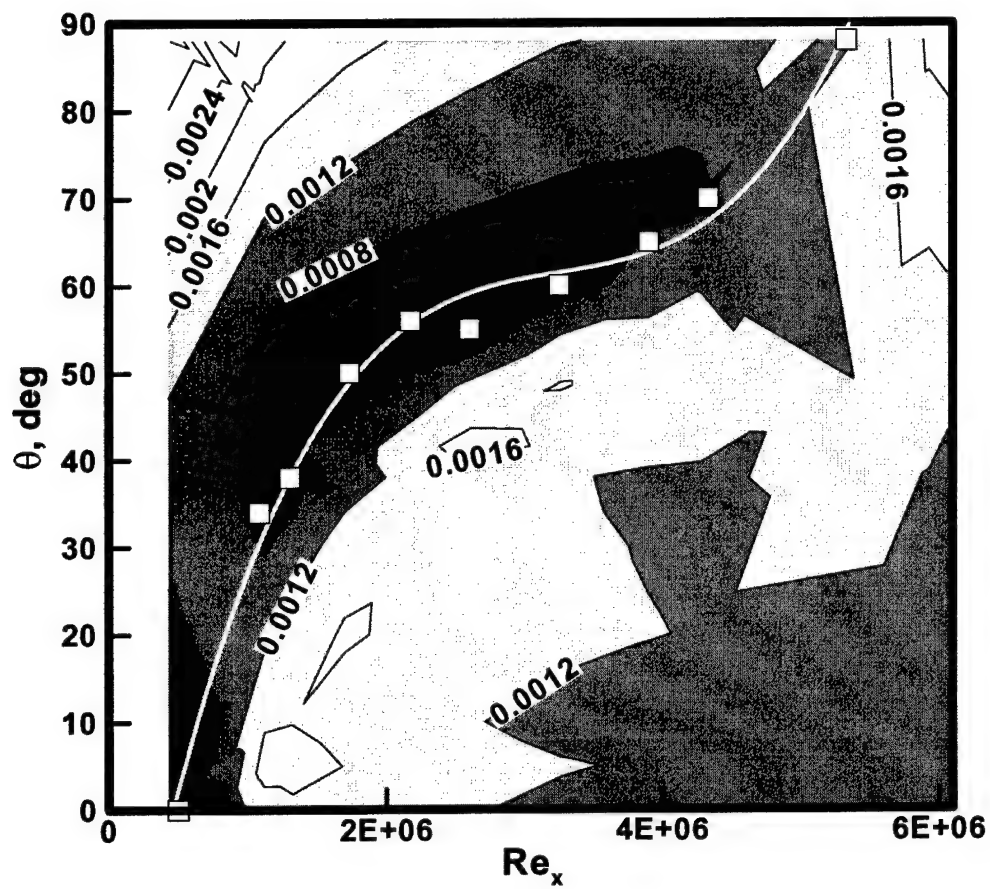Figure 7-6. Roughness effects on transition at $x/L = 0.65$ and $Re_L = 1.7 \times 10^6$.

Figure 7-7. Heat transfer contours. Symbols represent measured transition locations obtained using threshold value of $h = 1.5$. Solid line is curvefit through measured transition locations.
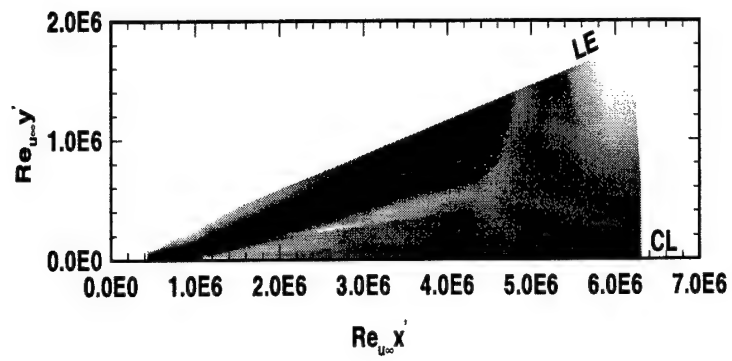
Figure 7-8. Heat transfer contours on developed cone surface.
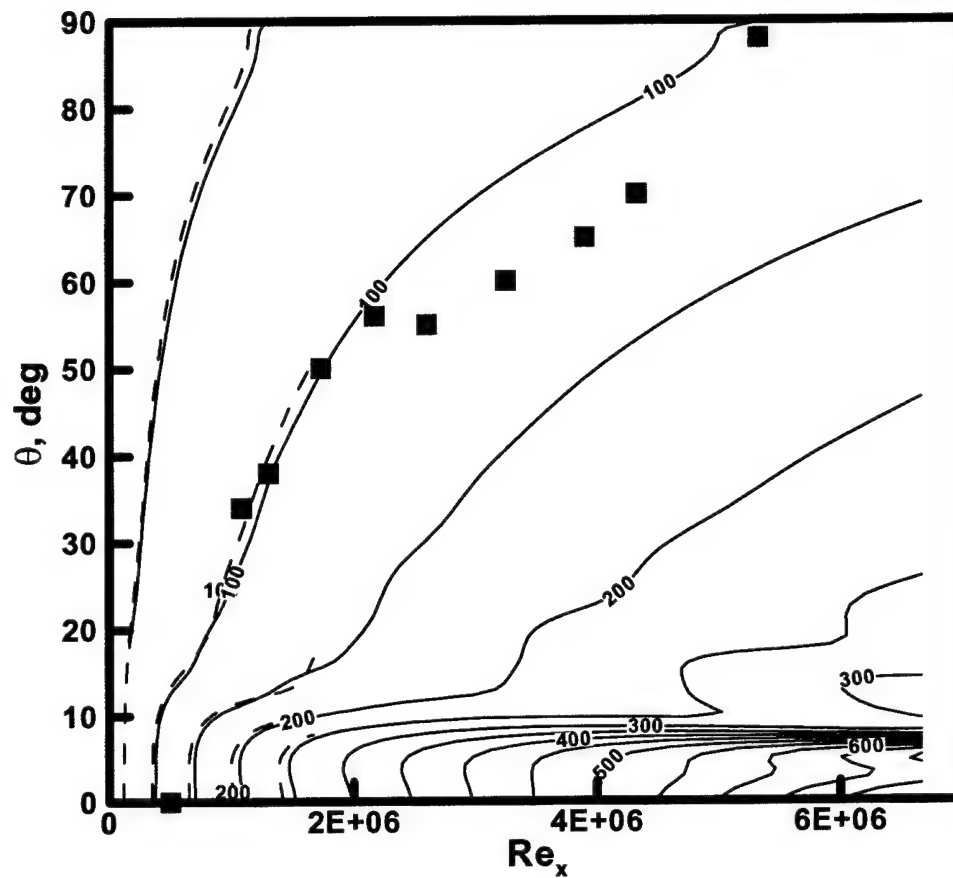
Figure 7-9. Measured transition front and computed Re_θ / M_e contours. Symbols indicate transition location derived from $h = 1.5$ threshold. Dashed lines are computed values of Re_θ / M_e for $Re_L = 1.7\text{x}10^6$, solid lines are computations for $Re_L = 6.6\text{x}10^6$.
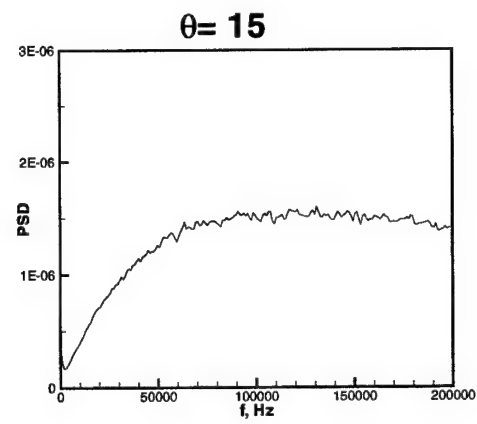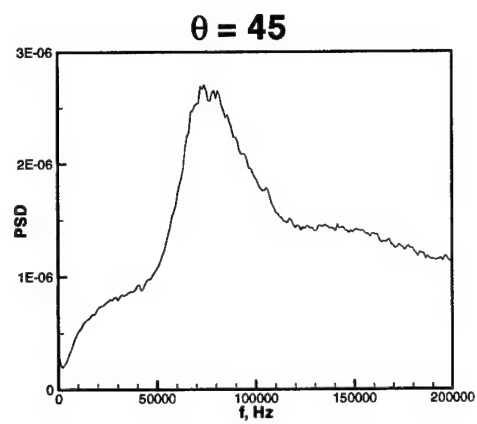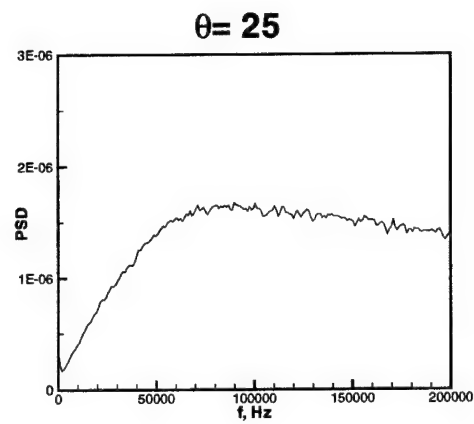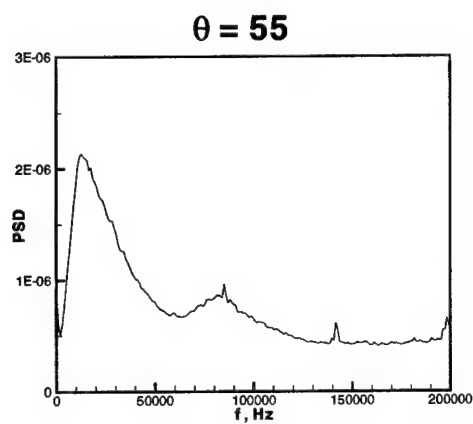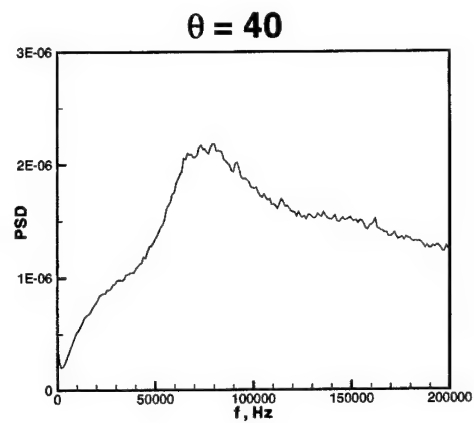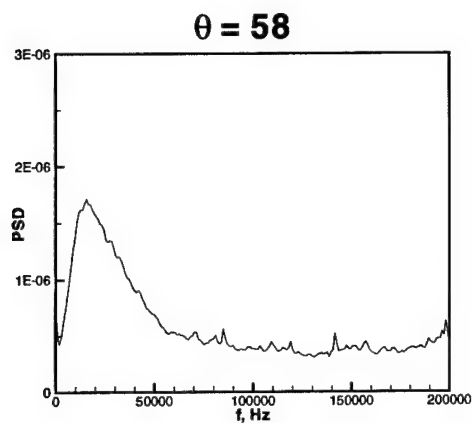
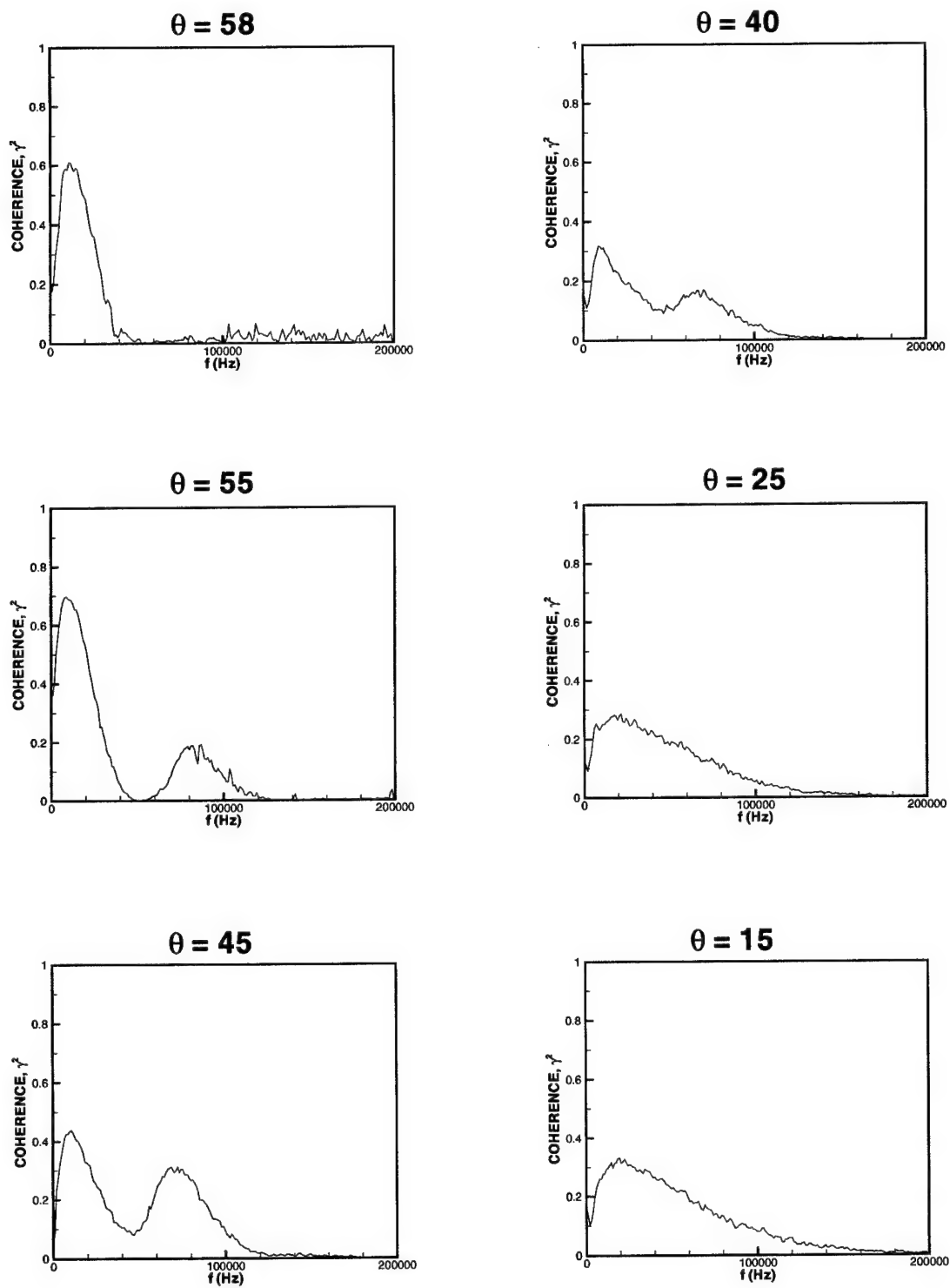Figure 7-10. Power spectra at $x/L = 0.8$, $Re = 1.6 \times 10^6$.

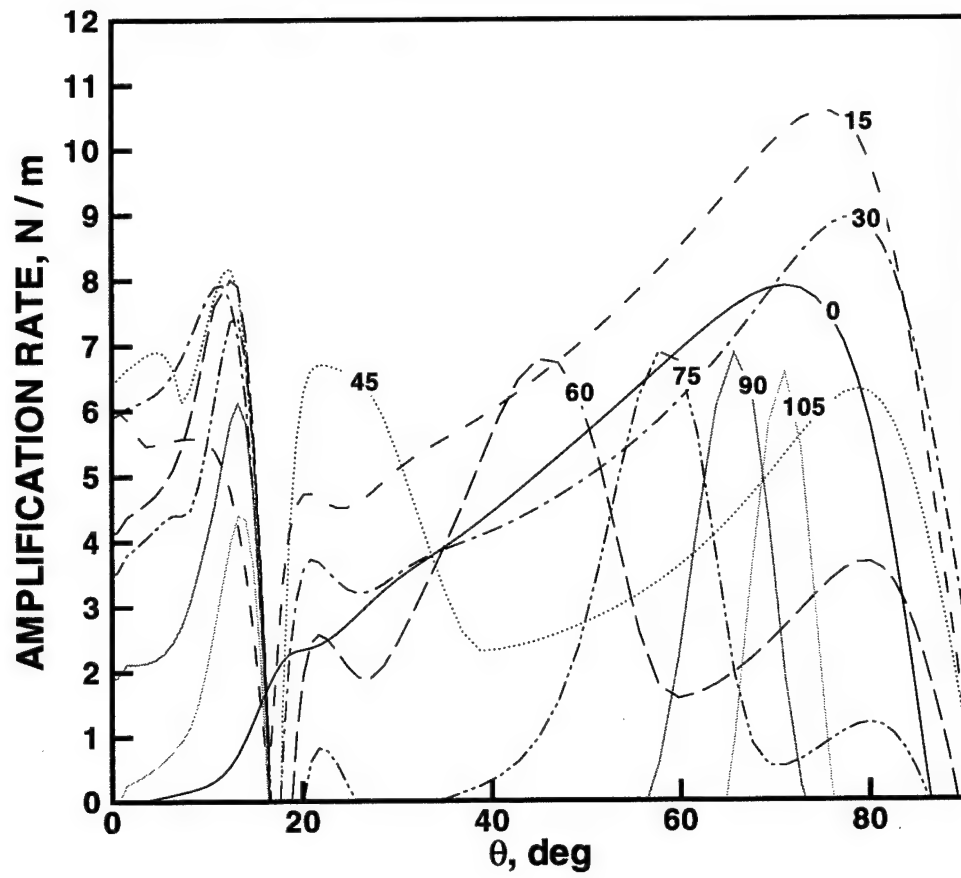Figure 7-11. Coherence function at $x/L = 0.8$, $Re = 1.6 \times 10^6$.

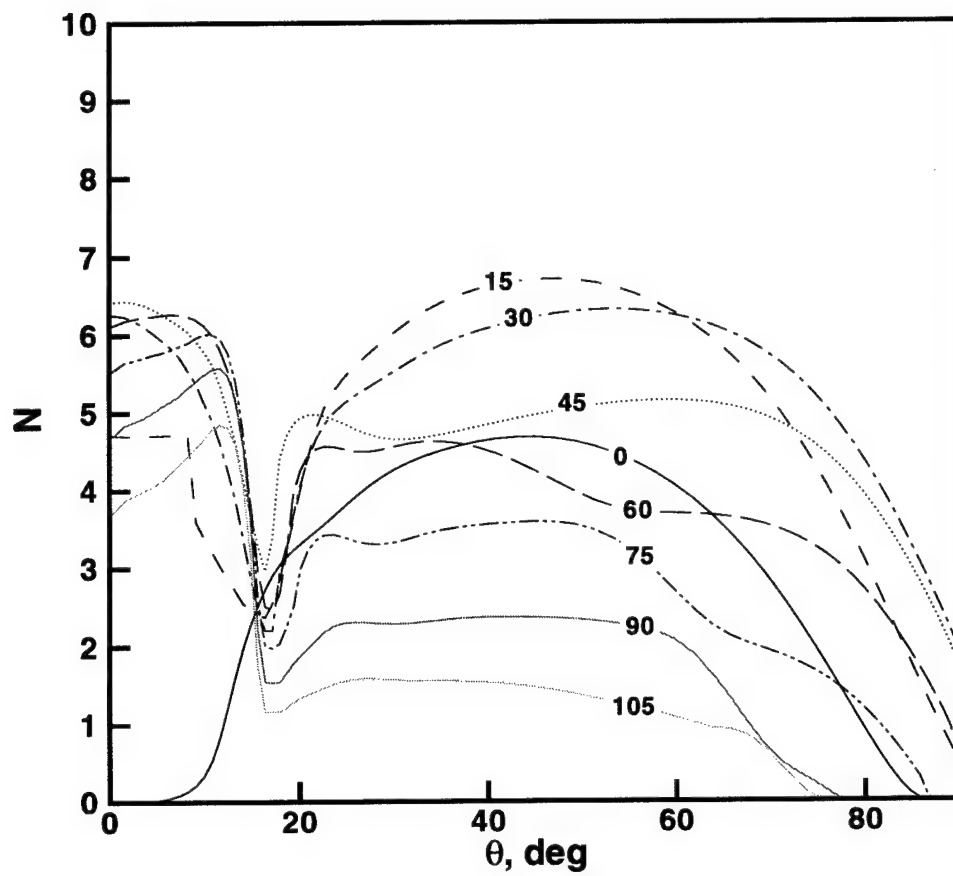Figure 7-12. Calculated amplification rates for the elliptic cone at $x/L = 0.8$, $Re = 1.6 \times 10^6$.

Figure 7-13. Calculated N-factors for the elliptic cone at $x/L = 0.8$, Re $= 1.6 \times 10^6$.

8. REFERENCES

[1] Mack, L. M., "Boundary-Layer Stability Theory," *Special Course on Stability and Transition of Laminar Flow*, edited by R. Michel, AGARD Report No. 709, pp. 3-1 to 3-81, 1984.

[2] Reshotko, E., "Stability Theory as a Guide to the Evaluation of Transition Data, " *AIAA J.*, vol. 7, no. 6, pp. 1086-1091, June 1969.

[3] Stetson, K. F., and Kimmel, R. L., "On Hypersonic Boundary-Layer Stability, " AIAA-92-0737, January 1992.

[4] Lachowicz, J. T., Chokani, N., and Wilkinson, S. P., "Boundary Layer Stability Measurements in a Hypersonic Quiet Tunnel," *AIAA Journal*, Vol. 34, No. 12, 1996, pp. 2496-2500.

[5] Doggett, G. P., Chokani, N., and Wilkinson, S. P., "Hypersonic Boundary-Layer Stability Experiments on a Flared-Cone Model at Angle of Attack in a Quiet Wind Tunnel," AIAA Paper 97-0557, Jan. 1997.

[6] Breuer, K. S., Dzenitis, E. G., Gunnarsson, J., and Ullmar, M., "Linear and nonlinear evolution of boundary layer instabilities generated by acoustic-receptivity mechanisms," *Physics of Fluids*, vol. 8, no. 6, June 1996, pp. 1415-1423.

[7] Mack, L. M., "Boundary-Layer Stability Analysis for Sharp Cones at Zero Angle-of-Attack," Air Force Wright Aeronautical Laboratory Technical Report AFWAL-TR-86-3022, Aug. 1986.

[8] Herbert, Th., Stuckert, G. K., and Lin, N., "Method for Transition Prediction in High-Speed Boundary Layers," Air Force Wright Laboratory Technical Report WL-TR-93-3097, Sep. 1993.

[9] Chang, C.-L., and Malik, M. R., "Non-Parallel Stability of Compressible Boundary Layers," AIAA Paper 93-2912, July 1993.

[10] Pruett, C. D., and Chang, C.-L., "Spatial Direct Numerical Simulation of High-Speed Boundary-Layer Flows, Part II: Transition on a Cone in Mach 8 Flow," *Theoretical and Computational Fluid Dynamics*, vol. 7, 1995, pp. 49-76.

[11] Gaster, M., "A theoretical model of a wave packet in the boundary layer on a flat plate," *Proceedings of the Royal Society of London*, vol. A. 347, pp. 271-289.

[12] Balakumar, P., and Malik, M., "Waves produced from a harmonic point source in a supersonic boundary-layer flow," Journal of Fluid Mechanics, vol. 245, 1992, pp. 229-247.

[13] Kendall, J. M., "Wind Tunnel Experiments Relating to Supersonic and Hypersonic Boundary-Layer Transition," *AIAA J.*, vol. 13, no. 3, pp. 290-299, March 1975.

[14] Demetriades, A., "Hydrodynamic Stability and Transition to Turbulence in a Hypersonic Boundary Layer Over a Sharp Cone, " AFOSR TR-75-1435, July 1975.

[15] Kimmel, R. L., and Kendall, J. M., "Nonlinear Disturbances In a Hypersonic Laminar Boundary Layer," AIAA Paper 91-0320, Jan. 1991.

[16] Owen, F. K., and Horstman, C. C., "On the structure of hypersonic turbulent boundary layers, " *J. Fluid Mech*, vol. 53, part 4, pp. 611-636, 1972.

[17] Demetriades, A., and Laderman, A. J., "Space-Time Correlation Structure of Hypersonic Boundary Layers, " *AIAA J.*, vol. 14, no. 2, pp. 256-257, February 1976.

[18] Spina, E. F., Donovan, J. F., and Smits, A. J., "On the structure of high-Reynolds-number supersonic turbulent boundary layers," *Journal of Fluid Mechanics*, vol. 222, 1991, pp. 293-327.

[19] Owen, F. K., and Horstman, C. C., "Hypersonic Transitional Boundary Layers," *AIAA J.*, vol. 10, no. 6, June 1972, pp. 769-775.

[20] Reed, H. L., and Saric, W. S., "Stability of Three-Dimensional Boundary Layers," *Annual Review of Fluid Mechanics*, 1989, pp. 235-284.

[21] Reed, H. L., and Saric, W. S., "Stability of Three-Dimensional Boundary Layers," *Annual Review of Fluid Mechanics*, 1989, pp. 235-284.

[22] Cattafesta III, L. N., Iyer, V., Masad, J. A., King, R. A., and Dagenhart, J. R., "Three-Dimensional Boundary-Layer Transition on a Swept Wing at Mach 3.5," *AIAA Journal*, vol. 33, no. 11, November 1995, pp 2032-2037.

[23] Malik, M., and Balakumar, P., "Instability and Transition in Three-Dimensional Supersonic Boundary Layers," AIAA-92-5049, December 1992.

[24] Balakumar, P., and Reed, H. L., "Stability of three-dimensional supersonic boundary layers," *Phys. Fluids A*, vol. 3 no. 4., Apr. 1991, pp 617-632.

[25] Herbert, Th., Stuckert, G. K., and Lin, N., "Method for Transition Prediction in High-Speed Boundary Layers," Air Force Wright Laboratory Technical Report WL-TR-93-3097.

[26] Burke, G. L., "Heat Transfer and Pressure Distributions About Sharp and Blunt Elliptic Cones at Angles of Attack and High Mach Numbers," Air Force Flight Dynamics Laboratory Technical Report AFFDL-TR-64-172, May 1965.

[27] McCauley, W. D., Saydah, A. R., and Bueche, J. F., "Effect of Spherical Roughness on Hypersonic Boundary-Layer Transition," *AIAA Journal*, vol. 4, no. 12, December 1966, pp. 2142-2148.

[28] DiCristina, V., "Three-Dimensional Boundary Layer Transition on a Sharp 8° Cone at Mach 10," *AIAA Journal*, vol. 8, no. 5, May 1970, pp. 852-856.

[29] Stetson, K. F., "Mach 6 Experiments of Transition on a Cone at Angle of Attack," *Journal of Spacecraft and Rockets*, vol. 19, no. 5, Sep.-Oct. 1982, pp. 397-403.

[30] Stetson, K. F., Thompson, E. R., Donaldson, J. C., and Siler, L. G., "Laminar Boundary Layer Stability Experiments on a Cone at Mach 8, Part 3: Sharp Cone at Angle of Attack," AIAA-85-0492, January 1985.

[31] King, R. A., "Mach 3.5 Boundary-Layer Transition on a Cone at Angle of Attack," AIAA-91-1804, Jun. 1991.

[32] Holden, M., Bower, D., and Chadwick, K., "Measurements of Boundary Layer Transition on Cones at Angle of Attack for Mach Numbers from 11 to 13," AIAA-95-2294, June 1995.

[33] Arnal, D., Vignau, F., Laburthe, F., "Recent Supersonic Transition Studies With Emphasis on the Swept Cylinder Case," *Boundary Layer Transition and Control Proceedings*, Peterhouse College, Cambridge, UK, 8-12 April 1991, pp. 3.1-3.14.

[34] Murakami, A., Stanewsky, E., and Krogman, P., "Boundary Layer Transition on Swept Cylinders at Hypersonic Speeds," *AIAA Journal*, vol. 34, no. 4, April 1996, pp. 649-654.

[35] Oberkampf, W. L., Aeschliman, D. P., Tate, R. E., and Henfling, J. F., "Experimental Aerodynamics Research on a Hypersonic Vehicle," Sandia Report SAND92-1411, April 1993.

[36] Pate, S. R., "Dominance of Radiated Aerodynamic Noise on Boundary-Layer Transition in Supersonic-Hypersonic Wind Tunnels, Theory and Application," Arnold Engineering Development Center Technical Report AEDC-TR-77-107, March 1978, p. 49.

[37] Reed, H. L., and Haynes, T. S., "Transition Correlations in Three-Dimensional Boundary Layers," *AIAA Journal*, vol. 32, no. 5, May 1994, pp. 923-929.

[38] Lyttle, I. J., and Reed, H. L., "Use of Transition Correlations for Three-Dimensional Boundary Layers Within Hypersonic Flows," AIAA-95-2293, June 1995.

[39] Boudreau, A. H., "Performance and Operational Characteristics of AEDC/VKF Tunnels A, B, and C," AEDC-TR-80-48 (AD A102614), July 1981.

[40] Donaldson, J. and Coulter, S., "A Review of Free-Stream Flow Fluctuation and Steady-State Flow Quality Measurements in the AEDC/VKF Supersonic Tunnel A and Hypersonic Tunnel B," AIAA paper 95-6137, Apr. 1995.

[41] Stetson, K. F., Thompson, E. R., Donaldson, J. C., and Siler, L. G., "Laminar Boundary Layer Stability Experiments on a Cone at Mach 8, Part 1: Sharp Cone," AIAA Paper 83-1761, Jul. 1983.

[42] Demetriades, A., and Anders, S. G., "Characteristics of Hot Film Anemometers for Use in Hypersonic Flows," *AIAA J.*, vol. 28, no. 11, pp. 2003-2005, November 1990.

[43] Demetriades, A., "Frequency Response of Constant-Current Film Anemometers," *J. Heat Mass Transfer*, vol. 36, no. 1, pp. 231-232, 1993.

[44] Donaldson, J. C., Nelson, C. G., and O'Hare, J. E., "The Development of Hot-Wire Anemometer Test Capabilities for M=6 and M=8 Applications," AEDC-TR-76-88 (AD A029570), September 1976.

[45] Bendat, J.S., and Piersol, A. G., *Random Data Analysis and Measurement Procedures,* 2nd ed., John Wiley and Sons, New York, 1986, pp. 294-302.

[46] Malik, M. R., "Prediction and Control of Transition in Hypersonic Boundary Layers," AIAA Paper 87-1414, Jun. 1987.

[47] Donaldson, J. C., and Hatcher, M. G., ``Investigation of the Development of Laminar Boundary-Layer Instabilities Along a Cooled-Wall Cone in Hypersonic Flows," AEDC-TSR-88-V32, Sep. 1988.

[48] Kimmel, 1993, "Experimental Transition Zone Lengths in Pressure Gradient in Hypersonic Flow," ASME FED Vol. 151, Symposium on Transitional and Turbulent Compressible Flows, Jun. 1993, pp. 117-127.

[49] Kendall, J. M., "Boundary Layer Receptivity to Freestream Turbulence," AIAA Paper 90-1504, Jun. 1990.

[50] Gaster, M., and Grant, I., "An experimental investigation of the formation and development of a wave packet in a laminar boundary layer," *Proceedings of the Royal Society of London*, vol. A. 347, pp. 253-269.

[51] Nikias, C. L. and Raghuveer, M. R., "Bispectrum Estimation: A Digital Signal Processing Framework," *Proceedings of the IEEE*, Vol. 75, no. 7, Jul. 1987, pp. 869-891.

[52] Hajj, M., Miksad, R., and Powers, E., "Experimental Investigation of the Fundamental-Subharmonic Coupling: Effect of the Initial Phase Difference," AIAA paper 91-0624, Jan. 1991.

[53] Schubauer, G. B. and Skramstad, H. K., "Laminar boundary layer oscillations and stability of laminar flow," *Journal of the Aeronautical Sciences*, v. 14, pp. 69-78, 1947. Originally published as confidential wartime report, April, 1943.

[54] Potter, J. L. and Whitfield, J. D., "Boundary layer transition under hypersonic conditions," AGARDograph 97, NATO Advisory Group for Aerospace Research and Development, 7 Rue Ancelle 92200 Neuilly Sur Seine France, 1965.

[55] Cohen, J., Breuer, K. S., and Haritonidis, J. H., "On the evolution of a wave packet in a laminar boundary layer," *Journal of Fluid Mechanics*, v. 225, pp. 575-606, 1991.

[56] Cohen, J., "The initial evolution of a wave packet in a laminar boundary layer," *Physics of Fluids*, v. 6, n. 3, pp. 1133-1143, March 1994.

[57] Criminale, W. O. and Kovasznay, L. S. G., "The growth of localized disturbances in a laminar boundary layer," *Journal of Fluid Mechanics*, v. 14, pp. 59-80, 1962.

[58] Landau, L. D. and Lifshitz, E. M., *Fluid Mechanics*, Pergamon Press, London, 1st edition, 1959.

[59] Whitham, G. B., "A note on group velocity," *Journal of Fluid Mechanics*, v. 9, pp. 347-352, 1960.

[60] Segel, L. A., *Mathematics Applied to Continuum Mechanics*, Dover, New York, 1987.

[61] Van Dyke, M., *An Album of Fluid Motion*, chapter 5, The Parabolic Press, Stanford, CA, 1982.

[62] Benjamin, T. B., "The development of three-dimensional disturbances in an unstable film of liquid flowing down and inclined plane," *Journal of Fluid Mechanics*, v. 10, pp. 401-419, 1961.

[63] Mack, L. M., "Linear Stability Theory and the Problem of Supersonic Boundary Layer Transition," AIAA Journal, v. 13, no. 3, pp. 278-289, March 1975.

[64] Lawrence, S. L., Tannehill, J. C., and Chaussee, D. S., "An Upwind Algorithm for the Parabolized Navier-Stokes Equations," AIAA paper 86-1117, May 1986.

[65] Malik, M. R., "e^{Malik}: A New Spatial Stability Analysis Program for Transition Prediction Using the e^N Method," High Technology Report No. HTC-8902, March 1989.

[66] Perry, A. E., and Chong, M. S., "Topology of Flow Patterns in Vortex Motions and Turbulence," *Eddy Structure Identification in Free Turbulent Shear Flows*, Proceedings of the 1992 IUTAM Symposium. Poitiers, France, Bonnet, J.-P. and Glauser, M., ed., 1993

[67] Schlichting, H., *Boundary-Layer Theory*, 7th Edition, McGraw-Hill Book Company, New York, p. 330.

[68] Stetson, K. F., Thompson, E. R., Donaldson, J. C., and Siler, L. G., "Laminar Boundary Layer Stability Experiments on a Cone at Mach 8, Part 2: Blunt Cone," AIAA-84-0006, January 1984.

[69] Stetson, K. F., Thompson, E. R., Donaldson, J. C., and Siler, L. G., "Laminar Boundary Layer Stability Experiments on a Cone at Mach 8, Part 5: Tests with a Cooled Model, AIAA 89-1895, June 1989.

[70] Stetson, K. F., "On Predicting Hypersonic Boundary Layer Transition," Air Force Wright Aeronautical Laboratories Technical Memorandum AFWAL-TM-87-160-FIMG, March 1987, pp. 35-36.

[71] Bertin, J. J., Stetson, K. F., Bouslog, S. A., Caram, J. M., "Effect of Isolated Roughness Elements on Boundary-Layer Transition for Shuttle Orbiter," AIAA paper 96-1906, Jun. 1996.

[72] Poggie, J., and Kimmel, R. L., "Traveling Instabilites in Elliptic Cone Boundary Layer Transition at Mach 8," AIAA paper 98-0435, Jan., 1998.